Universitá degli studi di Napoli *Federico II*

ICFO – Institut de Ciencies Fotoniques

DOTTORATO DI RICERCA IN
FISICA

Ciclo XXX
Coordinatore: Prof. Salvatore Capozziello

Simulation and bulk detection of topological phases of matter

Settore scientifico/disciplinare: Fis03

Dottoranda:
Maria Maffei

Tutori:
Prof. Lorenzo Marrucci
Prof. Maciej Lewenstein

Anni 2014/2018

Abstract

Differently from the majority of the other phases of matter, which are characterized by local order parameters, the topological phases are characterized by integer or semi-integer numbers, the topological invariants, which are depending on global properties and robust against impurities or deformations. In the last decade, the study of the topological phases of matter has been developing parallel to the field of quantum simulation. Quantum simulators are fully controllable experimental platforms simulating the dynamics of systems of interest by the use of the mapping between the two Hamiltonians. These simulators represent a key resource in the study of topological phases of matter because their observation in natural systems is usually highly problematic and sometimes impossible. Quantum simulators are commonly realized with cold atoms in optical lattices or with photonic systems. The unitary and time-periodic protocols, known as quantum walks, are a versatile class of photonic quantum simulators. The purpose of this PhD thesis is to design feasible protocols to simulate and characterize topological non-interacting crystalline Hamiltonians in 1 and 2 dimensions. Moreover, this thesis contains the description of the experiments that have been completed using the theoretical proposals. In details: i) We demonstrate that the topological invariant associated to chiral symmetric 1D Hamiltonians becomes apparent through the long time limit of a bulk observable, the mean chiral displacement (MCD). This detection method converges rapidly and requires no additional elements (i.e. external fields) or filled bands. The MCD has been used to characterize the topology of a chiral-symmetric 1D photonic quantum walk and to detect a signature of the so-called topological Anderson insulating phase in a disordered chiral symmetric wire simulated with ultracold atoms. ii) We designed the protocol to measure the topological invariant that characterizes a 2D photonic quantum walk simulating a Chern insulator.

Abstract

A diferencia de la mayoría de las otras fases de la materia, caracterizadas por un parámetro de orden local, las fases topológicas de la materia se definen por su invariante topológico que depende de las propiedades globales del sistema y es robusto frente a la presencia de impurezas y/o deformaciones. En la última década, el estudio de las fases topológicas de la materia se ha desarrollado en paralelo con el campo de la simulación cuántica. Un simulador cuántico es unas plataformas experimental altamente controlable cuyo objetivo es simular la dinámica de un sistema de interés, mediante la correspondencia entre los dos Hamiltonianos. Estos simuladores representan un recurso clave en el estudio de las fases topológicas dado que su observación en sistemas reales es en general muy problemática y en determinadas ocasiones hasta imposible. Normalmente, los simuladores cuánticos se crean mediante átomos fríos en redes ópticas o con sistemas fotónicos. Los paseos cuánticos (quantum walks), un proceso unitario y temporalmente periódico, representan una de las clases mas versátiles de simuladores cuánticos. El propósito de esta tesis de doctorado es el diseño de protocolos para la simulación y la caracterización de Hamiltonianos topológicos no interactivos de estructuras cristalinas, tanto en una como en dos dimensiones. Además, en esta tesis se expone la descripción de experimentos llevados a cabo a partir del modelo teórico propuesto. En detalle: i)Demostramos que el invariante topologico asociado a la simetría quiral en una dimensión se hace aparente a partir del limite a tiempos largos de un observable del volumen (bulk), el desplazamiento quiral medio (MCD, por sus siglas en inglés). Este método de detección converge de manera rápida y no necesita de elementos adicionales (es decir, de campos externos) o bandas pobladas. El MCD ha sido utilizado para caracterizar la topología de un paseo cuántico en una dimensión con simetria quiral y para detectar la fase topologica aislante de Anderson en hilos quirales con desorden, simulados con átomos ultra fríos. ii) Hemos diseñado una protocolo para medir el invariante topológico que caracteriza un paseo cuántico en dos dimensiones simulando un aislante de Chern.

Contents

I

Introduction

Topology is an important topic in mathematics and has direct applications in physics. In simple words, topology is the branch of mathematics which classifies the objects on the basis of properties remaining unchanged under continuous deformations [1]. As an example, a coffee cup and a doughnut are equivalent from a topological point of view: it is possible to deform one into the other without breaking them, as shown in Fig. I.1; while an orange belongs to a different topological class because there is no continuous deformation which can open up an hole into it. In other words, these objects can be classified topologically according to the number of their holes which cannot be closed through continuous deformations: this number is a topological invariant and is called the *genus*. The genus of a smooth and closed surface, according to the Gauss-Bonnet theorem [1], is given by the surface integral of a function called *Gaussian curvature* containing all the second derivatives of the surface's equation. The genus can take only positive, integer values: coffee cups and doughnuts have genus one, an orange has genus zero, a two-handle cup has genus two.

Figure I.1: Continuous deformation of a coffee cup into a doughnut.

Topological phases of matter

In solid state physics, topology defines phases whose properties are absolutely unique. Indeed, on the one hand, most of the phase transitions studied in condensed matter physics share two features: they happen through symmetry breaking, and they are characterized by local order parameters which take different values in the different phases [2]. This is true, for example, in the solid/liquid/gas transitions, in the ferroelectric transition, or in the superfluid and the superconducting transitions... On the other hand, topological phase transitions happen without symmetry breaking and are characterized by topological invariants which are global properties of the systems. Topological invariants only depend on systems' dimensionality and symmetries [3]. An example of a topological phase transition is the dissociation of vortex and anti-vortex pairs in the xy model and in neutral 2D superfluids. This phase transition, studied by Berezinskii, Kosterlitz and Thouless (BKT) in the 70s [4], has been the first one to be described in terms of this "topological order" [5]. Another paradigmatic example of a topological phase of matter is the integer quantum Hall effect (IQHE) [6]. It has been observed for the first time in 1980 [7]; it consists in the quantization of the transverse electric (Hall) conductance of a 2D semiconductor at very low temperature under a strong magnetic field; changing the magnetic field, the Hall conductance forms plateaus at integer multiples of e^2/h. A couple of years

after its first observation, Thouless, Kohmoto, Nightingale and den Nijs (TKNN) explained the IQHE with a lattice model [8]. They showed that, in the low-temperature limit $T \to 0$ and for a Fermi energy lying inside a gap of the energy spectrum of the bulk, the Hall conductivity is proportional to a topological invariant, the total Chern number of the occupied bands. The Chern number takes only integer values. Being a topological invariant, its value remains unchanged under every perturbation, such as interaction or disorder, which deforms the energy spectrum without closing its gaps. In other words, it can only change through a gap-closing in the energy spectrum. This explains the plateaus in the plot of the Hall conductivity versus the magnetic flux which benchmarks the IQHE and, in general, the robustness of the Hall conductivity against perturbations. The lattice model used in the TKNN paper is known as Hofstadter model [9]. It describes non-interacting spinless electrons hopping on a square lattice pierced by a uniform magnetic field. If the magnetic flux per unit cell is set to a rational value p/q, the system, within periodic boundary conditions, is translationally invariant and it is possible to define a Bloch Hamiltonian for each value of the quasi-momentum k on the Brillouin torus. The energy spectrum is made of q separate bands, see Fig. I.2(a). For each band, the Chern number can be extracted from the Bloch Hamiltonian through an algebraic calculus analogous to the one which provides the genus of a closed surface, namely the integral over the Brillouin zone of the so-called *Berry curvature* of the energy band [10]. For a system with boundaries, current-carrying states arise on the edges [11, 12, 13]. These states are exponentially localized, have energies inside the gaps of the bulk spectrum and appear in chiral pairs with the same energy propagating in opposite directions on the two edges. These states are topological in the sense that, on each edge, their number is equal to the total Chern number of the occupied bands, see Fig. I.2(b). This makes them robust against perturbations, namely they overtake possible obstacles, such as impurities, without being reflected or backscattered [13]. This relation between edge-states and topological invariant is known as *bulk-edge* correspondence and holds in all the gapped topological systems in any spatial dimensions [14]. Some years

later in 1988, Haldane pointed out that the condition necessary for the IQHE was not the presence of the magnetic flux, but the broken time-reversal symmetry [6]. He showed it using a model of non-interacting spinless electrons hopping on a honeycomb lattice pierced by a magnetic field having zero net flux per unit cell [15], see Fig. I.3(a). The topological phase arising in such a system with zero net magnetic flux is known as anomalous quantum Hall effect and belongs to the same class of the IQHE, i.e. the class of Chern insulators.

Almost 20 years later, in 2005, Kane and Mele discovered a time-reversal-invariant analog of the quantum Hall effect, known as quantum spin Hall effect (QSHE) [16, 17]. They considered a system of non-interacting spinful electrons hopping on a layer of graphene at very low temperature. The Hamiltonians of the two different spin kinds, regarded separately, are equivalent to two conjugate Haldane Hamiltonians in which the spin-orbit coupling terms play the same role as opposite magnetic fields with zero net flux through the unit cell. Hence, the time-reversal symmetry is broken in the single spin Hamiltonians, which possess non-zero (opposite) Chern numbers, but it is intact in the overall system. This results in topologically protected edge currents of electrons with opposite spins which propagate in opposite directions on each edge. However, Kane and Mele later realized that the QSHE was too small to be observed experimentally in graphene; subsequently, its observation has been proposed [18], and realized [19], in a system of quantum nano-wells. The quantum spin Hall effect has been followed by a series of discoveries of natural and artificial crystalline systems, known as *topological insulators* [14]. They exhibit topological features wich depend only on their intrinsic properties, without any external field. Topological insulators have gapped bulk Hamiltonians and host localized edge states with energies inside the spectral gaps. These states are topologically protected against perturbations since their number on each edge is fixed by the value of the invariant (bulk-edge correspondence). The latter in general can be computed from the bulk Hamiltonian with periodic boundary conditions and depends on the system's dimensionality and symmetries. According to these features, the topological insulators can be divided in classes la-

beled by different invariants and can be ordered in a periodic table [3].

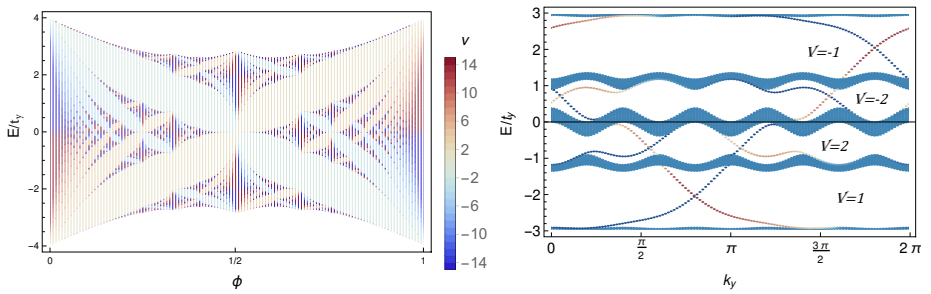

(a) (b)

Figure I.2: **IQHE in the Hofstadter model**. **a.** Hofstadter butterfly: energy spectrum (projection) of the Hofstadter model within periodic boundary conditions changing the flux per plaquette ϕ. The transverse conductivity inside each gap is proportional to the total Chern numbers of the bands below (ν). **b.** Energy spectrum of the Hofstadter Hamiltonian on the cylinder with $\phi = 1/5$. As predicted by the bulk-edge correspondence, the number of edge-states for each edge (red and blue dots) which traverse each gap during the pumping cycle is equal to the total Chern number of the bands below.

Quantum simulators

In the last decades, another branch of physics has been growing alongside the study of topological condensed matter: quantum simulation. The concept of quantum simulation was first introduced by Feynman in the beginning of the 80s: a very controllable quantum system is used to simulate the dynamics of another quantum system, taking into account the mapping between the two Hamiltonians. Simulators based on cold atoms in optical lattices [20], and photonic platforms [21] constitute a very versatile tool to simulate crystalline potentials and represent a fun-

damental resource in the study of topological phases [22, 23, 24] which in many cases are very difficult or impossible to observe in natural systems. Emblematic examples are the superfluid-Mott insulator transition, observed for the first time with bosons in an optical lattice in 2002 [25], and the 4D Integer quantum Hall effect [26], observed recently in three different simulation platforms based on trapped ultra-cold atoms [27, 28] and array of optical fibers [29].

Ultra-cold atoms simulators essentially consist of gases of neutral atoms at very low temperature trapped in periodic potentials generated by interfering laser beams [20]. In these systems, the temperature is below the critical temperature of transition to Bose-Einstein condensate or Fermi gas (depending on the spin of atoms). In this condition, once loaded in the optical lattice, the atoms mimic the dynamics of electrons in a crystalline potential [20]. The features of the lattice potential, such as the potential depth and the lattice shape, can be adjusted at will by tuning the laser fields. Since the atoms are neutral, it is non trivial to simulate magnetic fields or spin-orbit couplings. However, these elements are fundamental in order to simulate topological band-structures, and they have been realized in many cold-atoms simulators [30, 31, 32, 33, 34, 35, 36, 37, 38, 39]. The basic idea to simulate gauge fields in general is to control the phases of the hopping terms of the Hamiltonian; indeed, they can be incorporate inside these terms as *Peierls phase factors* [10]. One method employed to do this consists in laser assisted coupling between atomic levels [40]; another is the so-called Floquet engineering [41]. It consists in modulating periodically in time the atomic potential with a period much smaller than the characteristic time scale of the problem. In the long-time limit, the periodically-driven Hamiltonian is equivalent to the evolution under a static effective Hamiltonian, called Floquet Hamiltonian, in which the phases of the hopping terms depend on the periodically-driven potential. Floquet simulators are particularly interesting from the topological point of view since they have been found to possess a topology more complex than their static coun-

terpart. Indeed, in addition to the topological edge-states counted by the topological invariants of the corresponding static systems, Floquet systems can exhibit extra edge-states. Hence, new invariants are needed to obtain a bulk-edge correspondence for this kind of topological insulators [42, 43, 44, 45, 46]. A fruitful simulation strategy is also to map a lattice dimension onto an internal degree of freedom of the particles [47]. This synthetic dimension approach allowed, for example, for the simulation of a stripe starting from atoms trapped in a 1D potential [36, 37]. The concept of synthetic dimension can be used also to simulate 1D systems. For example, in Refs. [48, 49, 50], a 1D topological insulator has been simulated with a synthetic wire of ultra-cold atoms by mapping the lattice position onto the atomic momentum of the Bose-Einstein condensate.

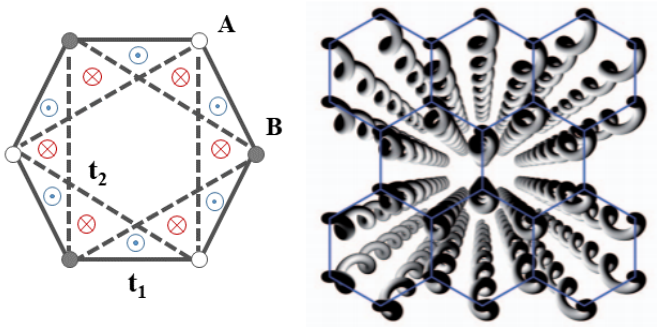

(a) (b)

Figure I.3: **Floquet honeycomb lattice of helical wave-guides**. **a.** Haldane model [15]: non-interacting spinless electrons hopping on a honeycomb lattice pierced by a magnetic field having zero net flux per unit cell. The topological non-trivial phase arises from the broken time-reversal symmetry and it is known as anomalous quantum Hall effect. **b.** Sketch of the simulator reported in Ref. [51]: a Floquet Chern insulator is realized through an honeycomb array of helical wave-guides. Figure adapted from Ref. [51].

Photonic simulators constitute another important family of simulators. They are prominently based on two kinds of architectures: photonic crystals and arrays of optical wave-guides [21]. Photonic crystals are periodic arrangements of materials with different optical properties [52]. The resulting periodicity of the dielectric and the magnetic permittivity tensors allows for the application of the Bloch theorem to the wave equation. For each value of the light wave-vector in the Brillouin zone, the modes allowed to propagate inside the crystal organize themselves in bands, as the energy eigenstates of a normal crystal [52]. The photonic bands can be made topological by choosing suitably the materials which form the crystal and, in most of the cases, by using magneto-optic crystals which work under strong magnetic field, as for example in the Chern photonic crystal proposed by Haldane and Raghu [53, 54]. While topological photonic crystal work in general in the microwave domain, topological simulators made of arrays of wave-guides can work in the optical frequency domain [24]. In these systems, the propagation direction implements the time, while the crystalline lattice is mapped onto the transverse plane. Indeed, under the *paraxial approximation* [52], the wave-equation which dictates the propagation of the electric field through the fibers takes the same form of a Schroedinger equation where the electric field plays the role of the wave function and the propagation direction that of the time. Each wave-guide represents a lattice site and the evanescent couplings between them represent the hopping terms. Thus, the latter can be tuned by adjusting the light wavelength, the refractive index of the wave-guides and the spacing between them [55]. In this setup, the Floquet engineering corresponds to give to the wave-guides a periodic modulation along the propagation direction. This has been achieved, for example, in Ref. [51], where the authors implemented a Floquet Chern insulator through an honeycomb array of helical wave-guides, see Fig. I.3(b).

Quantum walks represent a very versatile class of simulators, implementable with both cold atoms and photons [56]. Quantum walks are

periodically driven (Floquet) unitary protocols acting on two quantum observables: the walker, and its internal degree of freedom, the coin. In the simplest 1D QW, the coin has a spectrum of dimension two and the walker has an infinite and discrete spectrum of eigenvalues which can be regarded as lattice sites. The QW dynamics is given by the periodic repetition of unitary operators acting on coin and walker. It simulates stroboscopically the evolution of a particle moving on a lattice under a Floquet Hamiltonian. QWs allow for the simulation of a wide class of single-particle solid state phenomena, such as the free evolution of correlated particles [57, 58], the effect of decoherence [59, 60], Anderson localization [61], band dynamics of single electrons under constant electric fields [62], Berry phase measurement [63, 64, 65, 66]. Furthermore, in 2010, QWs have been discovered to be a valuable resource in the field of the topological condensed matter physics as they can simulate all the single-particle topological insulators in 1 and 2D [67]. In the last years, many topological 1D QW protocols have been implemented in different architectures based on both cold atoms and photons [68, 69, 70, 66, 71, 72, 73, 74]. In particular, QWs have been largely used in the study of the Floquet topological phases which, as we already mentioned, are different from their solid-state counterparts. Indeed, one can not apply to these systems the standard classification of topological insulators [3], and a new classification dedicated to Floquet topological isulators [42, 43, 44, 45, 46], and in particular to topological quantum walks [75, 67, 76], has been created. In this thesis we focused especially on photonic QWs. In these platforms, the walker is typically mapped onto a degree of freedom of a laser field, such as the optical path of the beam [59, 57, 58, 76, 77], the time delay between optical pulses [60, 78, 79], the light orbital angular momentum [69, 70, 71] (see Fig. I.4(b)) or its wave-vector [80], and the coin in general corresponds to the light's polarization.

Contents of this thesis

The aim of this thesis work is to propose detection methods and quantum walk protocols which led to the simulation of topological insulators

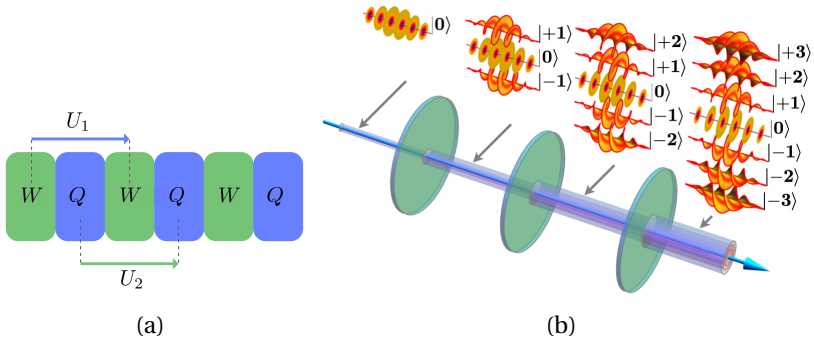

(a) (b)

Figure I.4: **Chiral-symmetric QW with twisted photons a.** Protocol of the chiral-symmetric QW. The topological classification of Floquet systems is different from that of static topological insulators; for instance, chiral-symmetric QWs are characterized by a couple of invariants which can be extracted from two Floquet operators corresponding to two different choices of the starting instant of the driving period (U_1 and U_2) [75]. **b.** Sketch of the photonic implementation of the chiral-symmetric QW with twisted photons. The walker's positions are mapped onto the values of the light's OAM. The latter counts for the number of times the beam's wave front winds around the propagation axis. The picture is adapted from Ref. [69].

in one and two dimensions. Many previous simulation experiments focused on detecting topological features at the edges of the systems [76, 81, 49, 82, 36, 37, 53, 51, 39]. In this thesis instead we develop methods to detect the topological invariants inside the bulk of the systems. These methods have the important feature of applying also to simulators in which it is very difficult or impossible to access the system's edges, as it often happens in systems which exploit an internal degree of freedom of particles as a synthetic dimension, for instance Refs. [69, 70, 71] (see Fig. I.4).

The thesis is organized as follows:

- In chapter II, we review the main features of static non-interacting topological insulators in one and two dimensions.

- In chapter III, we focus on the detection of the topology in 1D insulators protected by *chiral symmetry*.

  In Sec. III.1, which is mainly based on Ref. [83], we present our method to detect the topological invariant labeling the chiral class in 1D, the *winding number* [84]. It consists in measuring an observable called *mean chiral displacement* (MCD) which can be simply extracted from the particle's bulk dynamics with no need of additional elements, such as interferometric architectures [63, 64, 65, 66], introduction of losses [85, 86, 87], and scattering measurements [68]: the long time limit of the MCD is equal to the winding number. In this section we derive analytically this result in the case of an infinite clean system.

  In Sec. III.2, we show that the MCD can be used to detect topology also in disordered systems. Then, we present the cold atoms simulation experiment reported in Ref. [50] where the measurement of the MCD is used to detect topological phase transitions driven by a strong chiral-preserving disorder. The platform [48, 49, 50] simulates a chiral-symmetric wire; the lattice sites are mapped onto the values of the atomic momentum of the Bose-Einstein condensate. In the experiment, the MCD measurement allows for the detection of a signature of the so-called topological Anderson insulating (TAI) phase. This phase arises from the interplay between topological order and Anderson localization under a strong chiral-preserving disorder; it has been first predicted to occur in metallic 2D HgTe/CdTe quantum wells [88], but, so far, it was never been observed experimentally. In the TAI phase, the disorder closes the energy gap which is replaced by a mobility gap, and the band insulator of the clean system is replaced by an Anderson insulator that remains topological, with topology carried by localized states in the spectrum. Thereby experimental probes relying on the adiabatic

transport are expected to fail and the measurement of the MCD emerges as a very suitable method to detect the system's topology.

- In chapter IV, we review the main features of Floquet topological systems in one and two dimensions, focusing in particular on topological quantum walks and their topological classification.

- In chapter V, we describe two photonic experiments in which we realized and characterized two topological QWs, respectively in 1- and 2D.

  In Sec. V.1, we present the simulation experiment reported in Ref. [71] where we develop and apply for the first time the MCD detection method to a 1D photonic QW realizing a chiral-symmetric Floquet topological insulator, see Fig. I.4. In the QW platform [69, 70, 71], the lattice sites are mapped onto the values of the light's orbital angular momentum (OAM) [89, 90] and the coin states onto the circular polarizations. The OAM is shifted by a liquid crystal device called q-plate [91] which twists the light beams according to their polarization. Being a Floquet topological insulator, our QW is not characterized by a single winding number, as the static chiral-symmetric insulators, but by a couple of winding numbers which can be extracted from two inequivalent versions of the protocol corresponding to two different choices of the starting time of the periodic evolution [75]; we accomplish a complete topological characterization of our QW by measuring the MCD of the walker in these two different time-frames.

  In Sec. V.2, we present a novel photonic 2D QW realizing a Floquet Chern insulator [80]. In this experiment, the lattice position is mapped onto the transverse wave-vector of the light beam. This degree of freedom is manipulated through a liquid crystal device called g-plate; this device is obtained from a technology similar to that of q-plates and is essentially a polarization dependent diffraction grating. This setup represents a complete novelty in the still almost unexplored field of 2D quantum walks: these systems have

been implemented in few experiments [78, 79, 92, 93, 94] and, to our knowledge, the transverse light wave-vector has never been used as lattice position in any platform. We simulate a constant electric field acting on the system along one direction. Quantum walks with an extra costant driving, often referred to as electric quantum walks [95, 62, 96], have attracted attention for the study of phenomena such as quantum state refocusing and probability distributions revivals [95, 97, 98, 96], Bloch oscillations and Landau Zener transitions [62] and for the measurement of topological invariants [63, 64, 65, 66]. We observe the motion under the constant force of various wave-packets prepared in the lower energy band of the QW Floquet Hamiltonian and we extract the band's Chern number from their overall transverse displacement [99].

List of publications

The original results that are presented in this thesis have been published in the following papers, the list contains also a brief description of my contribution to each of them:

- Ref. [70] *Statistical moments of quantum-walk dynamics reveal topological quantum transitions*,
  F. Cardano, M. Maffei, F. Massa, B. Piccirillo, C. de Lisio, G. De Filippis, V. Cataudella, E. Santamato and L. Marrucci,
  Nature Communications **7**, 11439 (2016).
  In this work, Filippo Cardano and I contributed to develop the theoretical framework and to perform the experiment.

- Ref. [71] *Detection of Zak phases and topological invariants in a chiral quantum walk of twisted photons*,
  F. Cardano, A. DErrico, A. Dauphin, M. Maffei, B. Piccirillo, C. de Lisio, G. De Filippis, V. Cataudella, E. Santamato, L. Marrucci, M. Lewenstein and P. Massignan,
  Nature Communications **8**, 15516 (2017).
  In this work, I took part in the initial stage of the experimental work transmitting my knowledge of the setup to Alessio D'Errico who continued the experiment and contributed to the development of the detection method working in Naples in parallel with Alexandre Dauphin and Pietro Massignan. I also performed more realistic simulations of the QW dynamics to fit the experimental conditions.

- Ref. [83] *Topological characterization of chiral models through their long time dynamics*,
  M. Maffei, A. Dauphin, F. Cardano, M. Lewenstein and Pietro Massignan,
  New Journal of Physics **20** (2018).
  Here, I developed the theory deriving the proofs and performing the simulations.

- Ref. [50] *Observation of the topological Anderson insulator in disordered atomic wires*,
  E. J. Meier, F. Alex An, A. Dauphin, M. Maffei, P. Massignan, T. L. Hughes, B. Gadway,
  Science **362**, 6417 (2018).
  In this work, I made simulations to obtain the phase diagram and to compare the theory with the experimental results.

- Ref. [80] *Two-dimensional topological quantum walks in the momentum space of structured light*,
  A. D'Errico, F. Cardano, M. Maffei, A. Dauphin, R. Barboza, C. Esposito, B. Piccirillo, M. Lewenstein, P. Massignan, L. Marrucci,
  arXiv preprint arXiv:1811.04001 (2018).
  In this work, Alexandre Dauphin and I proposed the method we used to detect the Chern number and followed step by step its implementation adjusting the theoretical framework to match the experimental requirements. I also made simulations of the QW dynamics to fit the experimental conditions.

II

Non-interacting static topological insulators

In this chapter, we review the properties of two classes of non-interacting topological insulators in one and two dimensions. These Hamiltonians have a gapped bulk spectrum, but exhibit gapless modes exponentially localized on the edges, when they are in a topologically non-trivial phase. These systems are protected by a global topological order which makes their transport properties robust against gap preserving and symmetry preseving perturbations. Indeed, a set of discrete nonspatial symmetries, together with the systems' dimensionality, determines the topological classification of these Hamiltonians. Each class is labelled by a topological invariant which can be derived from the bulk Hamiltonian, it counts the number of topological states with energy inside the gap which arise on each edge of the system; this unique property of topological insulators is called *bulk-edge correspondence*.

In Sec. II.1, we review the properties of the 1D topological insulators protected by chiral symmetry: we give the definition of the associated topological invariant, the *winding number* (SubSec. II.1.2) and we compute it for a concrete model, the celebrated SSH model (SubSec. II.1.3). Finally, we give the definitions of Berry-Zak phase (SubSec. II.1.4) and of

bulk polarization for a band insulator (SubSec. II.1.5).

In Sec. II.2, we review the Integer Quantum Hall effect (IQHE) on the lattice: we give the definition of *Chern number* and outline its relation with the quantized Hall conductivity (SubSec. II.2.2) and with the normalized density of particle (SubSec. II.2.3). Finally, we consider a system with cylindrical boundary conditions (periodic along one direction and open along the other) and topological edge states (SubSec. II.2.4).

II.1 1D chiral-symmetric systems

II.1.1 Chiral symmetry and nonspatial discrete symmetries

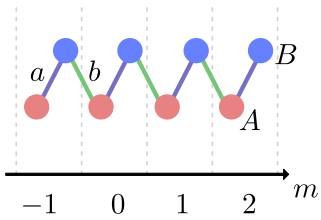

Figure II.1: **SSH model**. The SSH model [100] is the simplest 1D chiral model. It describes non-interacting electrons hopping along the polyacetylene chain. Each cell of the chain is composed of two sites A and B. The dynamics of the electrons is described to a very good approximation by a tight-binding model with staggered tunneling a and b, see Eq. (II.12).

In this section, we review the properties of 1D topological Hamiltonians with *chiral symmetry* (CS) [84]. An Hamiltonian is chiral-symmetric, if there exists an hermitian and unitary operator Γ, such that $\Gamma^2 = 1$, which anticommutes with it:

$$\Gamma H \Gamma^{-1} \equiv \Gamma H \Gamma = -H. \tag{II.1}$$

Equation (II.1) has a remarkable consequence: in a chiral system one may always identify two intertwined sublattices A and B, of equal length. Each unit cell of the lattice contains $\mathcal{D}$ sites, with $\mathcal{D}$ even: $\mathcal{D}/2$ sites belong to A and $\mathcal{D}/2$ to B; the Hamiltonian swaps them. We call *canonical basis* the eigenbasis of the chiral operator, where it takes the form:

$$\Gamma = \begin{pmatrix} \mathbb{I} & 0 \\ 0 & -\mathbb{I} \end{pmatrix}. \tag{II.2}$$

If we denote the eigenstates of the Bloch Hamiltonian in the canonical basis by $|\psi_j(k)\rangle$, with $j = \pm 1, \ldots, \pm\mathcal{D}/2$, and the corresponding energies by $E_j(k)$ (with $E_j(k) > 0$ for $j > 0$), then $\Gamma|\psi_j\rangle = |\psi_{-j}\rangle$, with $E_{-j} = -E_j$; namely, the eigenstates of chiral systems appear in chiral-partners pair. We can write Γ in terms of *partial chiral operators*:

$$\Gamma = \sum_{j=1}^{\mathcal{D}/2} \Gamma_j = \sum_{j=1}^{\mathcal{D}/2} |\psi_j\rangle\langle\psi_{-j}| + |\psi_{-j}\rangle\langle\psi_j|. \tag{II.3}$$

Together with the chiral symmetry, other two nonspatial discrete symmetries, the *time-reversal* symmetry (TRS) and *particle-hole* symmetry (PHS), allow for a topological classification of the gapped non-interacting Hamiltonians according to the celebrated periodic table of topological insulators and superconductors [14, 3]. For example, a 1D chiral-symmetric system of spinless non-interacting particles belongs to the AIII class if it has no other discrete symmetries, or to the BDI class if it has also TRS and PHS.

An Hamiltonian is time-reversal-symmetric if it commutes with a anti-unitary operator $\mathcal{T} = \tau K$, where τ is a unitary operator and K is the complex conjugation. The complex conjugation K acts in real space as $Kf(r) = f^*(r)K$ and in quasi-momentum space as $Kg(k) = g^*(-k)K$. A time-reversal-symmetric Hamiltonian verifies:

$$\mathcal{T}H\mathcal{T}^{-1} \equiv \tau H^* \tau^\dagger = H. \tag{II.4}$$

$\mathcal{T}^2$ gives either 1 or -1. In particular systems of particles with odd-half-integer spin have $\mathcal{T}^2 = -1$, while systems of particles with integer spin (or spinless) have $\mathcal{T}^2 = 1$ [3].

An Hamiltonian is particle-hole symmetric if it anticommutes with a anti-unitary operator $\mathcal{P} = PK$, where P is a unitary operator and K the complex conjugation:

$$\mathcal{P}H\mathcal{P}^{-1} \equiv PH^*P^\dagger = -H. \tag{II.5}$$

If ψ_j is an eigenstate of a particle-hole symmetric non-interacting Hamiltonian of eigenvalue E_j, its particle-hole reversed partner, $\mathcal{P}|\psi_j\rangle = |\psi_{-j}\rangle$ is still an eigevector of energy $-E_j$, [3]. $\mathcal{P}^2$ gives either 1 or -1.

A chiral operator can be found as combination of a particle-hole and a time-reversal operator, $\Gamma = \mathcal{T}\mathcal{P}$. Therefore, an Hamiltonian can possess either just one or the complete set of symmetries.

II.1.2 Winding number

The topological invariant characterizing 1D chiral systems is an integer called *winding number* $\mathcal{W}$. According to the bulk-edge correspondence, the number of edge states on each edge is equal to $|\mathcal{W}|$. The winding number $\mathcal{W}$ may be found in various equivalent ways, starting from either the Hamiltonian with periodic boundary conditions, or its eigenstates. In this subsection we give three equivalent definitions of it.

Let us consider a non-interacting tight-binding Hamiltonian on a lattice of N unit cells and $\mathcal{D}$ sites per unit cell. We will only consider the case where $\mathcal{D}$ is even, else chiral model necessarily present flat bands at zero energy. For the chiral symmetry, $\mathcal{D}/2$ sites per unit cell belongs to the sublattice A and $\mathcal{D}/2$ to the sublattice B. In the canonical basis, where the chiral operator takes the form (II.2), the Hamiltonian has a completely block-off-diagonal form

$$H = \begin{pmatrix} 0 & h^\dagger \\ h & 0 \end{pmatrix}. \tag{II.6}$$

$\mathcal{W}$ can be found in terms of the winding of the lower-left block h of the off-diagonal Hamiltonian [84], for simplicity, unless explicitly needed,

from now on we will often drop momentum indices:

$$\mathcal{W} = \oint \frac{\mathrm{d}k}{2\pi i} \mathrm{Tr}[h^{-1}\partial_k h] = \oint \frac{\mathrm{d}k}{2\pi i} \partial_k \log[\mathrm{Det}(h)] \tag{II.7}$$
$$= \oint \frac{\mathrm{d}k}{2\pi} \partial_k \arg[\mathrm{Det}(h)] = \sum_{j=1}^{\mathcal{D}/2} \oint \frac{\mathrm{d}k}{2\pi i} \partial_k \log h_j,$$

where $\{h_j\}$ denote the complex eigenvalues of the matrix h. We have implicitly assumed that the Hamiltonian is gapped at zero energy, so that both H and h are invertible, and we have used the fact that the integral of the derivative of a continuous and periodic function is zero over a complete period. The winding of the model is therefore given by the cumulative winding of all eigenvalues of h around the origin of the complex plane.

Equivalently, one may compute $\mathcal{W}$ using the flat-band Hamiltonian, the Q-matrix [3]. This is defined as the difference between the projector on the eigenstates of positive energy, minus the one on the states of negative energy,

$$Q = \sum_{j=1}^{\mathcal{D}/2} Q_j = \sum_{j=1}^{\mathcal{D}/2} P_j - P_{-j}, \tag{II.8}$$

where $P_j = |\psi_j\rangle\langle\psi_j|$, with $j = \pm 1, \ldots, \pm\mathcal{D}/2$, are the projectors on the Bloch Hamiltonian's eigenstates. The Q-matrix has the following properties: (i) it is Hermitian and unitary, (ii) it satisfies $Q^2 = \mathcal{I}$, so that its eigenvalues are simply $\lambda_Q = \pm 1$, (iii) it is diagonal in any basis of eigenvectors of H, (iv) once expressed in the canonical basis, it becomes block-off-diagonal,

$$Q = \begin{pmatrix} 0 & q^\dagger \\ q & 0 \end{pmatrix}, \tag{II.9}$$

with q unitary.

$\mathcal{W}$ can be extracted from the winding of q,

$$\mathcal{W} = \oint \frac{\mathrm{d}k}{2\pi i} \mathrm{Tr}[q^{-1}\partial_k q] = \oint \frac{\mathrm{d}k}{2\pi} \partial_k \arg[\mathrm{Det}(q)]. \tag{II.10}$$

The last equality may be simply demonstrated writing $q = \sqrt{\mathrm{Det}(q)}u$, so that $u \in SU(2)$, and exploiting the fact that the winding of any $SU(2)$ matrix is zero

Alternatively, as discussed in Ref. [101], the winding may be identified with a bulk observable called skew polarization $\mathcal{S} = \sum_{j\in \mathrm{occ.}} \mathcal{S}_j$,

$$\mathcal{W} = \oint \frac{\mathrm{d}k}{\pi} \mathcal{S}(k). \tag{II.11}$$

The quantity $\mathcal{S}_j = i\langle \Gamma\psi_j|\psi_j'\rangle$ (with $|\psi_j'\rangle \equiv \partial_k|\psi_j\rangle$) may be shown to be a purely real number, and $\mathrm{occ.}$ denotes the set of occupied bands (i.e., of negative energies). From these definitions, it is clear that the winding is not a property of a single band, but rather of the $\mathcal{D}/2$ negative (or positive) energy bands, which all contribute to its value.

Chiral symmetric chains have been simulated with cold atoms [63, 49] and photonic architectures [76, 86], and their topological properties have been witnessed through the observation of edge states [76, 49] or the direct measure of the invariant [63, 86].

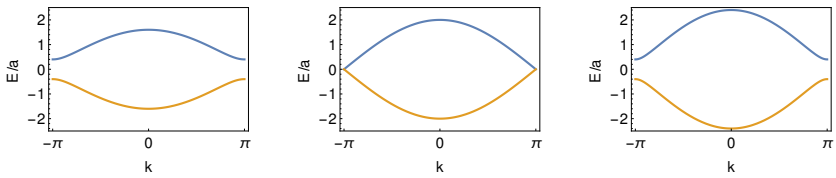

(a)

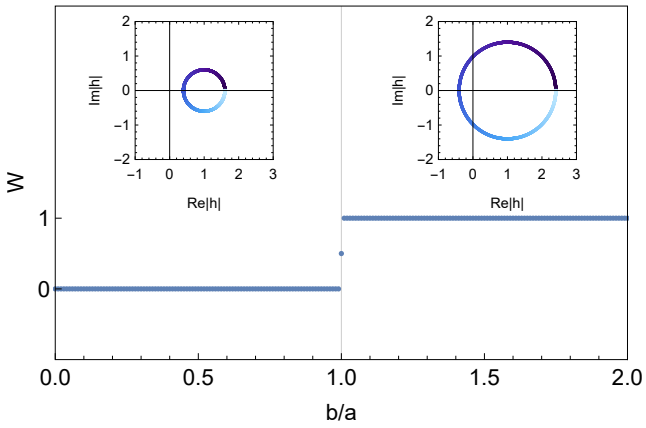

(b)

Figure II.2: **Energy dispersion and winding number of the SSH model**. **a.** Energy dispersion of the Bloch Hamiltonian for different values of the hopping ratio b/a, from left to right $b/a = 0.6$, $b/a = 1$, $b/a = 1.4$. The spectrum is gapped in both the topological phases and gapless at the transition. **b.** Winding number of the SSH model. The three definitions of the winding number (II.7), (II.10) and (II.11) coincide in predicting for the SSH model a non-trivial phase ($\mathcal{W} = 1$) when the intra-cell hopping a is smaller that the inter-cell one b. The insets display the winding of $h(k)$ varying k, namely the value of $h(k) = a + be^{ik}$ in the complex plane, as k is varied between 0 (blue) to 2π (white), for $b/a = 0.6$ (left side) and $b/a = 1.4$ (right side). In the trivial phase, when $W = 0$, the winding of $h(k)$ does not enclose the origin, in the non-trivial one ($\mathcal{W} = 1$), it encloses it.

II.1.3 The SSH model

The simplest 1D chiral model is the one introduced by Su, Schrieffer and Heeger (SSH) to provide an effective model for a single electron moving along the polyacetylene chain [100]. It is a tight-binding model with staggered tunnelings, so that the unit cell is composed of two sites (i.e., it has internal dimension $\mathcal{D} = 2$), see Fig. II.1.

$$H = \sum_n \left[a c_n^\dagger \sigma_x c_n + b \left(c_{n+1}^\dagger \frac{(\sigma_x - i\sigma_y)}{2} c_n + \text{h.c.} \right) \right], \tag{II.12}$$

where $c_n^\dagger = (c_{n,A}^\dagger, c_{n,B}^\dagger)$ creates a particle at unit cell n in sub-lattice site A or B, c_n is the corresponding annihilation operator, and σ_i are the Pauli matrices. The a and b characterize the intra- and inter-cell tunneling energies. It is straightforward to see that the SSH Hamiltonian possesses also time-reversal and particle-hole symmetries squaring to 1 and therefore it belongs to the BDI topological class [84].

We can consider an infinite chain and pass to the quasi-momentum space. For each value of k, the Bloch Chiral operator is σ_z. In the eigenbasis of σ_z, the Bloch Hamiltonian (II.6), and the Q-matrix (II.9) take an off-diagonal form. We will have $h = a + be^{ik}$, and $q = h/|h|$, so that $\arg h = \arg q$. As k traverses the Brillouin zone from 0 to 2π, both complex numbers h and q wind once in the positive (counter-clockwise) direction, so that the winding number computed using Eq. (II.7) and (II.10) is either 0 or 1, depending on whether these circles enclose or not the origin, see Figure II.2(b). We can compute the winding number also using the skew polarization (II.11). The normalized eigenvectors, which are also chiral partners, are $|\psi_\pm\rangle = \frac{1}{\sqrt{2}} \left(\frac{\sqrt{a^2+2ab\cos(k)+b^2}}{a+be^{ik}}, \pm 1 \right)$, and $\mathcal{W} = \oint \frac{\mathrm{d}k}{\pi} i \langle \psi_+ | \psi'_- \rangle$ equals either 0 or 1. All methods above therefore coincide in predicting for the SSH model a non-trivial phase ($\mathcal{W} = 1$) when the intra-cell hopping a is smaller that the inter-cell one b. The distinction between intra and inter-cell hopping depends on the choice of the unit cell and then it

has a physical meaning only when the SSH chain is cut. The energy spectrum in the bulk of the SSH model, for $b \neq a$, is gapped around $E = 0$, see Fig. II.2(a); when the chain is cut in such a way that $b > a$, the energy spectrum exhibits two eigenstates of energy $E = 0$ exponentially localized on opposite edges and opposite sublattices, while, when $a > b$, there are no edge-states in the gap of the spectrum, see Fig. II.3. Thus, the winding number predicts correctly the number of states on each chain's edge according to the bulk-edge correspondence. The edge-states are robust against disorder since they survive as long as the winding number remains unchanged, that means as long as the energy gap remains open. In Fig. II.3(a), we show the energy spectrum of the SSH model with open boundary conditions in both the trivial and non-trivial phases, in this latter, localized edge-states with zero energy are visible. In Fig. II.3(b), we show the energy spectrum when a chiral-preserving spatial disorder is added: the hoppings of the Hamiltonian are multiplied by a factor $(1+\epsilon)$, where ϵ is a random number in the range $[-\Delta/2, \Delta/2]$ with $\Delta = 0.6$. It is clear that, whereas the zero energy edge-states remain unaffected, the unprotected bulk states change their energy when disorder is applied.

II.1.4 Berry-Zak phase

The Berry-Zak phase γ [102, 10] is a fundamental concept, ubiquitous in the study of the topological matter. It appears in the *adiabatic motion* of a particle, is the phase accumulated by the Hamiltonian eigenstates during their parallel transport through the Brillouin zone. Differently from what happens in most of the systems, where the global phase factor of a wave function has no physical meaning, this phase can be observed as in the Aharanov-Bohm effect [103]. More recently, various works have proposed [64, 65] and experimentally realized [63, 66] the observation of this phase.

Let $H(\mathbf{R})$ be an Hamiltonian which depends smoothly on N parameters, $R_i(t)$, $1 \leq i \leq N$. The states $|n(\mathbf{R}(t))\rangle$, multiplied by an arbitrary phase factor, are its instantaneous eigenvectors, satisfying at each time t,

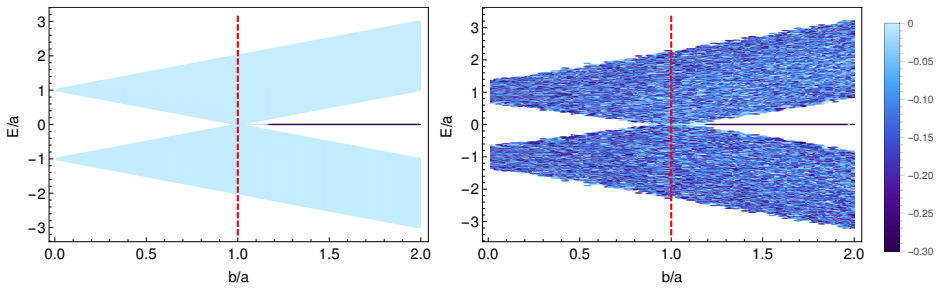

(a) (b)

Figure II.3: **Bulk-edge correspondence in the SSH model. a.** Energy spectrum with open-boundary conditions on a lattice of $2N+1=201$ cells varying the hopping ratio b/a. The color coding of the spectrum indicates the degree of localization $log_{10}(1-|\langle\hat{m}\rangle)|/N)$ of each eigenstate on the two edges $x=-N$, $x=N$; light (dark) colors indicate bulk (edge) states. The red dashed line passing through the point $b=a$ corresponds to the phase transition from trivial ($\mathcal{W}=0$) to topological ($\mathcal{W}=1$). **b.** We have added a chiral-preserving disorder with amplitude $\Delta=0.6$ (see text for details) showing that the edge states are topologically protected.

the relation:

$$H(\mathbf{R}(t))|n(\mathbf{R})\rangle = E_n(\mathbf{R})|n(\mathbf{R})\rangle. \tag{II.13}$$

During the time $t\to T$, each parameter $\mathbf{R}$ defines a continuous curve $\mathcal{C}$ and $|n(\mathbf{R})\rangle$ is smooth along $\mathcal{C}$. Let us assume that at $t=0$ the system's state is $|\psi(t=0)\rangle=|n(\mathbf{R}_0)\rangle$, with $\mathbf{R}_0=\mathbf{R}(t=0)$. The state of the system evolves according to the time-dependent Schrodinger equation:

$$i\frac{d}{dt}|\psi(t)\rangle = H(\mathbf{R}(t))|\psi(t)\rangle. \tag{II.14}$$

In the *adiabatic approximation*, the variation of $\mathbf{R}(t)$ along $\mathcal{C}$ is slow compared to the frequencies corresponding to the energy gaps $|E_n(\mathbf{R})-E_{n\pm1}(\mathbf{R})|$, and then the system remains in the energy eigenstate $|n(\mathbf{R})\rangle$ only picking

up a phase:

$$|\psi(t)\rangle = e^{i\phi_n(t)} e^{-i\int_0^t E_n(\mathbf{R}(t'))dt'} |n(\mathbf{R}(t))\rangle. \tag{II.15}$$

Putting Eq. (II.15) in Eq. (II.14) and projecting on $|n(\mathbf{R})\rangle$, we find:

$$\phi_n = \int_{\mathcal{C}} i\langle n(\mathbf{R})|\partial_{\mathbf{R}}|n(\mathbf{R})\rangle d\mathbf{R}. \tag{II.16}$$

$i\langle n(\mathbf{R})|\partial_{\mathbf{R}}|n(\mathbf{R})\rangle$ is called *Berry connection* and is denoted as $\mathcal{A}^{(n)}(\mathbf{R})$ [10].

$\mathcal{A}^{(n)}$ is not a gauge invariant quantity, and therefore γ_n in general is not gauge invariant unless $\mathcal{C}$ is a closed path. If $\mathcal{C}$ is a closed line, Eq. (II.16) gives the Berry phase:

$$\gamma_n = i \oint \mathrm{d}R\langle n(R)|\partial_R|n(R)\rangle. \tag{II.17}$$

When the slowly varying parameter R is the quasi-momentum k, and the integral in Eq. (II.17) is taken over the Brillouin zone, the Berry phase is called Zak phase [104]. In a chiral-symmetric Hamiltonian, the Zak phase is equal to $\mathcal{W}\pi$ modulo 2π.

II.1.5 Bulk polarization and Zak phase

A physical manifestation of the Zak phase is the bulk polarization of a band insulator [105, 10]. The polarization of a neutral molecule is defined as the difference between the centre of mass' positions of negative and positive charges. According to this definition, the bulk polarization of a band insulator with a fully occupied valence band, is simply the mean position of the centre of the negative charges. This quantity cannot be found straightforwardly working in the basis of the energy eigenstates, since these latter are Bloch waves delocalized over all the bulk. One has to use a complete orthonormal set of localized states, the *Wannier states* [106, 107, 105].

In the simple case of a 1D insulator with only one occupied band, the bulk polarization is the Zak phase of the occupied band divided by

2π, [107, 105]. For each quasi-momentum k in the Brillouin zone, the energy eigenstates are Bloch functions:

$$|\Psi_i(k)\rangle = |k\rangle \otimes |\psi_i(k)\rangle = \frac{1}{\sqrt{N}} \sum_{m=1}^{N} e^{i\alpha(k)} e^{imk} |m\rangle \otimes |\psi_i(k)\rangle, \tag{II.18}$$

where $|\psi_i(k)\rangle$ are the eigenstates of the Bloch Hamiltonian, i is the band index and $\alpha(k)$ is an arbitrary phase factor. We can omit the band index i since we are considering the case in which only the lowest band is occupied.

The Wannier states $|w(j)\rangle$ should fulfill the following set of properties:

- $\langle w(j)|w(j')\rangle = \delta_{jj'}$
- $\sum_{j=1}^{N} |w(j)\rangle\langle w(j)| = \sum_{k\in B.Z.} |\Psi(k)\rangle\langle\Psi(k)|$
- $\langle m+1|w(j+1)\rangle = \langle m|w(j)\rangle$
- $\langle w(j)|m\rangle\langle m|w(j)\rangle < e^{-|j-m|/\xi}$, with ξ some finite localization length.

We can find such a wave-function performing the inverse Fourier transform of the Bloch function of the occupied band,

$$|w(j)\rangle = \frac{1}{\sqrt{2\pi}} \oint \mathrm{d}k e^{-ijk} e^{i\alpha(k)} |\Psi(k)\rangle, \tag{II.19}$$

and setting $\alpha(k)$ in order to make them as localized as possible. In the thermodynamic limit $N \to \infty$, the average position of a Wannier state can be calculated easily writing the position operator in quasi-momentum space $\hat{m} = i\partial_k$:

$$\langle w(j)|\hat{m}|w(j)\rangle = \frac{i}{2\pi} \oint \mathrm{d}k \langle\psi(k)|\partial_k\psi(k)\rangle + j. \tag{II.20}$$

This equation shows that the centre of each Wannier state is given by the position of the lattice cell where it is exponentially localized, plus the Zak phase of the occupied band divided by 2π. The bulk polarization is simply the sum of the centres of the Wannier states for $j \in [-N/2, N/2]$ divided by N, hence, it corresponds to the Zak phase of the occupied band in units of 2π.

II.2 The Integer Quantum Hall effect

Discovered in the $80s$ [7], the integer quantum Hall effect constitutes a paradigmatic example of topological insulating phase of matter [6]. When a magnetic field is applied on a 2D semi-conductor at very low temperature, the transverse conductivity, *Hall conductivity*, inside the energy gaps is quantized. Its value is proportional to the bulk topological invariant, the total *Chern number* of the occupied energy bands [8]. The system is thus very robust against perturbations: while the gap is open, the Hall conductivity remains the same. Finally, for a system with boundaries, topologically protected current-carrying edge-states arise, their number is proportional to the total Chern number (bulk-edge correspondence), as it has been demonstrated in the seminal papers [11, 12, 13]. The IQHE has been experimentally observed in the last years in a multitude of synthetically engineered systems such as atomic [22, 23], superconducting [108], photonic [24] and acoustic platforms [109, 110, 111].

II.2.1 Integer Quantum Hall effect on the lattice: the Hofstadter model

The Hofstadter Hamiltonian [9] has been used to describe the Integer Quantum Hall effect by Thouless, Kohmoto, Nightingale, and den Nijs in the celebrated TKNN paper [8]. It is a tight-binding model of spinless electrons on a square lattice pierced by a uniform magnetic field, see Fig. II.4:

$$H = -t_x \sum_{\langle j,k\rangle_x} e^{i\theta_{jk}} c_k^\dagger c_j - t_y \sum_{\langle j,k\rangle_y} e^{i\theta_{jk}} c_k^\dagger c_j, \tag{II.21}$$

where the first summation is taken over all the nearest-neighbour sites along the x direction and the second sum along the y direction, and the lattice spacing is set to one. The phase factor θ_{jk} is called the Peierls

phase factor and is defined on a link as:

$$\theta_{jk} = \frac{e}{\hbar}\int_{\mathbf{r}_j}^{\mathbf{r}_k} \mathbf{A}\cdot d\mathbf{l}, \tag{II.22}$$

where $\mathbf{A}$ is the vector potential. The sum of the Peierls phase factors on a plaquette is equal to the magnetic flux per plaquette ϕ in units of the magnetic flux quantum $\phi_0 = \hbar/e$, $\phi = \sum_{plaquette}\theta_{jk}$. We can write the vector potential in the Landau gauge: $\mathbf{A} = Bx\mathbf{I}_y$. Hence, $\theta_{jk} = 0$ for the links along x, and $\theta_{j,k} = 2\pi x\phi$ for the link between (j,k) and $(j,k+1)$ along y.

For a rational magnetic flux $\phi = p/q$, the system is periodic over supercells made by q cells in one direction (x) and one cell in the other (y). Thus, we can still write the eigenvalues problem for the Hamiltonian with periodic boundary conditions in terms of Bloch functions $\psi_{\mathbf{k}}(\mathbf{r}) = e^{i\mathbf{k}\cdot\mathbf{r}}u_{\mathbf{k}}(\mathbf{r})$, obtaining the equation known as *Harper equation* [112] for each discrete position x from 0 to q:

$$E_{\mathbf{k}}u_{\mathbf{k}}(x) = -t_x e^{ik_x}u_{\mathbf{k}}(x+1) - t_x e^{-ik_x}u_{\mathbf{k}}(x-1) - 2t_y\cos(2\pi x\phi + k_y)u_{\mathbf{k}}(x). \tag{II.23}$$

For t_x and $t_y \neq 0$, the energy spectrum is made by q bands.

II.2.2 Chern number and Hall conductivity

In SubSec. II.1.4, we considered a Hamiltonian with a periodic dependence from a slowly varying parameter $\mathbf{R}$ which, during a period T, defines a closed curve $\mathcal{C}$. For an energy band separated from the other bands by a finite gap, we defined the Berry connection of the n-th band as the vector $\mathcal{A}^{(n)}(\mathbf{R}) = i\langle n(\mathbf{R})|\partial_{\mathbf{R}}|n(\mathbf{R})\rangle$, where $|n(\mathbf{R})\rangle$ is the eigenvector of energy E_n. In 2D, starting from the Berry connection, we can define a gauge invariant pseudo-vector:

$$\mathbf{\Omega}^{(n)}(\mathbf{R}) = \nabla_{\mathbf{R}}\times\mathcal{A}^{(n)}(\mathbf{R}). \tag{II.24}$$

The second-rank tensor $\Omega_{\mu\nu}$, related to the pseudo-vector above through the Levi-Civita tensor $\Omega^{(n)}_{\mu\nu} = \epsilon_{\mu\nu\xi}\Omega^{(n)}_{\xi}$, is called *Berry curvature* [10]. When

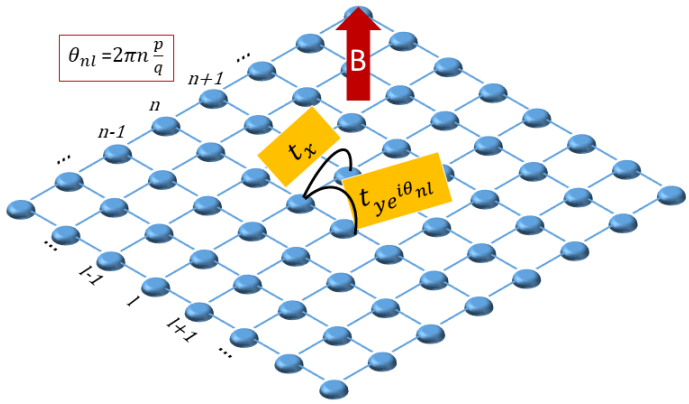

Figure II.4: **Hofstadter model**. The Hofstadter model [9] is a tight-binding model of spin-less electrons on a square lattice pierced by a uniform magnetic field, the lattice spacing is taken to be unity. The phase factor θ_{jk} is the Peierls phase factor defined on a link and represents the magnetic flux through the lattice plaquette. We chose a gauge in which this phase only enters the hopping along y. The magnetic flux per plaquette is a rational number p/q, this defines a magnetic super-lattice made of q cells in the x direction and one in the y direction.

the parameter $\mathbf{R}$ is the quasi-momentum $\mathbf{k}$ which varies on the Brillouin torus, the Berry curvature of the n-th band reads:

$$\Omega_{xy}^{(n)}(\mathbf{k}) = -i\left(\langle\partial_{k_x}u_{\mathbf{k}}^{(n)}|\partial_{k_y}u_{\mathbf{k}}^{(n)}\rangle - \langle\partial_{k_y}u_{\mathbf{k}}^{(n)}|\partial_{k_x}u_{\mathbf{k}}^{(n)}\rangle\right). \tag{II.25}$$

The Chern number of the n-th band is defined as:

$$\nu^{(n)} = \frac{1}{2\pi}\int_{BZ} \mathrm{d}\mathbf{k}\Omega_{xy}^{(n)}(\mathbf{k}), \tag{II.26}$$

where $\int_{BZ}\mathrm{d}\mathbf{k}$ is the integral over the Brillouin torus. The Chern number is an integer topological number: it keeps its value under continuous de-

formations of the band, as long as the gap separating it from the others does not close [10].

Following the proof given in the TKNN paper [8], one can use the Kubo formula to compute the Hall conductivity $\sigma_H \equiv \sigma_{xy}$. When the system is at zero temperature and the Fermi energy is in an energy gap, the Kubo formula gives:

$$\sigma_H \equiv \sigma_{xy} = \frac{2\hbar e^2}{(2\pi)^2} \sum_{E_i<E_F, E_j>E_F} \int_{BZ} \mathrm{d}\mathbf{k} \frac{\mathrm{Im}[\langle u^i_{\mathbf{k}}|v_x|u^j_{\mathbf{k}}\rangle\langle u^j_{\mathbf{k}}|v_y|u^i_{\mathbf{k}}\rangle]}{(E_i(\mathbf{k}) - E_j(\mathbf{k}))^2} \tag{II.27}$$

$$= \frac{2e^2}{(2\pi)^2\hbar} \sum_{E_i<E_F, E_j>E_F} \int_{BZ} \mathrm{d}\mathbf{k} \frac{\mathrm{Im}[\langle u^i_{\mathbf{k}}|\partial_{k_x} H_{\mathbf{k}}|u^j_{\mathbf{k}}\rangle\langle u^j_{\mathbf{k}}|\partial_{k_y} H_{\mathbf{k}}|u^i_{\mathbf{k}}\rangle]}{(E_i(\mathbf{k}) - E_j(\mathbf{k}))^2},$$

where we implicitly used the equality $\mathbf{v} = \frac{1}{\hbar}\nabla_{\mathbf{k}} H(\mathbf{k})$. Using the identity:

$$\sum_{E_i<E_F, E_j>E_F} \frac{\mathrm{Im}[\langle u^i_{\mathbf{k}}|\partial_{k_x} H_{\mathbf{k}}|u^j_{\mathbf{k}}\rangle\langle u^j_{\mathbf{k}}|\partial_{k_y} H_{\mathbf{k}}|u^i_{\mathbf{k}}\rangle]}{(E_i(\mathbf{k}) - E_j(\mathbf{k}))^2} = \tag{II.28}$$

$$\mathrm{Im} \sum_{i\in occ.} \langle \partial_{k_x} u^{(i)}_{\mathbf{k}} | \partial_{k_y} u^{(i)}_{\mathbf{k}} \rangle = -\frac{1}{2}\Omega^{(i)}_{xy}(\mathbf{k}),$$

we find:

$$\sigma_H = \frac{e^2}{h} \sum_{i\in occ.} \nu^{(i)}. \tag{II.29}$$

Hence, when an external electric field E^y acts on n filled bands of electrons, the transverse (Hall) current density follows the linear relation:

$$j_x = E^y \sigma_{yx} = \frac{e^2}{h} E^y \sum_{i=0}^{n} \nu^{(i)} = \frac{e^2}{h} E^y \mathcal{V}^{(n)}, \tag{II.30}$$

where $\mathcal{V}^{(n)}$ is the total Chern number of the first n bands.

This Hall response is robust while the gap remains open; for example, it does not change under small changes of the magnetic flux. This is the origin of the plateaus in the plot of the Hall conductivity versus the magnetic field which benchmark the IQHE [7].

II.2.3 Hall conductivity and the normalized density of particle

We can relate the Hall conductivity with the normalized density of particles of the Hofstadter model through a purely geometrical consideration [113]. However, this result is very general as it applies to all the Chern insulators with a fixed number of particles [114]. The label r of the r-th energy gap and the integers p and q giving the magnetic flux per plaquette ϕ are linked by a Diophantine equation:

$$r = pt_r + qs_r, \tag{II.31}$$

where $0 \leq r < q$, t_r and s_r are integers and $|t_r| < \frac{q}{2}$. For a system with a fixed number of particles and r filled bands, the normalized density of particles is given by the number of filled bands divided by the total number of bands, i.e. $\mathcal{N}_r = \frac{r}{q}$, hence:

$$\mathcal{N}_r = \phi t_r + s_r. \tag{II.32}$$

The Streda formula [115] predicts the response of the density of particles of the system to small changing of the perpendicular magnetic field:

$$\sigma_H = \frac{e^2}{h}\frac{\partial \mathcal{N}}{\partial B}. \tag{II.33}$$

Then Eq. II.32 reads

$$\mathcal{N}_r = \phi \mathcal{V}^{(r)} + s_r. \tag{II.34}$$

Figure II.5 shows the *Hofstadter butterfly* [9], namely the projection of the energy spectrum of the Hofstadter model with periodic boundary conditions for different values of the rational magnetic flux $\phi = p/q$ in the range $[0, 1]$. This plot exhibits a fractal structure of the energy gaps. The Hall conductivity is quantized and constant inside each gap, we used Eq. (II.34) to compute its values and we associated to each value a color in a scale going from blue to red.

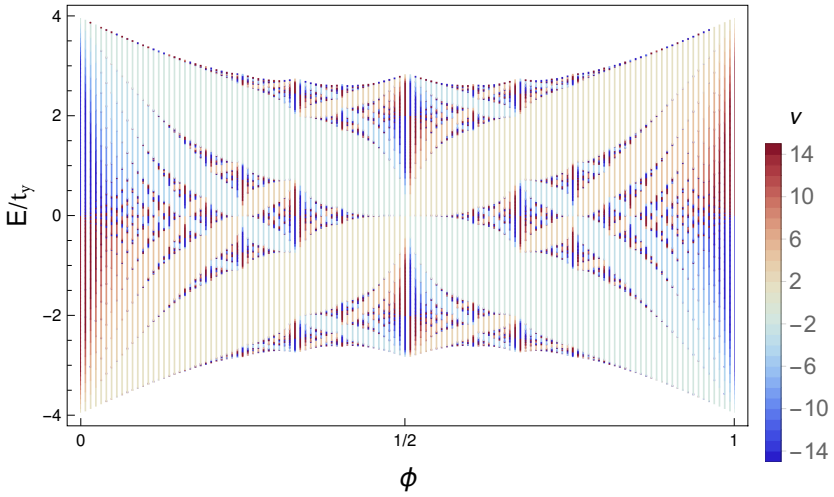

Figure II.5: **Hofstadter butterfly**. Energy spectrum (projection) of the Hofstadter model within periodic boundary conditions changing the flux per plaquette ϕ, for $t_x = t_y = 1$. The plot shows a fractal structure with energy gaps, the transverse conductivities inside the gaps are quantized, their values have been computed using Eq. (II.34) and are associated with a colour going from blue to red.

II.2.4 Hofstadter model on the cylinder

If we consider the Hofstadter Hamiltonian on a cylinder, i.e. with periodic boundary conditions along y and open boundary conditions along x, states with energy laying in the gaps of the bulk energy spectrum arise on each edge; their number is equal to the total Chern number of the filled bands. This bulk-edge correspondence can be understood with the socalled *Thouless' pump argument* [13]. In a cylindrical configuration, the effect of a constant electric field E_y is to shift the quasi-momentum k_y, since $\dot{k}_y = \frac{-eE_y}{\hbar}$. It works as a periodic pump which in a period $T = \frac{2\pi}{e|E_y|}$ pushes across the bulk region a number of electrons equal

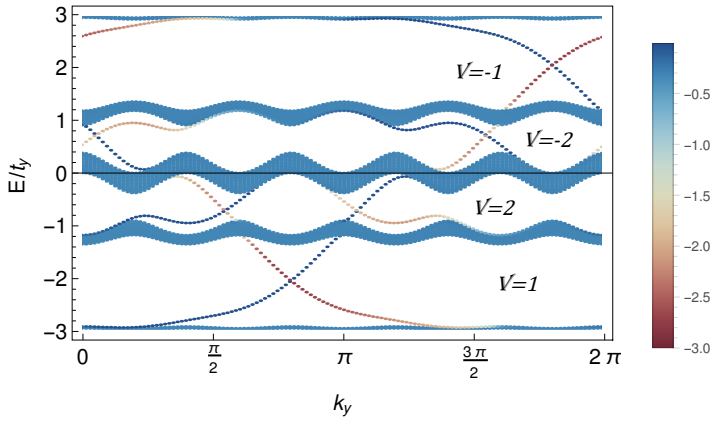

Figure II.6: **Spectrum of the Hofstadter model on a cylinder.** The rational flux is fixed to $\phi = 1/5$, $t_x = t_y = 1$ and the number of cells in the x direction is $2N_x + 1 = 401$. The color of each energy value indicates the degree of localization of the corresponding eigenstate ψ on the edges $x = -N_x$ (dark blue) and $x = N_x$ (red), i.e. the value of the function $log_{10}[1 - \langle\hat{x}\rangle_\psi]/N_x$. The integers labelling the gaps are the total Chern numbers of the bands below. In agreement with the bulk-edge correspondence, they count correctly the number of edge-states (for each edge) which traverse the corresponding gap during the pumping.

to the total Chern number. Figure II.6 shows the energy spectrum of the Hofstadter Hamiltonian with $\phi = 1/5$ and with periodic boundary conditions on y and open boundary conditions on x (cylindrical geometry) while shifting k_y from 0 to 2π. Since $\phi = 1/5$, the spectrum is made of 5 energy bands; the total Chern number under the n-th gap, $\mathcal{V}^{(n)}$, counts the number of edge-states crossing the gap during the pumping cycle. The sign of $\mathcal{V}^{(n)}$ corresponds to the chirality of the modes on one edge, i.e. the sign of their group velocity. Let us consider the Harper equation (II.23) with cylindrical boundary conditions, and let us replace the quasi-momentum component k_y with a parameter ξ_x called phason

varying in the same range $[0, 2\pi]$. We get a family of Hamiltonians labelled by ξ_x:

$$H(\xi_x) = \sum_x \left[t c_x^\dagger c_{x+1} + h.c. + \lambda \cos(2\pi\phi x + \xi_x) c_x^\dagger c_x \right]. \tag{II.35}$$

The energy spectrum of each $H(\xi_x)$ is gapped but, exactly as the original 2D Hamiltonian, it does not posses any discrete nonspatial symmetry. While in 2D, the absence of symmetries corresponds to the topological Chern class, in 1D, it corresponds to the topological triviality [3]. Then the single $H(\xi_x)$ is topologically trivial, but the union of the $H(\xi_x)$ for all the values of ξ_x in the period is topologically non-trivial: the topological invariant associated to this family of Hamiltonians is the Chern number of the corresponding 2D system. In Refs. [116] and [117], it is demonstrated that when the parameter ϕ in Eq. (II.35) is incommensurate with the lattice length, for example when ϕ is an irrational number, the integration over all the values of ξ_x is not needed and one can associate the same Chern number to every $H(\xi_x)$ in the family. The fact that ϕ is incommensurate with the lattice length makes the system quasi-periodic, namely a *quasi-crystal* (QC). Equation (II.35) with an irrational ϕ is known as Aubry-Andrè quasi-crystal (AAQC) [118]. If edges are introduced in such a system, topologically protected edge states arise. Changing adiabatically the parameter ξ_x these modes cross the energy gaps. In Ref. [116], this phenomenon has been observed in a AAQC implemented with an array of optical fibers. Another quasi-crystal is the celebrated Fibonacci quasi-crystal (FQC) [119]; interestingly, the AAQC and the FQC have been proven to be topologically equivalent [120].

III

Detecting the winding number in the bulk of a 1D chiral model

In this chapter we present a method to extract the winding number $\mathcal{W}$ of a 1D chiral-symmetric non-interacting system from the free bulk dynamics of the single particle. We find that $\mathcal{W}$ emerges in the long time limit of an observable, the *mean chiral displacement* (MCD), measured over initially localized states. This detection requires no precise knowledge about the Hamiltonian's details (apart from the fact that it is chiral symmetric), and it simply relies on the detection of the average position of the particle's wavepacket within each sublattice. Our detection method does not require any kind of external intervention on the system, such as interferometric architectures [63, 66, 64, 65], introduction of losses [85, 86, 87], or scattering measurements [68] and it does not require the access to the system's edges [76, 49]. This feature makes this method suitable in simulation platforms where the chiral lattice is encoded in a degree of freedom which has no physical edges, as for example in Ref. [71].

In Sec. III.1, which is based on Ref. [83], we derive our result in the

case of an infinite, clean, chiral system with an arbitrary (even) number of sites per unit cell: we demonstrate the relation between MCD and winding number analytically in terms of spectral projectors written in quasi-momentum space. In SubSec. III.1.2, and III.1.3, we apply our method to two models extracting their winding numbers from the numerical simulations of their dynamics. All the figures of this section are adapted from Ref. [83].

In Sec. III.2, we show that the MCD detects the winding number also in systems with a strong chiral-preserving disorder. In SubSec. III.2.1, we derive the relation between MCD and winding number in presence of disorder. In SubSec. III.2.2, we present the experiment reported in [50]; here the MCD measurement has been used to detect a signature of the topological Anderson insulating phase (TAI) in a disordered chiral-symmetric wire simulated with ultra-cold atoms. All the figures in this subsection are adapted from Ref. [50].

III.1 Detection of the winding number in translationally invariant systems

III.1.1 Winding number and mean chiral displacement in quasi-momentum space

Let us consider a non-interacting tight-binding chiral Hamiltonian on a lattice of N unit cells, and $\mathcal{D}$ (even) sites per unit cell. We describe a particle moving in such a system using as basis a set of localized wavefunctions:

$$\overline{|\psi_j\rangle} = \oint \frac{\mathrm{d}k}{\sqrt{2\pi}} |\psi_j\rangle, \tag{III.1}$$

where $|\psi_j(k)\rangle$ are the eigenstates of the Bloch Hamiltonian with $j = \pm 1, \ldots, \pm\mathcal{D}/2$. The generic state written in this basis reads:

$$\overline{|\Psi\rangle} = \sum_j c_j \overline{|\psi_j\rangle} = \sum_j c_j \oint \frac{\mathrm{d}k}{\sqrt{2\pi}} |\psi_j\rangle = \oint \frac{\mathrm{d}k}{\sqrt{2\pi}} \sum_j c_j |\psi_j\rangle = \oint \frac{\mathrm{d}k}{\sqrt{2\pi}} |\Psi\rangle, \tag{III.2}$$

where c_j are complex coefficients which do not depend on k. Comparing expression (III.1) with (II.19) it is clear that $\overline{|\psi_j\rangle}$ are Wannier functions localized in the central site of the lattice, $m = 0$, with a particular choice of the phase $\alpha(k)$, namely $\alpha(k) = 0$ for all values of the quasi-momentum k. In the following demonstrations, we will use a particular subclass of these localized functions, the *chiral localized states* $\overline{|\Gamma_j\rangle}$:

$$\overline{|\Gamma_j\rangle} = \frac{\mathrm{sgn}(j)\overline{|\psi_j\rangle} + \overline{|\psi_{-j}\rangle}}{\sqrt{2}} = \oint \frac{\mathrm{d}k}{\sqrt{2\pi}} |\Gamma_j\rangle. \tag{III.3}$$

These states are eigenstates of the partial chiral operator, Eq. (II.3), such that $\Gamma_j|\Gamma_{j'}\rangle = \delta_{jj'}\mathrm{sgn}(j)|\Gamma_j\rangle$. The average value of the partial Q operator, Eq. (II.8), evaluated on them yields $\langle Q_j\rangle_{\Gamma_{j'}} = 0$.

We now introduce the position operator $\hat{m}$ (where the integers m label whole unit cells, as shown in Fig. III.1), and the *chiral position* operator $\widehat{\Gamma m} \equiv \Gamma\hat{m}$. From now on we will set to unity the length of the unit cell. The position operator in momentum space is represented as usual by a derivative,

$$\begin{aligned} \langle k|\hat{m}|\tilde{k}\rangle &= \sum_{m,\tilde{m}} \langle k|m\rangle\langle m|\hat{m}|\tilde{m}\rangle\langle\tilde{m}|\tilde{k}\rangle \\ &= \sum_{m,\tilde{m}} m\delta(m-\tilde{m}) \frac{e^{i(\tilde{k}\tilde{m}-km)}}{2\pi} = i\partial_k \sum_m \frac{e^{i(\tilde{k}-k)m}}{2\pi} = i\partial_k\delta(\tilde{k}-k). \end{aligned} \tag{III.4}$$

The average displacement at time t for a particle starting from the state

$\overline{|\Psi\rangle}$ is given by:

$$\langle \hat{m}(t)\rangle_{\overline{\Psi}} = \oint \frac{\mathrm{d}k}{2\pi}\langle U^{-t}(i\partial_k)U^t\rangle_\Psi = \sum_{j=1}^{\mathcal{D}/2}\oint \frac{\mathrm{d}k}{2\pi}\Big\{t\partial_k E_j\langle Q_j\rangle_\Psi \tag{III.5}$$
$$+ \mathcal{S}_j\sin(2tE_j)\langle iQ_j\Gamma_j\rangle_\Psi - \mathcal{S}_j[1-\cos(2tE_j)]\langle\Gamma_j\rangle_\Psi\Big\}$$
$$+ \sum_{j,j'=-1 \text{ and } |j|\neq|j'|}^{\mathcal{D}/2}\oint \frac{\mathrm{d}k}{2\pi} i\langle\psi_j|\psi'_{j'}\rangle\langle\Psi|\psi_j\rangle\langle\psi_{j'}|\Psi\rangle e^{it(E_j-E_{j'})},$$

where $U^t \equiv e^{-iHt}$ is the unitary evolution operator, $U^{-t} \equiv e^{iHt}$ is its inverse and $\mathcal{S}_j$ is the skew polarization introduced in SubSec. II.1.2. The explicit derivation of Eq. (III.5) is given in App. VII.1.1. When evaluated on the chiral localized states $\overline{|\Gamma_j\rangle}$, the mean displacement reduces to

$$\langle \hat{m}(t)\rangle_{\overline{\Gamma_j}} = -\mathrm{sgn}(j)\oint \frac{\mathrm{d}k}{2\pi}\mathcal{S}_j[1-\cos(2tE_j)]. \tag{III.6}$$

Let us now define the *chiral average displacement* as:

$$\langle\Gamma\cdot\hat{m}(t)\rangle_{\overline{\Psi}} \equiv \oint \frac{\mathrm{d}k}{2\pi}\langle\Gamma U^{-t}(i\partial_k)U^t\rangle_\Psi = \oint \frac{\mathrm{d}k}{2\pi}\langle U^t\Gamma(i\partial_k)U^t\rangle_\Psi, \tag{III.7}$$

and the *mean chiral displacement* as:

$$\langle\widehat{\Gamma m}(t)\rangle_{\overline{\Psi}} \equiv \oint \frac{\mathrm{d}k}{2\pi}\langle U^{-t}\Gamma(i\partial_k)U^t\rangle_\Psi. \tag{III.8}$$

Using Eq. (III.6), we find that, in the long-time limit, $\langle\Gamma\cdot\hat{m}(t)\rangle_{\overline{\Gamma_j}}$, when summed on the chiral localized states with $j>0$, converges to minus one half of the winding number $\mathcal{W}$ (see App. VII.1.2 for details):

$$\sum_{j=1}^{\mathcal{D}/2}\langle\Gamma\cdot\hat{m}(t)\rangle_{\overline{\Gamma_j}} = \sum_{j=1}^{\mathcal{D}/2}\langle\hat{m}(t)\rangle_{\overline{\Gamma_j}} = \sum_{j=1}^{\mathcal{D}/2}\oint\frac{\mathrm{d}k}{2\pi}\mathcal{S}_j[-1+\cos(2tE_j)] \tag{III.9}$$
$$= -\frac{\mathcal{W}}{2} + \sum_{j=1}^{\mathcal{D}/2}\oint\frac{\mathrm{d}k}{2\pi}\mathcal{S}_j\cos(2tE_j) = -\frac{\mathcal{W}}{2}+\dots.$$

We find a similar result for $\langle\widehat{\Gamma m}(t)\rangle_{\overline{\Gamma_j}}$:

$$\sum_{j=1}^{\mathcal{D}/2}\langle\widehat{\Gamma m}(t)\rangle_{\overline{\Gamma_j}}=\sum_{j=1}^{\mathcal{D}/2}\langle\widehat{\Gamma m}(t)\rangle_{\overline{\psi_j}}=\sum_{j=1}^{\mathcal{D}/2}\oint\frac{\mathrm{d}k}{2\pi}\mathcal{S}_j[1-\cos(2tE_j)]=\frac{\mathcal{W}}{2}+\ldots, \tag{III.10}$$

The expressions (III.9) and (III.10) are invariant under the change of j to $-j$, as the skew polarization is invariant under such change. Therefore, we can compute the traces over all the $\mathcal{D}$ chiral localized states:

$$-\operatorname{Tr}[\Gamma\cdot\hat{m}(t)]=\operatorname{Tr}[\widehat{\Gamma m}(t)]=2\sum_{j=1}^{\mathcal{D}/2}\oint\frac{\mathrm{d}k}{2\pi}\mathcal{S}_j[1-\cos(2tE_j)]=\mathcal{W}+\ldots, \tag{III.11}$$

As the trace does not depend of the choice of the basis, these results imply that a trace taken on any set of $\mathcal{D}$ vectors forming a complete basis of the unit cell will converge to the winding number $\mathcal{W}$ in the long time limit. At topological critical points, the mean chiral displacement converges to the average of the invariants computed in the two neighboring phases in agreement with Ref. [121].

As we derive in App. VII.1.2, when $\mathcal{D}=2$, the contribution of the two sub-lattice sites $A(+)$ and $B(-)$ is the same, and the trace of the mean chiral displacement can be rewritten as:

$$\mathcal{C}(t)=\operatorname{Tr}[\widehat{\Gamma m}(t)]=2\langle\widehat{\Gamma m}(t)\rangle_{\overline{|\psi_+\rangle}}=2\oint\frac{\mathrm{d}k}{2\pi}i\langle\psi_+|\psi'_-\rangle[1-\cos(2tE)]=\mathcal{W}+\ldots, \tag{III.12}$$

From now on, we will refer to the trace of the mean chiral displacement, $\mathcal{C}(t)$ as to MCD.

In the following subsections, we will benchmark our method on two concrete Chiral Hamiltonians. The first model is a direct generalization of the SSH model with four sites per unit cell, and the second one is an SSH model with staggered long-range hopping which possesses a richer topological diagram with phases corresponding to winding numbers ±1, 0 and ±2.

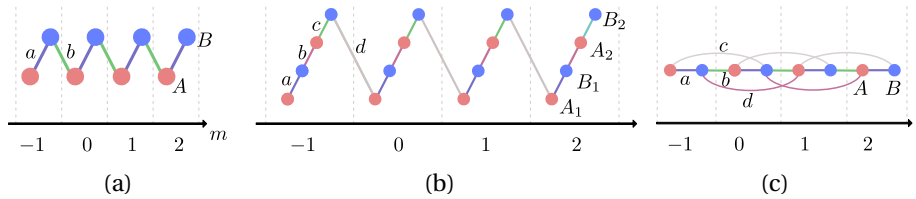

Figure III.1: **1D chiral models**. Sketch of the SSH (**a**), the SSH_4 (**b**) and the SSH model with staggered long range hoppings (**c**). Red and blue sites belong respectively to the A and B sublattices, thin lines denote hoppings, and the unit cells of the lattice are indexed by the integer m. The corresponding Hamiltonians are explicitly chiral, as these contain no term coupling a sublattice directly with itself.

III.1.2 The SSH_4 model

We now discuss an example of chiral model with $\mathcal{D} = 4$. This model is a direct generalization of the SSH model (Fig. III.1(a)), we will refer to it as to SSH_4. The SSH_4 has a non-interacting Hamiltonian with nearest-neighbour hoppings. As shown in Fig. III.1(b), the system is a Bravais lattice with a four atom unit cell of sites A_1, B_1, A_2, B_2. The intra-cell hoppings are a, b and c, the inter-cell hopping is d. The Hamiltonian defines two sublattices, containing two sites each: $A = \{A_1, A_2\}$, and $B = \{B_1, B_2\}$. Since the Hamiltonian contains no term acting within a given sublattice, the model is chiral for arbitrary values of $\{a, b, c, d\}$. The model belongs to class AIII when the tunnelings are complex numbers and hence the TRS is broken, while it belongs to the more constrained class BDI if all tunnelings are purely real [3]. We will for simplicity restrict ourselves to the latter case, but note that our results hold for all 1D chiral models, i.e., also for AIII ones, such as the one considered in Ref. [50]. Finally, note that for $a = c$ and $d = b$, the SSH_4 reduces to the usual SSH model, shown in Fig. III.1(a). In the canonical basis $\{\psi_{A_1}, \psi_{A_2}, \psi_{B_1}, \psi_{B_2}\}$,

the Bloch Hamiltonian assumes the off-diagonal form

$$H(k) = \begin{pmatrix} 0 & h^\dagger(k) \\ h(k) & 0 \end{pmatrix} = \begin{pmatrix} 0 & 0 & a & de^{-ik} \\ 0 & 0 & b & c \\ a & b & 0 & 0 \\ de^{ik} & c & 0 & 0 \end{pmatrix}. \tag{III.13}$$

The energy spectrum and the eigenvectors of the different bands may be found analytically (see App. VII.1.3 for details). The corresponding windings are computed from Eq. (II.7), and by direct integration one finds $\mathcal{W} = 0$ when $ac > bd$, and $\mathcal{W} = 1$ when $ac < bd$. Figure III.4(a) shows the energy spectrum for $a = c = d$ and for different values of b. The gap closing appears at $b = 1$, as it is the case for the SSH model. Figure III.4(b) shows the winding number in terms of b (solid line). The yellow and green dashed lines are the separate contributions of the two pairs of chiral partners to the total winding number. The separate contributions are not quantized, but their sum is. Finally, the insets show parametric plots of the determinant of h, which performs a circle in the complex plane as k traverses the Brillouin zone. In the topological phase, the circle contains the origin (right inset) whereas in the trivial phase the circle does not contain the origin (left inset).

Measuring the winding number of the SSH$_4$ in real space

We simulate the dynamics of a finite system of 200 unit cells. We prepare localized initial states at the center of the chain $m = 0$, and we let them evolve under the SSH$_4$ Hamiltonian. In particular, we choose as initial states two different bases of the internal space: the chiral basis, and an arbitrary basis. At each time t, we compute (minus) the trace of the chiral average displacement $-\mathrm{Tr}[\Gamma \cdot \hat{m}(t)]$ (Eq. (III.9)) on the chiral basis, and the trace of the mean chiral displacement $\mathrm{Tr}[\widehat{\Gamma m}(t)]$ (Eq. (III.11)) on an arbitrary basis. With the choice of the unit cell $\{\psi_{A_1}, \psi_{B_1}, \psi_{A_2}, \psi_{B_2}\}$, in real space these operators are simply represented by the diagonal matrices $\hat{m} = \mathrm{diag}(\ldots, 1, 1, 1, 1, 2, 2, 2, 2, \ldots)$ and $\widehat{\Gamma m} = \mathrm{diag}(\ldots, 1, -1, 1, -1, 2, -2, 2, -2, \ldots)$.

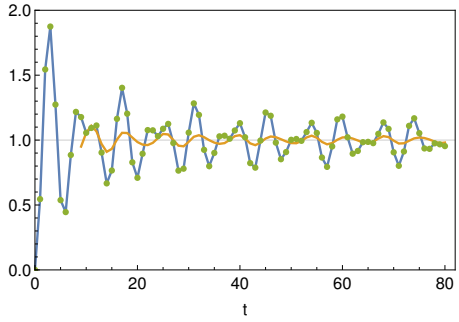

Figure III.2: **Traces of mean chiral and of chiral average displacements of the SSH_4 model.** Parameters are chosen in the topological phase: $\{a,b,c,d\} = \{1, 2.5, 0.3, 0.6\}$, so that $bd > ac$ and $\mathcal{W} = 1$. There are 2 completely superposed series of dots, showing the results of the two observables discussed in the text, and the blue line shows the analytical result, Eq. (III.11). The yellow line shows a sliding average of the data, which rapidly converges to the expected value of 1.

Figure III.2 shows the results of the numerical simulations for the SSH_4 model. The two traces in the different bases are superimposed (green dots), and match perfectly with the theoretical curve (blue curve) given in Eq. (III.11). In the figure we also show a sliding average of the data over ten points (orange curve), which shows a smoother and quicker convergence to the winding number.

Finally, let us note that the simplest procedure which yields the desired result (the winding) is to follow Eq. (III.9) and take the sum of the mean displacement measured over two orthogonal states which are completely localized on the central unit cell, and which form a complete basis of the left sublattice (the one corresponding to the +1 eigenvalue of the chiral operator). Minus two times this quantity will give the result plotted in Fig. III.2. Explicitly, e.g., two states of the form $\bar{\Psi}_a = (0,\ldots,0,\mathbf{1},\mathbf{0},\mathbf{0},\mathbf{0},0,\ldots,0)$ and $\bar{\Psi}_b = (0,\ldots,0,\mathbf{0},\mathbf{1},\mathbf{0},\mathbf{0},0,\ldots,0)$, where the four central num-

bers (marked in bold) indicate the amplitudes on the cell with coordinate $m = 0$ in the basis where the chiral operator is $(1, 1, -1, -1)$.

III.1.3 The SSH model with staggered long range hoppings

In this Section we wish to test the validity of our detection method using a system which exhibits a richer phase diagram ($\mathcal{W} = 0, \pm 1, 2$). To this aim, we study a one-dimensional chiral Hamiltonian, which is a standard SSH model with staggered nearest-neighbor hoppings a and b, and with additional staggered third-nearest-neighbor hoppings c and d (that is to say, there is a hopping c between sites 1 and 4, d between sites 2 and 5, c between 3 and 6, and so on). The model is shown schematically in Fig. III.1(c), and given its long-range character we refer to it as the LR-SSH model.

The model can be written in momentum space when using a two-atom unit cell. The corresponding Hamiltonian is a 2×2 matrix,

$$H_{\mathrm{LR}} = \begin{pmatrix} 0 & a + be^{-ik} + ce^{ik} + de^{-2ik} \\ a + be^{ik} + ce^{-ik} + de^{2ik} & 0 \end{pmatrix}. \quad \text{(III.14)}$$

The winding $\mathcal{W}$ of this model equals +2, +1, 0, or -1. The topological phase diagram with $a = b$ is shown in Fig. III.3(a). As shown in Fig. III.3(b), the long time limit of the trace of the mean chiral displacement detects correctly the winding in all topologically distinct regions. In particular, when $c = d = 0$, the model is at the critical point between the phases with $\mathcal{W} = 0$ and $\mathcal{W} = 1$, recovering the expected SSH result, which is critical when $a = b$. In this point, as in all other phase transitions, the mean chiral displacement converges to the intermediate (integer, or half integer) value between the windings of the neighboring phases (see dashed lines in Fig. III.3(b)), as discussed in Ref. [121].

III.1.4 Possible experimental implementations

Various possible experimental scenarios may be envisaged to study chiral models with large internal dimensions. For example, a $\mathcal{D} = 4$ chiral

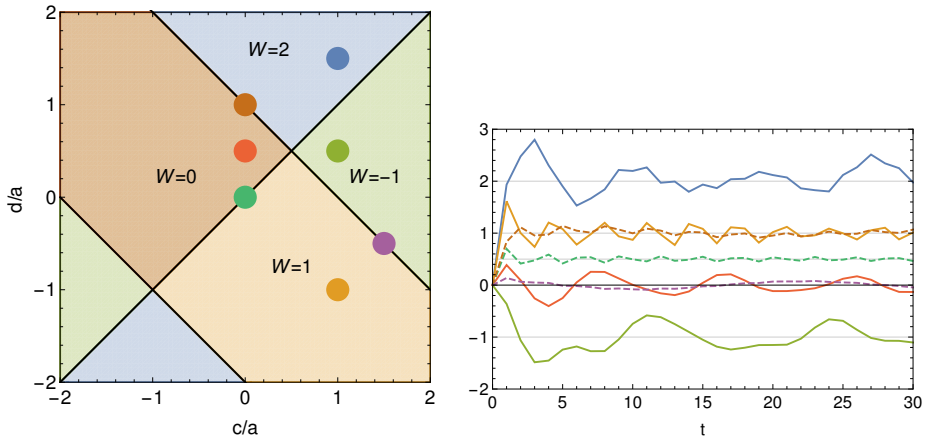

Figure III.3: **Topology of the LR-SSH model. a.** Winding numbers, with $a = b$. **b.** Trace of mean chiral displacement computed for the values of (c, d) indicated by the corresponding dot in the left figure. The three dashed lines correspond to values of the parameters at the border between two phases, where the model is critical; in these cases, the observable remarkably converges to the average of the corresponding invariants.

model with ultracold atoms may be implemented by means of a suitable superlattice as it has been proposed also in Ref. [122]. Three superposed optical lattices with lattice spacings $\lambda/2$, λ, and 2λ effectively realize an SSH_4 model with two equal tunnelings. The three lattices may be obtained from a single laser working at $\lambda_{\text{laser}} = 1064\text{nm}$, which once retroreflected produces an optical potential with lattice spacing $\lambda = \lambda_{\text{laser}}/2$. The $\lambda/2$ lattice may be obtained by retroreflecting the frequency-doubled laser, while the one at 2λ may be obtained by crossing two λ_{laser} beams at a small angle. Otherwise, the superlattice may be by directly imprinted with a spatial light modulator (SLM) or with a digital mirror device (DMD).

Driven models may be realized by periodically pulsed Hamiltonians, such as the one discussed, e.g., in Ref. [44]. Another suitable platform is the synthetic wire implemented in the space of the discrete momentum of a Bose-Einstein condensate in an optical lattice [49, 48, 50] which we will describe in further detail in the following section. In a photonic setting, we envisage to use a lattice of evanescently coupled optical waveguides, where the different hopping amplitudes correspond to different distances between the wave-guides [24]. Finally, the SSH_4 model may be implemented in exciton-polariton experiments, by a slight modification of the approach used by the group of A. Amo in Ref. [123].

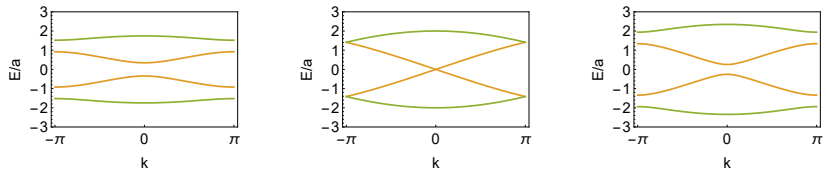

(a)

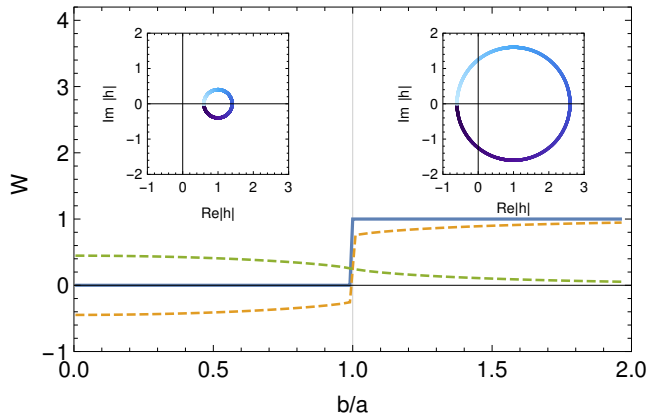

(b)

Figure III.4: **Spectrum and topology of the SSH$_4$ model**. **a.** Energy dispersions for $a = c = d$, and $b/a = 0.4, 1, 1.6$ (from left to right). The model is in the trivial phase for $bd < ac$ ($\mathcal{W} = 0$, left), and in the non-trivial phase for $bd > ac$ ($\mathcal{W} = 1$, right). At the critical point, the two central bands touch at $E = k = 0$ (center). Eventual gap closings between the other bands (such as the one visible in the central figure, at $E/a \approx \pm\pi/2$) have no topological relevance for this model. **b.** Winding number for the SSH$_4$ model with $a = c = d$, as a function of b/a. The yellow and green dashed lines are the separate contributions of the two pairs of chiral partners to the total winding number, respectively $\oint \frac{dk}{\pi}\mathcal{S}_1$ and $\oint \frac{dk}{\pi}\mathcal{S}_2$, while the blue solid line is the actual winding number, given by their sum. The insets display the value of the determinant of $h(k)$ in the complex plane, as k is varied between 0 (blue) to 2π (white).

III.2 Detection of the winding number in disordered systems

III.2.1 Winding number and mean chiral displacement in real space

So far we have dealt with translationally invariant systems where the winding number is simply calculated in momentum space using the Bloch wavefunctions of the energy bands as derived in SubSec. II.1.2. In the presence of disorder, where translational symmetry is broken, the winding number must be computed in real space. A method to derive the winding in real space, valid with periodic boundary conditions, is presented in Ref. [124] and references therein. Here we present an alternative one which can be used also with open boundary conditions. After having derived the winding in real-space for a disordered system, we will derive the MCD and we will prove that these two quantities are still equal in the long-time limit. From now on, we will refer to this real-space winding number using the letter ν.

Let us consider a two-bands Hamiltonian H and the corresponding Q-matrix, $Q = P_+ - P_-$, given in Eq. (II.8). If the original Hamiltonian is chiral, so is the Q-matrix, and it is therefore possible to write it as

$$Q = Q_{AB} + Q_{BA} = \Gamma_A Q \Gamma_B + \Gamma_B Q \Gamma_A, \tag{III.15}$$

where Γ_A, Γ_B are projectors onto the A or B sublattices respectively, and $\Gamma = \Gamma_A - \Gamma_B$ is the chiral operator given in Eq. (II.2). The real-space expression of the winding number proposed in Ref. [124] reads:

$$\nu = \mathcal{T}\{Q_{BA}[X, Q_{AB}]\} = \mathcal{T}\{Q_{BA} X Q_{AB} - Q_{BA} Q_{AB} X\}, \tag{III.16}$$

where $\mathcal{T}$ indicates a "trace per volume" (i.e., per number of unit cells N) and X is the position operator in real space.

In order to compute the winding number within open boundary conditions we modify a formalism introduced by Bianco and Resta for a real-space calculation of the Chern number in quantum Hall insulators, in

Refs. [125, 126]. This method consists of defining a "local topological marker" that depends on the eigenfunctions of the system. This marker gives a local value for a topological invariant when evaluated in a region away from the physical boundary of the system. While this quantity is not exactly quantized, it converges smoothly and rapidly to the integer value of the corresponding invariant in the limit of an infinite system with mild assumptions of homogeneity of the bulk phase. Hence, we use the idea of Bianco and Resta to directly evaluate a symmetrized version of the argument of the trace per volume of Eq. (III.16), over the central part of the chain. Our topological marker then takes the form:

$$\begin{aligned}\nu(j) \equiv & \frac{1}{2}\Big\{(Q_{BA}[X,Q_{AB}])_{jA,jA} + (Q_{BA}[X,Q_{AB}])_{jB,jB} \\ & + (Q_{AB}[Q_{BA},X])_{jA,jA} + (Q_{AB}[Q_{BA},X])_{jB,jB}\Big\} \\ = & \frac{1}{2}\sum_{a=A,B}\Big\{(Q_{BA}[X,Q_{AB}])_{ja,ja} + (Q_{AB}[Q_{BA},X])_{ja,ja}\Big\} \\ = & \sum_{a=A,B}\langle j_a|M|j_a\rangle,\end{aligned} \tag{III.17}$$

where j indicates the lattice site index, the subscripts jA and jB indicate the entries of the matrix corresponding to the A or B sublattice for lattice site j and:

$$M = \frac{Q_{BA}XQ_{AB} - Q_{BA}Q_{AB}X - Q_{AB}XQ_{BA} + Q_{AB}Q_{BA}X}{2}. \tag{III.18}$$

To extract a value for the winding number ν in a disordered system we average $\nu(j)$ over a small region ($\sim N/8$ unit cells with N length of the chain) in the center of the lattice, that is $j = 0$, and over different disorder configurations. In particular we consider a state $|0_a\rangle$, completely localized on the central cell of the chain, either in a site $a = A$ or in a site $a = B$. We project this state on the eigensystem of the Hamiltonian $\{|\phi_i\rangle\}$, with $i = -N,..N$ and energies $E_{-i} = -E_i$ denoting $\langle 0_a|\phi_i\rangle$

with α_{ai}. Note that the Chiral symmetry implies that the states ϕ_i satisfy $|\phi_{-i}\rangle = \Gamma|\phi_i\rangle$. We can now evaluate $\nu(0)$ as:

$$\nu(0) = \sum_{a=A,B} \langle 0_a|M|0_a\rangle = \sum_a \left[\sum_i |\alpha_{ai}|^2 \langle\phi_i|\Gamma X|\phi_i\rangle \right. \tag{III.19}$$
$$\left. + \sum_{i,j<0;i\neq j} \alpha^*_{ai}\alpha_{aj}\langle\phi_i|\Gamma X|\phi_j\rangle + \sum_{i,j>0;i\neq j} \alpha^*_{ai}\alpha_{aj}\langle\phi_i|\Gamma X|\phi_j\rangle \right].$$

The explicit derivation of this result is given in App. VII.2.1. Numerically, we observe that the off-diagonal part of this expression provides a very small contribution (typically $\sim 1\%$ of the total), so that the sum is completely dominated by the diagonal term.

Now, we can derive the real-space formulation of the mean chiral displacement $\mathcal{C}(t)$ whose momentum-space formulation is given in Eq. (III.12). Since the projections α_{ai} of the initial state on the energy eigenstates are effectively randomly distributed variables, upon disorder average, the result from initializing the system on site A is the same as initializing it on site B. Hence, the MCD can be computed as mean value of $2\Gamma X(t)$ over a state initially localized equivalently on either the A or the B site:

$$\mathcal{C}(t) = \langle 0_a|e^{iHt}(2\Gamma X)e^{-iHt}|0_a\rangle = 2\sum_i |\alpha_{ai}|^2\langle\phi_i|\Gamma X|\phi_i\rangle \tag{III.20}$$
$$+ 2\sum_{i\neq j} \alpha^*_{ai}\alpha_{aj}e^{-i(E_j-E_i)t}\langle\phi_i|\Gamma X|\phi_j\rangle,$$

and the disorder-averaged MCD, $\bar{\mathcal{C}}(t)$, is:

$$\bar{\mathcal{C}}(t) \approx \bar{\nu}(0) + ... \tag{III.21}$$

where the dots corresponds to the oscillatory off-diagonal terms which go to zero in the long time limit.

III.2.2 Observation of the Topological Anderson Insulator in a disordered chiral-symmetric wire

Introduction

Here we present the experiment reported in Ref. [50] where the MCD is used to detect disorder-driven topological transitions of a chiral wire implemented in the space of the discrete momentum sates of trapped ultracold atoms. In particular, two phenomena are observed: a transition from a topological phase to a trivial one, and, for the first time, evidences of the the so-called *topological Anderson insulator* (TAI) phase, namely a topological non-trivial phase induced by a strong disorder. The TAI has been first predicted to occur in metallic 2D HgTe/CdTe quantum wells [88], but so far it was never been observed experimentally.

The topological phases are robust against weak symmetry-preserving disorder, but a strong disorder can kill them. In a low-dimensional system, like the one we are considering, a static disorder also causes the *Anderson localization* of the particle wave-functions [127]. Without energy gap, experimental probes relying on the adiabatic transport are expected to fail and thus the measure of the MCD emerges as suitable method to detect the system's topology. During the last phase of our work [50], a related work [128] provided a complementary evidence of the TAI phase through the observation of topological edge states in a 2D photonic waveguides' array.

Experimental platform

We consider the following chiral Hamiltonian in real space:

$$H = \sum_{n=-N/2}^{N/2} \left[m_n c_n^\dagger S c_n + t_n \left(c_{n+1}^\dagger \frac{(\sigma_x - i\sigma_y)}{2} c_n + \text{h.c.} \right) \right], \qquad \text{(III.22)}$$

where $c_n^\dagger = (c_{n,A}^\dagger, c_{n,B}^\dagger)$ creates a particle at unit cell n in sublattice site A or B, c_n is the corresponding annihilation operator, and σ_i are the Pauli

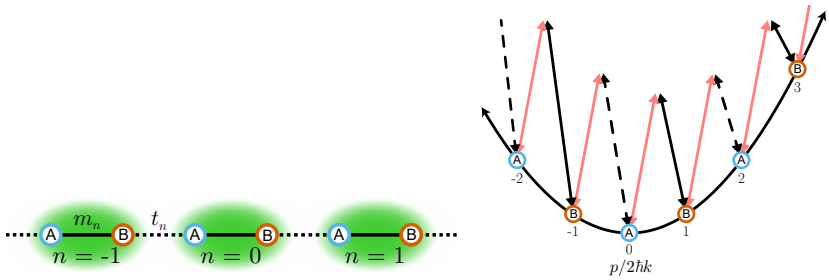

(a) (b)

Figure III.5: **Synthetic chiral symmetric wires engineered with atomic momentum states. a.** Schematic lattice of the nearest-neighbor-coupled chiral symmetric wire. Site-to-site links within the unit cell (solid) and those connecting different unit cells (dashed) have independent tunneling energies m_n and t_n, respectively. **b.** Schematic of the experimental implementation of the tight-binding model depicted in **a**, with tunneling based on two-photon Bragg transitions between discrete atomic momentum states.

matrices. The m_n and t_n characterize the intra- and inter-cell tunneling energies. This model can describe chiral wires of the AIII or BDI symmetry classes, by choosing the intra-cell hopping term to be $S = \sigma_x$ (BDI) or $S = \sigma_y$ (AIII).

In Refs. [48, 49, 50], the Hamiltonian Eq. (III.22) is implemented by using the controlled, parametric coupling of many discrete momentum states of ultracold atoms, see Fig. III.5. A pair of counter-propagating laser fields with nominal wavelength $\lambda = 1064nm$ and wavevector $k = 2\pi/\lambda$ are applied to a weakly-trapped Bose-Einstein condensate (BEC) of ^{87} Rb atoms. Both lasers are far-detuned from any atomic transitions; most of the trapping power is in one of the beams while the other provides only a weak confinement. This arrangement results in a weak harmonic trapping along the propagation axis of the high-power beam (with

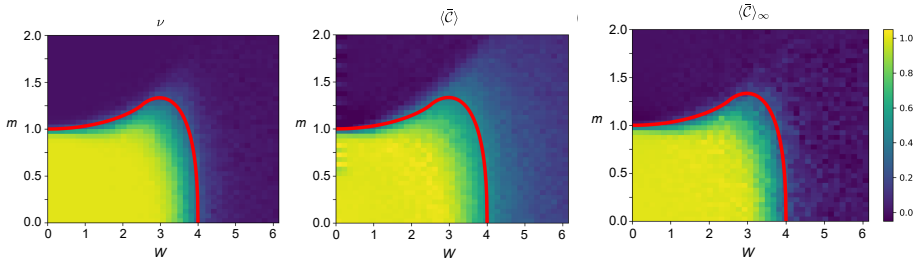

(a) (b) (c)

Figure III.6: **Topological phase diagrams of the BDI model with disorder** $W \equiv W_2 = 2W_1$. All the simulations have been performed for a system of 50 unit cells and averaged over 1000 disorder realizations. **a.** Real space winding number ν. **b.** Disorder- and time-averaged mean chiral displacement $\langle\bar{\mathcal{C}}\rangle$. The temporal sliding average has been done for times $\tau \in [5, 50]$ with $\Delta\tau = 1$. **c.** Disorder-averaged MCD in the long time limit of 1000 tunneling times, $\langle\bar{\mathcal{C}}\rangle_\infty$. The red lines (identical in all panels) indicate the critical phase boundary, where the localization length diverges in the thermodynamic limit according to Ref. [124].

a harmonic trapping frequency of roughly 10 Hz) and tighter trapping (with a harmonic frequency of roughly 130 Hz) along the other two axes. The lattice is created by passing the high-power trapping beam through a series of acousto-optic modulators which turn the single frequency beam into a beam containing many slightly detuned frequency components. This multi-frequency beam is then directed to counter-propagate with itself at the location of the atoms. The spatial periodicity of the laser interference pattern, π/k, defines the set of momentum states separated by integer values of $2\hbar k$. These states may be coupled from the BEC, which is a source of atoms with essentially zero momentum, and they represent the effective sites of the synthetic lattice. The tunneling of atoms between these sites is precisely controlled by simultaneously driving many two-photon Bragg transitions with the applied laser fields. The individual, spectroscopically-resolved, control over many such transitions is al-

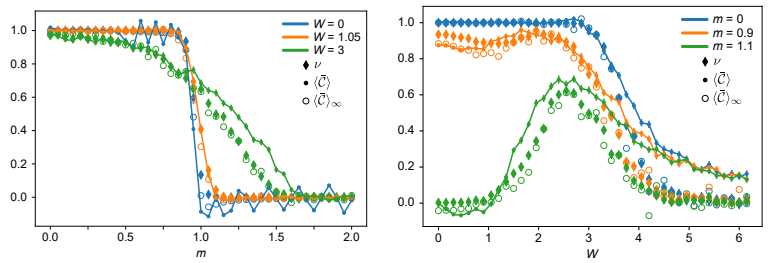

(a) (b)

Figure III.7: **Comparison of the winding number ν and the time- and disorder-averaged MCD $\langle\bar{\mathcal{C}}\rangle$.** Cuts through the phase diagrams in Figs.III.6(a) and III.6(b), comparing the winding number ν (filled diamonds), the time- and disorder-averaged MCD, $\langle\bar{\mathcal{C}}\rangle$ (lines with filled circles), and its infinite time limit $\langle\bar{\mathcal{C}}\rangle_\infty$ (open circles), for a BDI model with disorder ratio $W \equiv W_2 = 2W_1$.

lowed for by the Doppler shifts experienced by the atoms, which are unique to the various Bragg transitions. This provides local (in momentum space) control of the intra- and inter-cell tunneling amplitudes and phases, directly through the amplitudes and phases of the corresponding Bragg laser fields [48].

In particular, the expressions:

$$t_n = t(1 + W_1\omega_n), \tag{III.23}$$
$$m_n = t(m + W_2\omega'_n), \tag{III.24}$$

define the variations of the hopping terms, where t is the characteristic inter-cell tunneling energy, m is the ratio of intra- to inter-cell tunneling in the clean limit, ω_n and ω'_n are independent random real numbers chosen uniformly from the range $[-0.5, 0.5]$, and W_1 and W_2 are the dimensionless disorder strengths applied to inter- and intra-cell tunneling.

The BDI model: detecting a phase transition from topological to trivial

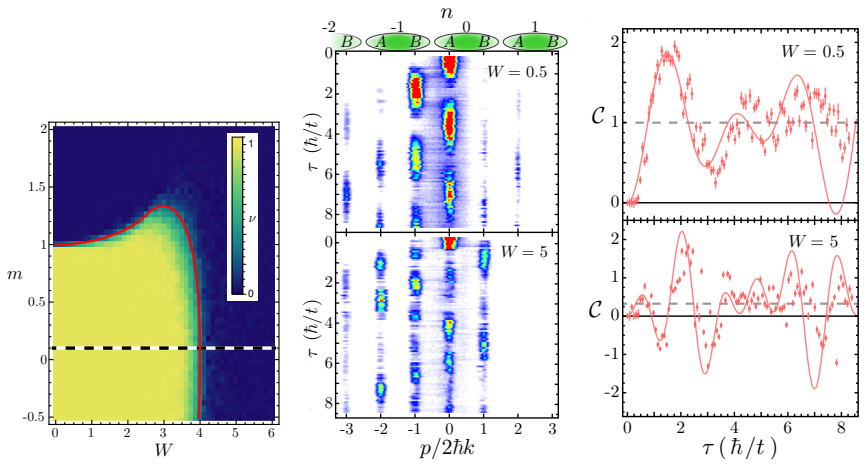

Figure III.8: **Disorder-driven transition from topological to trivial wires**. **a.** Topological phase diagram of a BDI wire of $N = 200$ unit cells. The diagram shows the real space winding number ν (inset color scale) as a function of disorder strength W and tunneling ratio m with tunneling disorder strengths $W \equiv W_2 = 2W_1$. The dashed line at $m = 0.1$ indicates the region explored experimentally. The solid red curve indicates the critical phase boundary predicted for an infinite system in Ref. [124]. **b.** Integrated absorption images of the bulk dynamics following a sudden quench of the tunnel couplings, for both weak disorder ($W = 0.5$) and strong disorder ($W = 5$), each for a single disorder configuration. The data refer to a system of $N = 20$ unit cells. **c.** Dynamics of the MCD, $\mathcal{C}(\tau)$, as calculated from the data shown in **b**. The solid red curves are numerical simulations with no free parameters. The dashed gray horizontal lines denote $\langle \bar{\mathcal{C}} \rangle$ for each data set. The error bars in **c** denote one standard error of the mean.

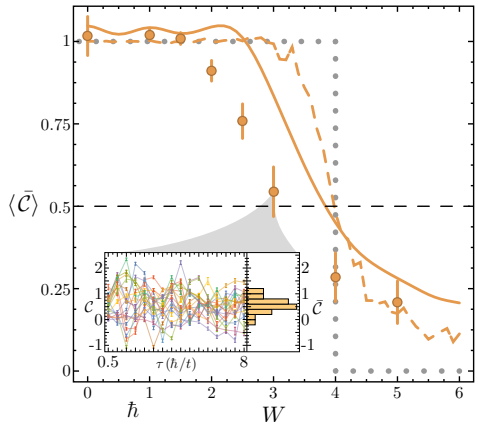

Figure III.9: **Time- and disorder-averaged MCD**. Time- and disorder-averaged MCD, $\langle\bar{\mathcal{C}}\rangle$, as a function of W for $m = 0.1$. The data are averaged over 20 independent disorder configurations and over times τ varying from 0.5 to $8\hbar/t$ in steps of $0.5\hbar/t$. The solid gold line represents a numerical simulation for 200 disorder configurations, but with the same time-average as the data. The dashed gold line represents a numerical simulation for 200 disorder configurations, as the solid one, but sampled to much longer times ($\tau = 1000\hbar/t$) in a wire with 250 unit cells. The dotted grey curve shows the topological index in the thermodynamic limit which takes a value of 0.5 at the critical point, as indicated by the horizontal dashed line. The inset shows $\mathcal{C}(\tau)$ for $W = 3$ as a function of time for all 20 disorder configurations with $\mathcal{C}(\tau)$ for each disorder shown in the histogram. The error bars denote one standard error of the mean.

Let us first consider the influence of disorder added to a strongly dimerized BDI wire (Eq. (III.22) with $S = \sigma_x$) characterized by a small intra- to inter-cell tunneling ratio of $m = 0.1$ (with $t/\hbar \approx 2\pi \times 1.2$ kHz). In the clean limit, this system is in the topological regime. The disorder amplitudes are fixed to $W \equiv W_2 = 2W_1$. Figure III.6(a) shows the disorder-averaged

topological phase diagram of the BDI model as a function of W and m in terms of the real-space winding number (Eq. (III.19)) together with the critical phase boundary predicted for an infinite system in Ref. [124]. We show, through numerical simulations of the BDI system's dynamics in the thermodynamic limit, that the disorder- and time- averaged MCD matches the expected value of the real-space winding number, see Figs. III.6(b), III.6(c) and III.7.

The entire atomic population is initially localized in the central site of the lattice of $N = 20$ unit cells, in particular in the site A of the unit cell $n = 0$, with all the tunneling couplings turned off. Then the tunnel couplings are quenched on in a stepwise fashion. The projection of the localized initial state onto the quenched system's eigenstates leads to a rich dynamics for both weak ($W = 0.5$) and strong ($W = 5$) disorder. Such site-resolved dynamics of the atomic population distribution is directly measured by a series of absorption images taken after a time τ, for 16 values τ evenly spaced between $0.5\hbar/t \approx 65\mu$s and $8\hbar/t \approx 1040\mu$s, and the discrete momentum states are separated according to their momenta during a time-of-flight period [48]. The measure is repeated within 20 different disorder configurations. The MCD and its time- and disorder-average $\langle\bar{\mathcal{C}}\rangle$ are extracted from the data and shown in Fig. III.8. In particular, figure III.9 shows that $\langle\bar{\mathcal{C}}\rangle$ is robust to weak disorder maintaining a nearly-quantized value close to one, while, for strong disorder, $W \gtrsim 2$, we observe a relatively steep drop in $\langle\bar{\mathcal{C}}\rangle$, with it falling below $\langle\bar{\mathcal{C}}\rangle = 0.5$ for $W \gtrsim 3$. This behaviour is associated to a disorder-driven transition from topological ($W \lesssim 4$) to trivial wires ($W \gtrsim 4$). We observe a smooth crossover due to finite-time broadening from the abbreviated period of quench dynamics and the corresponding finite number of sites. However, on an infinitely long chain, we would expect to observe a sharp phase transition in the infinite-time limit of $\langle\bar{\mathcal{C}}\rangle$ measurement, yielding quantized values of the invariant for all disorders, and half-integer values at the critical phase boundary, as shown in Fig. III.3 for a clean system.

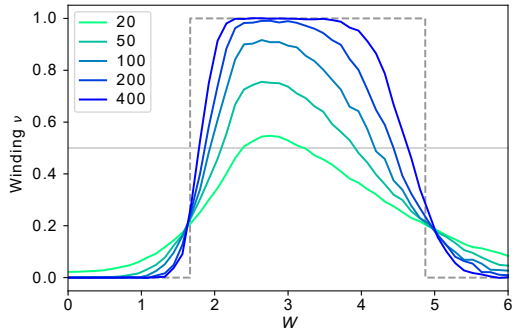

Figure III.10: **Emergence of the TAI plateau.** Winding number ν of the AIII model computed as a function of the disorder strength $W \equiv W_2$, with $W_1 = 0$ and $m = 1.12$, averaged over 1000 disorder realizations. The various lines display results for systems with an increasing number of unit cells N, and the gray dashed line indicates the expected thermodynamic limit, given by the divergence of the localization length, as found in Ref. [124].

The AIII model: observation of the topological Anderson insulator phase

The mechanism for the formation of a TAI phase was first elaborated in Ref. [129] for 2D systems. In that work, the disorder is taken into account perturbatively using the self-consistent Born approximation, and it was shown to effectively renormalize the parameters in the Hamiltonian, including the parameter that tunes between the topological and trivial phases. In a system described by the Hamiltonian (III.22), the TAI phase arises because, as disorder is added to the trivial phase tuned near the clean critical point that is $m = 1$, m is renormalized through a value smaller that one which is into the topological phase. This type of reasoning was adapted and extended to describe the TAI phase in 1D systems including both the BDI- and AIII-class wires that we consider

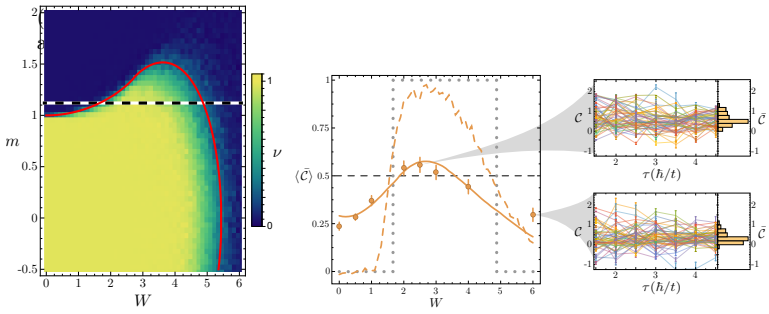

(a) (b)

Figure III.11: **Observation of the topological Anderson insulator phase**. **a.** Topological phase diagram of the AIII wire with $N = 200$ unit cells. The diagram shows the computed winding number (color scale at right) as a function of disorder strength W and tunneling ratio m with tunneling disorder strengths $W \equiv W_2$ ($W_1 = 0$). The striped black and white line at $m = 1.12$ indicates the region explored experimentally. The solid red curve indicates the critical boundary. **b.** $\langle \bar{C} \rangle$ as a function of W for $m = 1.12$. The data refer to a system of $N = 20$ unit cells. The disorder average is taken over 50 independent disorder configurations and the time average over the range 1.5-4.5 $\hbar/t$ with steps of 0.5 $\hbar/t$. The solid gold line refers to a numerical simulation for 200 disorder configurations, but with the same time sampling as the data. The dashed gold line is based on the same simulation as the solid gold line, but sampled to much longer times ($\tau =$ 1,000 $\hbar/t$) in a 250 unit cell system. The dotted grey curve shows the topological index in the thermodynamic limit, which takes a value of 0.5 at the critical points, as indicated by the horizontal dashed line. $\mathcal{C}(\tau)$ as a function of time for for $W = 2.5$ and for $W = 6$ for all 50 disorder realizations. All error bars in **b** denote one standard error of the mean.

here [130, 121, 124]. Numerical simulations show that, in the thermodynamic limit, a random tunneling disorder induces the TAI phase over a broad range of weak to moderate W values, see Fig. III.10. It can also

been shown that a very large disorder generates again a trivial Anderson insulator phase, see Fig. III.11(a). Let us now consider an Hamiltonian belonging to the AIII class (Eq. (III.22) with $S = \sigma_y$), with $m = 1.12$. In the clean limit, the system is in a trivial phase. Since the system is so near the critical point, the band gap in the clean limit is much smaller than in the previous experimental setup. Here differently from the previous case, the disorder is added only to the intra-cell hopping terms, i.e. $W_1 = 0$ and $W \equiv W_2$. From Refs. [129, 130, 121], we expect that, for weak disorder of this form, the intra-cell hopping m should be renormalized toward the topological phase resulting in a TAI. Figure III.11(b) shows the dependence of $\langle \bar{\mathcal{C}} \rangle$ on the disorder strength. The measured $\langle \bar{\mathcal{C}} \rangle$ values are obtained, as in the previous case, through the non-equilibrium bulk dynamics of the atoms following a quench of the tunneling. Due to the different experimental conditions, the explored time-range is narrower than in the previous case, τ goes from 1.5 to $4.5\hbar/t$ with steps of $0.5\hbar/t$. However, the experiment has been repeated within more disorder configurations, 50, to allow for stable measures of $\langle \bar{\mathcal{C}} \rangle$. For weak disorder, $\langle \bar{\mathcal{C}} \rangle$ rises and reaches a pronounced maximum at $W \approx 2.5$. This is consistent with the expected change in the renormalized m parameter for weak disorder. In fact, according to Refs. [129, 130, 121], the lowest-order correction to m has a negative sign. $\langle \bar{\mathcal{C}} \rangle$ then decays for very strong applied disorder. Therefore, the initial increase of $\langle \bar{\mathcal{C}} \rangle$ followed by its decrease is indicative of two phase transitions, from trivial wires to the TAI phase and from the TAI phase to a trivial Anderson insulator.

IV

Topological quantum walks

Quantum walks (QWs) are periodically driven (Floquet) protocols implementable within a large variety of atomic and photonic platforms [131]. QWs have been firstly studied for their importance in matter of quantum computation [132] and searching algorithms [133, 134]. More recently, in 2010, they have been discovered to be a valuable resource in the field of the topological condensed matter physics as they can be regarded as stroboscopic simulators of all the single-particle topological lattice Hamiltonians in 1 and 2D [67]. These systems exhibit extra topologically protected edge states with respect to their static counterparts [46, 76]. The existence of these edge states is not predicted by the topological invariant associated to the system by the standard topological classification [3]. Hence, a new classification dedicated to Floquet topological systems has been built [67, 42, 75, 43, 44, 45]. In the last years, many topological protocols of QW have been implemented in different architectures based on both cold atoms and photons in 1D [68, 69, 70, 66, 71, 72, 73, 74].

In Sec. IV.1, we focus on topological protocols of QW in 1D. In SubSec. IV.1.1, we review the classification of 1D Floquet topological insulators in terms of nonspatial discrete symmetries (PHS, TRS, CS) provided in Refs. [67, 42, 75, 43, 45]. Then, in SubSec. IV.1.2, we introduce briefly the general concept of discrete time quantum walk (DTQW) in 1D, and

in SubSecs. IV.1.3 and IV.1.4 we describe in details two concrete protocols of chiral symmetric DTQW in 1D. The protocol described in SubSec. IV.1.3 has been experimentally implemented within a photonic architecture with twisted light beam [69, 70, 71]. This setup is discussed in details in the next chapter in Sec. V.1. The protocol described in IV.1.4 has been proposed in Ref. [83].

In Sec.IV.2, we focus on topological protocols of DTQW in 2D. In SubSec. IV.2.1, we review the topological classification of these systems provided by Rudner et al. in Ref. [44]. In SubSec. IV.2.2, we apply this analysis to a concrete protocol of topological 2D DTQW which we have implemented with a novel photonic platform where the walker's position is mapped onto the transverse light wavevector [80]. The description of this setup is discussed in details in the next chapter in Sec. V.2

IV.1 Topological discrete time quantum walks in 1D

IV.1.1 Topological classification of 1D Floquet Hamiltonians

Let us consider non-interacting particles evolving on a 1D lattice under a time-dependent Hamiltonian $H(t)$ such that $H(t+T) = H(t)$, where T is the period of the driving cycle. The evolution operator of the system over a full period reads:

$$U(T) = \mathbb{T} e^{-i\int_0^T H(t)dt}, \tag{IV.1}$$

where $\mathbb{T}$ is the time-ordering operator. $U(T)$ is called Floquet operator [42]. If $|\phi\rangle$ is an eigenstate of $U(0)$, then $U(T)|\phi\rangle = e^{i\epsilon T}|\phi\rangle$, and ϵ is called quasi-energy. In the long time limit, the system is a stroboscopic simulator of an effective (Floquet) Hamiltonian:

$$H_{eff} = \frac{i \log U(T)}{T}. \tag{IV.2}$$

It is important to notice two important differences between H_{eff} and a static Hamiltonian: i) the Floquet operator and thus H_{eff} depends on

the choice of the starting time of the period, changing this starting time means applying a unitary operation on $U(T)$ and then changing H_{eff}, in this case, the eigenvalues remain unchanged but the eigenvectors can be different; ii) the eigenvalues of the effective Hamiltonian, called quasi-energies ϵ, are defined up to integer multiples of $2\pi/T$. These differences are crucial in the topological analysis of Floquet systems.

We could be tempted to classify periodically-driven systems possessing a gapped Floquet Hamiltonian, by using the standard topological classification of static topological insulators and superconductos [3]. Namely, by looking for the discrete nonspatial symmetries (TRS, PHS and CS) of their effective Hamiltonians. However two issues appear immediately: i) the symmetries of the effective Hamiltonian depend on the arbitrary choice of the starting time of the driving period or time-frame; ii) if the effective energy spectrum is gapped around $\epsilon = 0$, it is also gapped around $\epsilon = \pm\pi/T$. As a consequence of this, when a 1D periodically-driven system lies in a topological phase and edges are inserted in the system, the topologically protected edge modes can have quasi-energies $\epsilon = 0$ or $\epsilon = \pi/T$ [46, 76]. Hence, in order to have a bulk-edge correspondence for periodically driven systems, one needs two topological indices counting separately the number of edge-modes of the two species.

For these reasons, a new topological classification for 1D periodically driven systems has been defined in the last decade [42, 67, 75, 43]. Within this classification, each topological class in 1D, is associated to a couple of topological invariants recovering the bulk-edge correspondence separately for the 0 and the π/T energy modes.

Particle-hole symmetry

Let us start the analysis of the effective Hamiltonian's symmetries with the partice-hole symmetry. An effective Hamiltonian is particle-hole symmetric if it satisfies Eq. (II.5) with $\mathcal{P} = PK$ and $\mathcal{P}^2 = \pm 1$, where P is a unitary operator and K is the complex conjugation. The associated Floquet operator will satisfy:

$$PU(T)^* P^\dagger = U(T). \tag{IV.3}$$

If this condition is satisfied within a choice of the time-frame, it is satisfied within all the others by the same particle-hole operator [42, 135]. In particular, if there exists a basis where all the elements of $U(T)$ are real numbers, then $\mathcal{P} = k$ [42]. The quasi-energy spectrum of a PHS effective Hamiltonian is gapped around $\epsilon = 0$ and $\epsilon = \pm\pi/T$. For 1D translational invariant PHS systems, the $\mathbb{Z}_2$ invariant associated to the D class in the standard topological classification [3] is replaced by a couple of $\mathbb{Z}$ invariants, (Q_0, Q_π). They are respectively the total number of times the curves described by the eigenvalues of the Bloch unitary evolution operators $U_{k=0}(t)$ and $U_{k=\pi}(t)$ in the complex plane for t going from 0 to T, cross the value 1. Q_0 and Q_π count correctly the number of topologically protected modes with energy 0 and π/T arising at the edges of a cut periodically-driven PHS chain [46].

Chiral symmetry

For the chiral symmetry the analysis is more complex. In Refs. [75, 43], the authors provide an operative definition of chiral symmetry in a 1D Floquet system. Such a system is chiral-symmetric if there exists a time $t_1 \in]0, T[$ such that $U_1(T) = \Gamma F^\dagger \Gamma F$ with Γ hermitian and unitary and the operator F defined as

$$F = \mathbb{T} e^{-i\int_0^{t_1} H(t)dt}. \tag{IV.4}$$

These conditions imply that the effective Hamiltonians associated with $U_1(T)$ and with $U_2(T) = F\Gamma F^\dagger \Gamma$ anticommute with Γ. The couple of $\mathbb{Z}$ invariants which provide the bulk-edge correspondence for 1D chiral Floquet systems, $(\mathcal{W}_0, \mathcal{W}_\pi)$ is defined as:

$$\begin{aligned} \mathcal{W}_0 &= \frac{\mathcal{W}_1 + \mathcal{W}_2}{2} \\ \mathcal{W}_\pi &= \frac{\mathcal{W}_1 - \mathcal{W}_2}{2}, \end{aligned} \tag{IV.5}$$

where $\mathcal{W}_1$ and $\mathcal{W}_2$ are the winding numbers of the effective Hamiltonians $H_1 = \frac{i \log U_1(T)}{T}$ and $H_2 = \frac{i \log U_2(T)}{T}$ which can be computed equivalently

from Eqs. (II.7), (II.10), (II.11). In Ref. [43], the authors derive another equivalent definition of $\mathcal{W}_0$ and $\mathcal{W}_\pi$ in terms of the blocks of the matrix F written in quasi-momentum space in the canonical basis (the eigenbasis of Γ). If

$$F = \begin{pmatrix} a(k) & b(k) \\ c(k) & d(k) \end{pmatrix}, \tag{IV.6}$$

then

$$\begin{aligned} \mathcal{W}_0 &= \oint \frac{\mathrm{d}k}{2\pi i} \partial_k \log[\mathrm{Det}(b(k))] \\ \mathcal{W}_\pi &= \oint \frac{\mathrm{d}k}{2\pi i} \partial_k \log[\mathrm{Det}(d(k))]. \end{aligned} \tag{IV.7}$$

Time reversal symmetry

Finally, as mentioned in SubSec. II.1.1, if an Hamiltonian possesses two of the three discrete symmetries entering the topological classification, it possesses also the third one which can be obtained as product of the others. Therefore, if an effective Hamiltonian is particle-hole and chiral-symmetric, it is also time-reversal-symmetric. Namely, it satisfies Eq. II.4 with $\mathcal{T} = \Gamma\mathcal{P} \equiv \tau K$ and $\mathcal{T}^2 = \pm 1$, where τ is a unitary operator and K is the complex conjugation. The associated Floquet operator will satisfy:

$$\mathcal{T} U(T)^* \mathcal{T}^\dagger = U(T)^\dagger. \tag{IV.8}$$

As proven in Ref. [42], to satisfy this equivalence, a sufficient, but not necessary condition, is the existence of a time t_0 such that:

$$\mathcal{T} H(t + t_0)^* \mathcal{T}^\dagger = H(-t + t_0). \tag{IV.9}$$

IV.1.2 1D discrete time quantum walks

A 1D discrete time quantum walk is a unitary protocol acting on a single quantum observable, the walker, and on its internal degree of freedom,

the coin [56]; the walker moves on an infinite 1D lattice. A unitary operator U acts N times on the system $|walker\rangle \otimes |coin\rangle$. Hence, U is regarded as a Floquet operator $U(T)$ with $T = 1$ and N as the total number of steps of walk. The total QW is given by the operator:

$$\mathcal{U} \equiv U^N = e^{-iNH_{eff}}, \tag{IV.10}$$

where H_{eff} is the effective Hamiltonian of the QW.

In the standard DTQW [56], the Hilbert space of the coin has dimension 2 and the unitary evolution operator is of the kind $U = RT$, where R is a rotation acting in the coin space, and T is a coin-dependent translation of the walker position. A standard choice is $T = \sum_x [|x+1\rangle\langle x| \otimes |+\rangle\langle +| + |x-1\rangle\langle x| \otimes |-\rangle\langle -|]$, where $\{|+\rangle, |-\rangle\}$ is a basis of the coin space.

Let us consider the standard DTQW and let us set the lattice spacing equal to one. For every value of k in the Brillouin zone $[-\pi, \pi]$, the Bloch effective Hamiltonian reads:

$$H_{eff}(k) = \epsilon(k)\mathbf{n}(k) \cdot \sigma, \tag{IV.11}$$

with $\sigma = \{\sigma_x, \sigma_y, \sigma_z\}$ and $\mathbf{n}(k) = \{n_x(k), n_y(k), n_z(k)\}$ being a unitary vector.

A state fully localized on the m-th cell of the lattice reads:

$$|\overline{\Psi}\rangle = \oint \frac{\mathrm{d}k}{\sqrt{2\pi}} e^{ikm} |k\rangle \otimes |s\rangle \equiv \oint \mathrm{d}k |\Psi\rangle, \tag{IV.12}$$

where $\oint \mathrm{d}k$ is the integral over the quasi-momentum Brillouin zone, $|\Psi\rangle \equiv \frac{e^{ikm}}{\sqrt{2\pi}}|k\rangle \otimes |s\rangle$ and $|s\rangle = c_+|+\rangle + c_-|-\rangle$, with $c_\pm$ complex coefficients such that $|c_+|^2 + |c_-|^2 = 1$. For a walker starting in such a state, after N steps in the DTQW, we have:

$$\frac{\langle \hat{m} \rangle_{\overline{\Psi}}}{N} = \oint \frac{\mathrm{d}k}{2\pi} \langle \Psi | e^{iNH_{eff}} (i\partial_k) e^{-iNH_{eff}} | \Psi \rangle = \oint \frac{\mathrm{d}k}{2\pi} \frac{d\epsilon}{dk} \langle s | \mathbf{n} \cdot \sigma | s \rangle + \mathcal{O}(1/N), \tag{IV.13}$$

where, for simplicity, we chose as starting site the 0-th cell and we omitted the explicit dependence on k. Equation (IV.13) clearly shows that, despite from the fact that the quantum walk was firstly proposed in Ref. [56] as a quantum analogue of the classical random walk, the two protocols are dramatically different. Indeed, the propagation of a particle performing a random walk is diffusive, namely $\langle x^2 \rangle \propto N$, with N number of steps, while the propagation of particle performing a quantum walk is ballistic, namely $\langle x^2 \rangle \propto N^2$. Interestingly, by adding decoherence to the 1D DTQW, one can progressively retrieve the classical random walk's diffusive distribution, and by adding a strong static disorder one can induce Anderson localization [60].

Discrete time 1D quantum walks have been realized in many experimental platforms with both trapped ultra-cold atoms and photons, see Refs. [60, 59, 131] and references therein.

IV.1.3 Chiral symmetric discrete time quantum walks

The first topological protocol of 1D DTQW has been proposed by Kitagawa et al. in 2010 in Ref. [67] and implemented experimentally two years later, within a photonic architecture [76]. It was called *split-step QW* as the standard translation operator T was split in two parts (two translations in opposite directions) by a rotation operator. The split-step QW possesses PHS and CS in the sense of the topological classification of Floquet systems reviewed in SubSec. IV.1.1. Thus, its bulk-edge correspondence is provided by the couple of topological indices $(\mathcal{W}_0, \mathcal{W}_\pi)$. However, when this protocol was experimentally implemented for the first time in Ref. [76], the topological classification of the Floquet system was still incomplete; then, the observation of a couple of edge states, whose existence was not predicted by the static system's winding number, is reported as a novel phenomenon to be further studied.

Here, we present a protocol of chiral DTQW, belonging to the same topological class of the split-step QW. We implemented this protocol for the first time in Ref. [70], within a photonic architecture with twisted light beams which we will describe in details in the next chapter in Sec. V.1. In

this first work, we detected a topological phase transition by looking at the even moments of the probability distribution of the walker final positions. One year later, in Ref. [71], we provided a complete experimental characterization of this protocol by measuring $\mathcal{W}_0$ and $\mathcal{W}_\pi$ through the walker mean chiral displacement.

The building blocks of the protocol are:

$$W = \sum_m c_m^\dagger(\sigma_0 - i\sigma_x)c_m, \tag{IV.14}$$
$$Q = \sum_m \cos\frac{\delta}{2}c_m^\dagger c_m + i\sin\frac{\delta}{2}\left(c_{m+1}^\dagger\frac{(\sigma_x - i\sigma_y)}{2}c_m + h.c.\right),$$

with $c_m^\dagger = (c_{m,+}^\dagger, c_{m,-}^\dagger)$. The corresponding Bloch operators for each value of k in the B.Z. read:

$$W = e^{-i\frac{\pi}{4}\sigma_x} = \frac{1}{\sqrt{2}}\begin{pmatrix} 1 & -i \\ -i & 1 \end{pmatrix} \tag{IV.15}$$
$$Q = e^{i\frac{\delta}{2}(\cos(k)\sigma_x + \sin(k)\sigma_y)} = \begin{pmatrix} \cos(\delta/2) & ie^{-ik}\sin(\delta/2) \\ ie^{ik}\sin(\delta/2) & \cos(\delta/2) \end{pmatrix}.$$

As we will discuss in further details in the next chapter, in the photonic implementation of this protocol, the operators W and Q correspond to two unitary optical devices acting on the light polarization and OAM. The default Floquet operator is $U \equiv U(T) = QW$. The effective Hamiltonian is $H_{eff} = i\log U$, $(T = 1)$. In quasi-momentum space H_{eff} is given by $H_{eff} = \epsilon(k)\mathbf{n}(k)\cdot\sigma$ with

$$\epsilon(k) = -\cos^{-1}\left(\frac{\cos(\delta/2) + \sin(\delta/2)\cos(k)}{\sqrt{2}}\right). \tag{IV.16}$$

and

$$n(k) = \frac{1}{c}\begin{pmatrix} -\cos(\delta/2) + \sin(\delta/2)\cos(k) \\ \sin(\delta/2)\sin(k) \\ -\sin(\delta/2)\sin(k) \end{pmatrix} \tag{IV.17}$$

where $c = \sqrt{2-2\cos^2(E)} = \sqrt{2}|\sin(E)|$. The spectrum has vanishing gaps (or band-touchings) at $E = 0$ for $\delta = \{\frac{\pi}{2}, \frac{7\pi}{2}\}$, and at $E = \pm\pi$ for $\delta = \{\frac{3\pi}{2}, \frac{5\pi}{2}\}$.

The system is particle-hole symmetric; the particle-hole operator in quasi-momentum space reads $\mathcal{P} = K\sigma_z$. It is straightforward to see that $\mathcal{P}$ anticommutes with $H_{eff}(k)$ for every k. As mentioned in SubSec. IV.1.1, $\mathcal{P}$ will anticommute also with the effective Hamiltonians corresponding to the other possible choices of the QW time-frame [42, 135].

For the chiral symmetry, we should find an operator F which fulfils Eq. (IV.4). We find $F = \sqrt{Q}\sqrt{W}$, with $\Gamma = \sigma_z$. In perfect agreement with Refs. [75, 43], we find that $U_1 = \sqrt{W}Q\sqrt{W}$ and $U_2 = \sqrt{Q}W\sqrt{Q}$ have effective Hamiltonians which anticommutes with Γ. We can compute the invariants $(\mathcal{W}_0, \mathcal{W}_\pi)$ using Eq. (IV.5) starting from the winding numbers $\mathcal{W}_1$ and $\mathcal{W}_2$ of the effective Hamiltonians $H_1 = i\log U_1$ and $H_2 = i\log U_2$. These invariants provide the correct bulk-edge correspondence for the system once this is cut.

The fact that $(\mathcal{W}_0, \mathcal{W}_\pi)$ can be obtained from the winding numbers $\mathcal{W}_1$ and $\mathcal{W}_2$ makes possible to measure them using the mean chiral displacements of the walker, as we proved in SubSec. III.1.1. In the long time limit, namely for the number of QW steps $N \to \infty$, the mean chiral displacement $\mathcal{C}_1(N)$ ($\mathcal{C}_2(N)$) of the walker starting localized in the 0-th cell and evolving under U_1 (U_2) will give $\mathcal{W}_1$ ($\mathcal{W}_2$), see Eq. (III.12). Hence, we obtain the complete topological characterization of the system in terms of the long time limit of the observables $\mathcal{C}_0(t) \equiv (\mathcal{C}_1(t) + \mathcal{C}_2(t))/2$ and $\mathcal{C}_\pi(t) \equiv (\mathcal{C}_1(t) - \mathcal{C}_2(t))/2$. In the next chapter, we show the results of the measurement of $\mathcal{C}_0$ and $\mathcal{C}_\pi$ for our QW [71].

IV.1.4 Periodically driven SSH$_4$ model

Here we consider a periodically-driven version of the SSH$_4$ model presented in SubSec. III.1.2, where even and odd tunnelings are turned on and off in a periodic sequence. More specifically, a single period of the evolution is generated by the one-step operator U given by a composition of two unitary operators obtained extending W and Q to a coin-space of

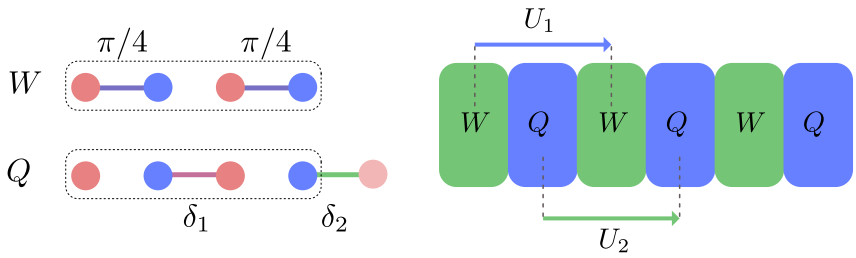

Figure IV.1: **The driven SSH$_4$ model. a.** Scheme of the unit step of the driven SSH$_4$ model, or quantum-walk with four dimensional coin. The figure is taken from Ref. [83]. The four sites of each unit cell correspond to the coin states $|A_1\rangle, |A_2\rangle$ (red spots), and $|B_1\rangle, |B_2\rangle$(blue spots). The dynamics is obtained by the repeated application of two unitary operators: W is a rotation acting on the odd sites of the lattice (which are all intra-cell), while Q acts on the even sites, thereby coupling different cells. **b.** Scheme of the quantum-walk protocol. In a periodically driven system, the choice of the initial instant of the time period, i.e. the time-frame, is arbitrary. The single-step unitary operators U_1 and U_2 are explicitly chiral symmetric in the sense of the topological classification of Floquet systems [75, 43].

dimension 4. The extended operator W reads:

$$W = e^{-i\frac{\pi}{4}S_{0x}} \tag{IV.18}$$

where $S_{0x} = \sigma_0 \otimes \sigma_x = \mathbb{I} \otimes \sigma_x$. As shown in Fig. IV.1, the operator W acts within each unit cell of the effective lattice (see Fig. IV.1(a)). On the other hand, the extended operator Q acts both within a given cell, and between

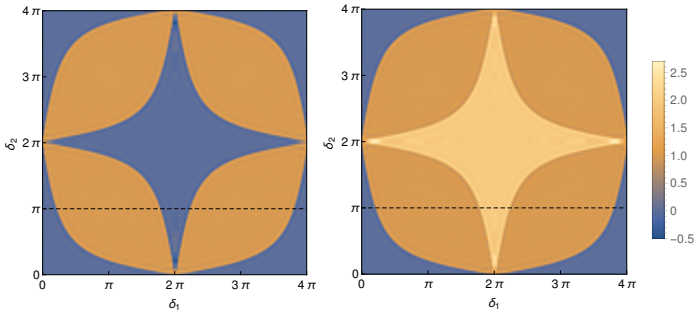

(a) (b)

Figure IV.2: **Mean chiral displacement of the driven SSH$_4$ model.** Temporal average of the MCD, obtained performing a sliding average between the 30$^{\text{th}}$ and the 50$^{\text{th}}$ step of the numerically simulated walker's evolution, as a function of the parameters δ_1 and δ_2 parametrizing the action of the Q operators, for the time-frames U_1 (**a**) and U_2 (**b**). The figure is readapted from Ref. [83]

two consecutive cells. It reads:

$$
\begin{aligned}
Q\cdot(|A_1\rangle\otimes|m\rangle) &= \cos\frac{\delta_2}{2}|A_1\rangle\otimes|m\rangle - i\sin\frac{\delta_2}{2}|B_2\rangle\otimes|m-1\rangle \qquad \text{(IV.19)}\\
Q\cdot(|B_1\rangle\otimes|m\rangle) &= \left(\cos\frac{\delta_1}{2}|B_1\rangle - i\sin\frac{\delta_1}{2}|A_2\rangle\right)\otimes|m\rangle\\
Q\cdot(|A_2\rangle\otimes|m\rangle) &= \left(\cos\frac{\delta_1}{2}|A_2\rangle - i\sin\frac{\delta_1}{2}|B_1\rangle\right)\otimes|m\rangle\\
Q\cdot(|B_2\rangle\otimes|m\rangle) &= \cos\frac{\delta_2}{2}|B_2\rangle\otimes|m\rangle - i\sin\frac{\delta_2}{2}|A_1\rangle\otimes|m+1\rangle.
\end{aligned}
$$

In order to characterize the topology of this driven model we have still to consider the two explicitly chiral inversion-symmetric time-frames defined by the evolution operators $U_1 = \sqrt{W}Q\sqrt{W}$ and $U_2 = \sqrt{Q}W\sqrt{Q}$, where now W and Q are given by Eq. (IV.18) and (IV.19), see Fig. IV.1(b).

Figure IV.3(a) depicts the temporal average of $\mathcal{C}_1(t)$ and $\mathcal{C}_2(t)$ obtained performing a sliding average between the 30^{th} and the 50^{th} step of a numerical simulation of the walker's evolution. To illustrate the bulk-boundary correspondence for this model, in Fig. IV.3(b), we show the energy spectrum and the degree of localization of eigenstates in a chain with open boundary conditions. Comparing the two panels, it may be seen that the invariants C_0 and C_π converge, respectively, to the number of edge states with energy equal to 0 and to π. Finally, figure IV.3(b) also shows the presence of edge states with energy $\pi/2$. These states are not protected by the chiral symmetry, and therefore not robust against (chiral-preserving) disorder. In order to illustrate this fact, we add a spatial disorder in the operator W: the hoppings of the Hamiltonian of W are multiplied by a factor $(1+\epsilon)$, where ϵ is a random number in the range $[-\Delta/2, \Delta/2]$. The right side of the energy spectrum (after the dashed line) in Fig. IV.3(b) shows clearly that, when disorder is applied, the unprotected states change of energy, whereas the 0 and the $\pi-$energy states remain unaffected.

For the chiral symmetric DTQW with coin having dimension two, we verified that the observables $\mathcal{C}_0$ and $\mathcal{C}_\pi$ are robust topological marker by observing that, in presence of chiral-preserving dynamical disorder of amplitude small compared to the gap, the ensemble average of the mean chiral displacement smoothly converges to the value obtained for a clean system. At a qualitative level, systems with internal dimension $\mathcal{D} > 2$ in presence of disorder behave analogously to systems with $\mathcal{D} = 2$.

The driven SSH_4 may be implemented in a photonic setting using a lattice of evanescently coupled optical wave-guides. In these devices, the different hopping amplitudes correspond to different distances between the wave-guides [86, 136, 137, 61]. The periodic driving could be achieved by periodical modulation of the separation between the wave-guides along the propagation direction [136, 61].

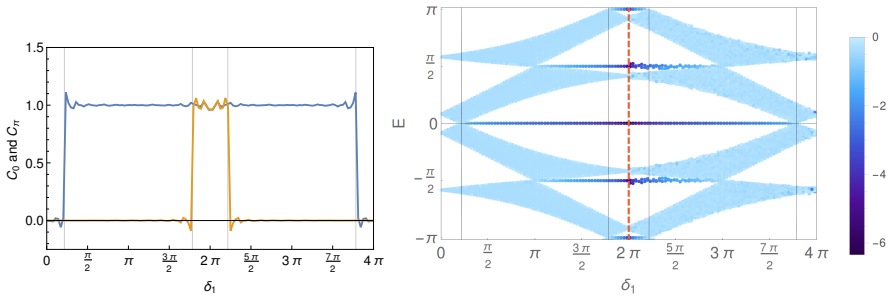

(a) (b)

Figure IV.3: **Bulk-edge correspondence for the driven SSH$_4$. a.** Time average of the mean chiral displacements $\mathcal{C}_0(t) \equiv \frac{\mathcal{C}_1(t)+\mathcal{C}_2(t)}{2}$ (blue line) and $\mathcal{C}_\pi(t) \equiv \frac{\mathcal{C}_1(t)-\mathcal{C}_2(t)}{2}$ (yellow line). The points are obtained performing a sliding average between the 30$^{\text{th}}$ and the 50$^{\text{th}}$ step of the numerically simulated walker's evolution. **b.** Quasi-energy spectrum of the effective QW Hamiltonian within open boundary conditions for a chain of $2N+1 = 21$ cells varying δ_1 at fixed $\delta_2 = \pi$. The color coding of the spectrum indicates the degree of localization $log_{10}(1-|\langle\hat{m}\rangle)|/N)$ of each eigenstate on the two edges $m=-N$, $m=N$; light (dark) colors indicate bulk (edge) states. For $\delta_1 > 2\pi$, we have added weak chiral-preserving disorder (see text for details) with $\Delta = 0.6$, showing explicitly that the edge states with $E = \pm\pi/2$ are localized, but not topologically protected. Comparing the left and right image, it is easy to see that C_0 and C_π predict respectively the number of edge states with 0- and $\pi-$energies. The figure is readapted from Ref. [83].

IV.2 Topological discrete time quantum walks in 2D

IV.2.1 Topological classification of 2D Floquet Hamiltonians

Let us consider a non-interacting periodically driven system on a 2D lattice whose effective Hamiltonian (IV.2) belongs to the class of the Chern insulators according to the classification of static topological insulators. The topological invariant associated to this class is the Chern number defined in Eq. II.26. As discussed in SubSec. II.2.4, the total Chern number below an energy gap counts the number of edge states with the same chirality (living on the same edge) crossing the gap during one cycle of the adiabatic pumping. This is equivalent to say that the Chern number of each band equals the difference between the number of edge modes with the same chirality exiting and entering the band during the pumping cycle. The quasi-energy spectrum of a Floquet Hamiltonian is periodic, therefore a mode could for example exit from the upper band from above and enter the lower band from below. In Ref. [44], it is shown that, for this reason, in a Floquet system, one can have chiral edge modes despite the fact that all the Chern numbers are null. Hence, the authors find a new invariant, $W[U_\epsilon]$, which counts the number of edge states at quasi energy ϵ living on the same edge. Then the total Chern number of all the bands between two energy values ϵ and ϵ' reads $\mathcal{V}_{\epsilon,\epsilon'} = W[U_\epsilon] - W[U_{\epsilon'}]$. In order to define $W[U_\epsilon]$ Rudner et al. start from the case of a unitary evolution operator U whose Floquet operator $U(T)$ is the identity. The quasi-energy spectrum of the Floquet Hamiltonian is thus made of a single value $\epsilon = 0$. Since they are considering a translation invariant system of N cells with periodic boundary conditions, they can write the Bloch unitary operator $U(k_x, k_y, t)$ for each value of (k_x, k_y, t) in $[-\pi, \pi] \times [-\pi, \pi] \times [0, 1]$ (the lattice spacings and the time period are set to 1). Hence, U defines a map from a 3D torus to the space of the unitary matrices of dimensions $N \times N$. The index theorem [138], states that U can be associated to an integer

winding number:

$$W[U] = \frac{1}{8\pi^2}\int_0^1\int_{-\pi}^{\pi}\int_{-\pi}^{\pi} \mathrm{d}k_x \mathrm{d}k_y \mathrm{d}t \mathrm{Tr}\left(U^{-1}\partial_t U\left[U^{-1}\partial_{k_x}U, U^{-1}\partial_{k_y}U\right]\right), \tag{IV.20}$$

Rudner et al. demonstrate analytically that, in this trivial case, $W[U]$ equals the number of edge states [44]. Then they consider a generic unitary evolution operator U, with $U(T) \neq \mathbb{I}$ and with a gapped quasi-energy spectrum of the Floquet Hamiltonian. In order to obtain the number of edge states with quasi-energy equal to a certain value ϵ inside the gap ($n_{edge}(\epsilon)$) they continuously deform U into an operator U_ϵ, such that $U_\epsilon(T) = \mathbb{I}$. Then $n_{edge}(\epsilon) = W[U_\epsilon]$ where $W[U_\epsilon]$ is computed using Eq. IV.20.

The interpolation between U and U_ϵ is achieved by a family of unitary U_s parametrized by $s \in [0,1]$, such that $U_{s=0}(t) = U(t)$ and $U_{s=1}(t) = U_\epsilon(t)$. The Floquet operator $U_s(T)$ for every s has to keep a gapped quasi-energy spectrum whose centre moves from ϵ, for $s = 0$, to π, for $s = 1$. Rudner et al. provide also one simple way, among the many possible, to associate an operator U_ϵ to U.

$$U_\epsilon(t,\mathbf{k}) = \begin{cases} U(2t,\mathbf{k}) = e^{-2i\int_0^t H(2\tau,\mathbf{k})d\tau} & 0 \leq t \leq T/2 \\ V_\epsilon(t,\mathbf{k}) = e^{-iH^\epsilon_{eff}(T-2t)}U(T,\mathbf{k}) & T/2 \leq t \leq T, \end{cases} \tag{IV.21}$$

with

$$\hat{H}^\epsilon_{eff} = i\log(\hat{U}e^{-i\epsilon}) - \epsilon. \tag{IV.22}$$

Then, the method proposed by Rudner et al. consists in shrinking the evolution operator $U(t)$ over half of its original period and using the other half to connect it to the identity through a *trivial return map* V_ϵ. They apply this method to a concrete 2D DTQW protocol and they compute $W[U_{\epsilon=0}]$ and $W[U_{\epsilon=\pi}]$. They show that these invariants count correctly the edge states arising in the quasi-energy spectrum of the QW, when edges are introduced in one of the two directions.

IV.2.2 Full topological characterization of a protocol of 2D quantum walk

Here we apply the method presented by Rudner et al. in Ref. [44] to the 2D QW protocol that we proposed and experimentally implemented with a photonic platform [80]. In this setup the walker's coordinates on the 2D lattice are mapped onto the transverse components of the light wavevector, and the unitary operators which consitute the building blocks of the protocol are implemented with polarization dependent diffraction gratings. Further details on the experimental implementation are discussed in Sec. V.2 of the next chapter. This protocol belongs to the same topological class of the ones presented in Ref. [44] and in Ref. [42].

The building blocks of the protocol are the same operators W and Q which constitute the 1D DTQW (Eqs. (IV.14)). However, now, the unitary evolution operator of one step contains two operators, Q_x and Q_y, which shift the walker's position in two perpendicular directions x and y, and the phase in the W operator has opposite sign. In the momentum space they read:

$$W = e^{i\frac{\pi}{4}\sigma_x} = \frac{1}{\sqrt{2}}\begin{pmatrix} 1 & i \\ i & 1 \end{pmatrix} \tag{IV.23}$$

$$Q_x(k_x) = e^{i\frac{\delta}{2}(\cos(k_x)\sigma_x+\sin(k_x)\sigma_y)} = \begin{pmatrix} \cos(\delta/2) & ie^{-ik_x}\sin(\delta/2) \\ ie^{ik_x}\sin(\delta/2) & \cos(\delta/2) \end{pmatrix}$$

$$Q_y(k_y) = e^{i\frac{\delta}{2}(\cos(k_y)\sigma_x+\sin(k_y)\sigma_y)} = \begin{pmatrix} \cos(\delta/2) & ie^{-ik_y}\sin(\delta/2) \\ ie^{ik_y}\sin(\delta/2) & \cos(\delta/2) \end{pmatrix}$$

The Floquet operator of the QW reads:

$$U \equiv U(T) = Q_y Q_x W, \tag{IV.24}$$

with $T = 1$. The quasi-energy spectrum of the associated Floquet Hamiltonian is gapped around $\epsilon = 0$ and $\epsilon = \pm\pi$. We consider the QW step T divided in three parts of the same duration $(1/3)$ and we consider the operators W, Q_x and Q_y in Eq. (IV.23) as the Floquet operators of three time-dependent operators $W(t)$, $Q_x(t)$ and $Q_y(t)$, with $W \equiv W(1/3)$,

$Q_x \equiv Q_x(2/3)$ and $Q_y \equiv Q_y(1)$. The unitary evolution operator $U(t,\mathbf{k})$, for each $\mathbf{k} = (k_x, k_y)$ in the Brillouin torus, reads:

$$\begin{cases} W(t) = e^{i\frac{3\pi}{4}t\sigma_x} & 0 \le t \le 1/3 \\ Q(t,k_x)W = e^{i\frac{3\delta}{2}(t-1/3)[\cos(k_x)\sigma_x + \sin(k_x)\sigma_y]}W & 1/3 \le t \le 2/3 \\ Q(t,k_y)Q(k_x)W = e^{i\frac{3\delta}{2}(t-2/3)[\cos(k_y)\sigma_x + \sin(k_y)\sigma_y]}Q(k_x)W & 2/3 \le t \le 1 \end{cases} \tag{IV.25}$$

Now we build the operator $U_\epsilon(t)$ associated to $U(t)$ using the method proposed by Rudner, Eq. (IV.21), and we compute the windings of $U_{\epsilon=0}$ and $U_{\epsilon=\pi}$ using Eq. (IV.20), as

$$W[U_{0(\pi)}] = W[U] + \int_{1/2}^{1} \mathrm{d}\frac{dt}{8\pi^2} \int_{-\pi}^{\pi}\int_{-\pi}^{\pi} \mathrm{d}k_x \mathrm{d}k_y \mathrm{Tr}\left(V_{0(\pi)}^{-1}\partial_t V_{0(\pi)}\left[V_{0(\pi)}^{-1}\partial_{k_x}V_{0(\pi)}, V_{0(\pi)}^{-1}\partial_{k_y}V_{0(\pi)}\right]\right) \tag{IV.26}$$

In order to compute the winding of V_0 and V_π over the second half of the period $[1/2, 1]$, we use the relation derived in the Appendix of Ref. [44]:

$$\begin{aligned} &\frac{1}{8\pi^2}\mathrm{Tr}\left(A(t,\mathbf{k})^{-1}\partial_t A(t,\mathbf{k}) \cdot \left[A(t,\mathbf{k})^{-1}\partial_{k_x}A(t,\mathbf{k}), A(t,\mathbf{k})^{-1}\partial_{k_y}A(t,\mathbf{k})\right]\right) \\ &\qquad = -\frac{1}{2\pi^2}\partial_t\epsilon(t,\mathbf{k})\sin^2(\epsilon(\mathbf{k},t))\mathbf{n}(\mathbf{k}) \cdot \left(\partial_{k_x}\mathbf{n}(\mathbf{k}) \times \partial_{k_y}\mathbf{n}(\mathbf{k})\right), \end{aligned} \tag{IV.27}$$

with

$$A(t,\mathbf{k}) = e^{-i\epsilon(\mathbf{k},t)\mathbf{n}(\mathbf{k})\cdot\sigma}. \tag{IV.28}$$

Figure IV.4(a) shows the values of W_0, W_π and $\mathcal{V} = W_\pi - W_0$ that we computed for our 2D DTQW changing the parameter δ in Q_x and Q_y simultaneously. Figures IV.4(b)-IV.4(d) show the quasi-energy spectrum of the QW Floquet Hamiltonian evaluated on an infinite stripe along y (open boundary conditions on x) changing k_y, with δ corresponding to three different topological sectors. The comparison with Fig. IV.4(a) shows that the new invariants count correctly the number of states for each edge crossing the quasi-energy gap during the pumping (red and dark blue dots in Figs. IV.4(c) and IV.4(d)).

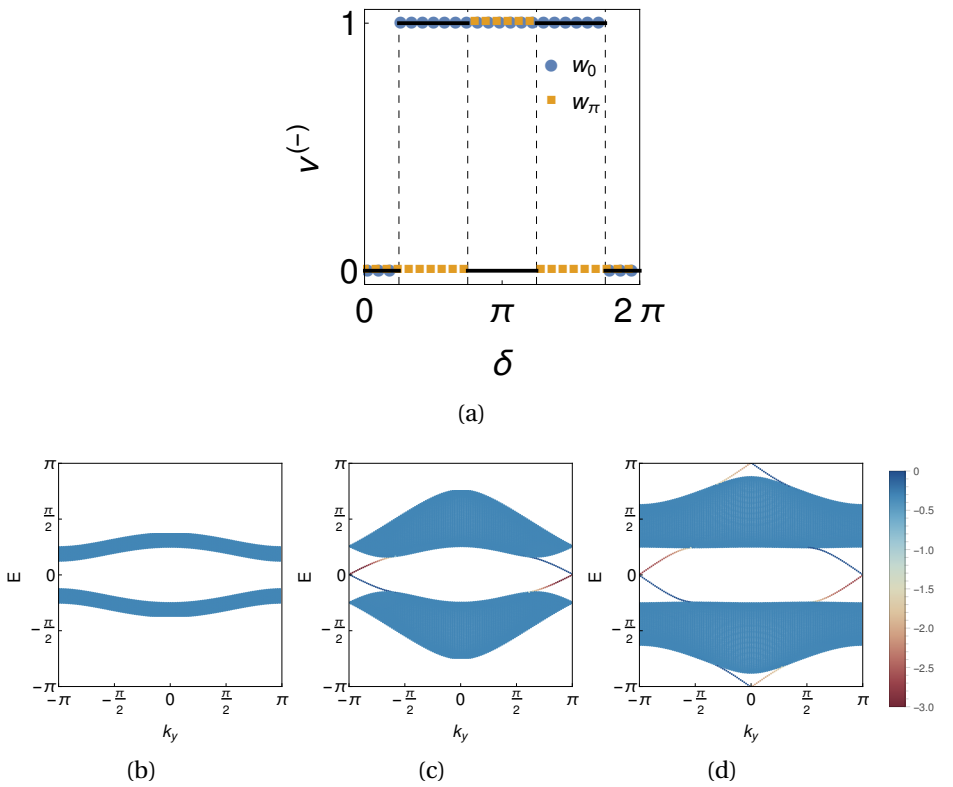

Figure IV.4: **Bulk-edge correspondence for the 2D DTQW. a.** Expected values of the lower band's Chern number ν, $W_\pi \equiv W[U_\pi]$ and $W_0 \equiv W[U_0]$ changing the parameter δ. **b, c, d.** Quasi-energy spectrum of the QW effective Hamiltonian on an infinite strip along y (with $2N+1 = 201$ sites along x) for $\delta = \pi/8$ (**b**), $\delta = \pi/2$ (**c**), $\delta = \frac{7\pi}{8}$ (**d**). The color coding of the spectrum indicates the degree of localization on the two edges $x = -N$ (dark blue) and $x = N$ (red). As degree of localization of each state ψ we take the function $log_{10}(1 - \langle \hat{x} \rangle_\psi)/N)$. The invariants W_0 and W_π predict the correct number of edge states crossing respectively the 0 and the π quasi-energy gaps.

V

Topological photonic quantum walks in one and two dimensions

In this chapter, we present two photonic experiments in which we realized and characterized two topological QWs, respectively, in 1- and 2D; their unitary protocols have been introduced in SubSec. IV.1.3 and SubSec. IV.2.2. Section V.1 is dedicated to the experiment reported in Ref. [71] where we realized a 1D chiral-symmetric QW and measure its topological invariants. Section V.2, is dedicated to the 2D QW simulation experiment reported in Ref. [80] where we realized a Floquet Chern insulator undergoing a constant electric field and we measure its Chern number.

V.1 1D quantum walk of twisted photons

In this section, we discuss the experimental implementation of the photonic quantum walk introduced in Refs. [69, 70, 71] and the bulk measurement of its topological invariants through the MCD detection. In the literature, various photonic protocols of 1D QW have been realized in dif-

ferent architectures: the walker is typically mapped onto a degree of freedom of a laser field, such as the optical path of the beam [59, 57, 58, 76, 77], the time delay between optical pulses [60, 78, 79]. Our QW, whose protocol has been discussed in Subsec. IV.1.3, exploits for the first time two degrees of freedom of paraxial beams: polarization and orbital angular momentum (OAM). Furthermore, eventhough other methods to measure topological invariants inside the bulk of chiral symmetric systems have been proposed [85, 87], so far, they have only been applied to static systems (arrays of optical waveguides) [86]. These detection schemes are also inherently different from ours, as they require the introduction of sub-lattice dependent losses and a well-defined initial state.

In SubSec. V.1.1, we introduce the OAM and we describe the optical device acting on it, the q-plate. In SubSec. V.1.2, we present the experiment: the detection of the topological invariants $\mathcal{W}_0$ and $\mathcal{W}_\pi$ through the measurements of the walker's MCD in two inequivalent time-frames. This experiment is reported in Ref. [71], figures V.2-V.6 are adapted from this paper.

V.1.1 Twisted light beams

Firstly observed in 1995 [139], the OAM has been extensively studied from a fundamental point of view [140, 89, 141, 142, 90] and it found many applications in the fields of quantum communication and simulation [143, 144, 145, 146]. Here, we provide a definition of the OAM valid for *monochromatic* and *paraxial* electromagnetic waves, as it is reported in the seminal paper of Allen et al. [140].

A wave is monochromatic when its electric field may be written as $\mathbf{E}(\mathbf{r},\mathbf{t}) = \mathbf{E}(\mathbf{r})e^{-i\omega t}$, with ω being the frequency of the radiation; a wave is paraxial when two components of its wavevector are negligible with respect to the third one, conventionally k_z, namely $k_z \approx k = \frac{\omega}{c}$ [52]. The electric field of a monochromatic and paraxial wave reads

$$\mathbf{E}(\mathbf{r},t) = \mathbf{A}(\mathbf{r})e^{i(kz-\omega t)}, \tag{V.1}$$

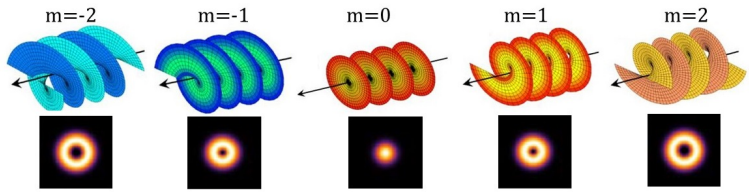

Figure V.1: **Twisted light beams.** LG modes with $p = 0$ and $m = -2, -1, 0, 1, 2$. The intensity profiles show the characteristic donut shape due to the phase singularity on the propagation axis. This image is adapted from the Wikipedia page "Orbital Angular Momentum of light", edited by L. Marrucci and E. Karimi.

with **A** satisfying the so-called *slow-varying envelope approximation* [52]:

$$\frac{\partial^2 A_i}{\partial z^2} << \frac{1}{\lambda}\frac{\partial A_i}{\partial z} << \frac{A_i}{\lambda^2}, \tag{V.2}$$

for $i = x, y$ while $A_z \approx 0$. One can define the OAM density in vacuum by using the classical definition of this quantity in terms of linear momentum density [52]:

$$\mathbf{j} \equiv \mathbf{r} \times \mathbf{p} = \mathbf{r} \times \frac{\mathbf{S}}{c^2}, \tag{V.3}$$

where c is the light's velocity in vacuum and $\mathbf{S} \equiv \frac{\mathbf{E}\times\mathbf{B}}{\mu_0}$ is the *Poynting vector* with μ_0 being the *magnetic permeability* of vacuum. The Poynting vector transports the electromagnetic power; the continuity equation for the electromagnetic energy in vacuum, known also as *Poynting theorem*, reads:

$$\frac{\partial u}{\partial t} = -\vec{\nabla} \cdot \vec{S}, \tag{V.4}$$

where $u = \frac{1}{2}\epsilon_0 E^2 + \frac{1}{2}\frac{B^2}{\mu_0}$ is the *electromagnetic energy density* with ϵ_0 being the *electric permittivity* of vacuum. Replacing Eq. (V.1) in (V.3) and

performing a time average over a period $T = 2\pi/\omega$, the z-component of the angular momentum flux, J_z, reads:

$$J_z = -i\hbar \frac{\int\int dxdy[\mathbf{E}_\perp^* \cdot (-i\mathbf{r} \times \nabla)_z \mathbf{E}_\perp + (\mathbf{E}_\perp^* \times \mathbf{E}_\perp)_z]}{\int\int dxdy \mathbf{E}_\perp^* \cdot \mathbf{E}_\perp}, \tag{V.5}$$

where $\int$ is an integral over an arbitrary volume,

$$\mathbf{E}_\perp = (E_x, E_y) \approx \mathbf{E} \tag{V.6}$$

with

$$E_{x(y)} = A(z) E^0_{x(y)} \cos\left(\omega t - \frac{z}{c} + \phi_{x(y)}\right). \tag{V.7}$$

Thus, the transverse components are the only two non-negligible components of the electric fields, as it follows straightforwardly from the first Maxwell law within paraxial approximation [52].

Since, in this approximation, E_x and E_y only differ in amplitude, $E^0_{x(y)}$, and phase, $\phi_{x(y)}$, one can express the polarization of a paraxial beam as a *Jones vector* [147], namely a complex column vector which reads

$$|E\rangle \equiv \begin{pmatrix} \mathcal{E}_x \\ \mathcal{E}_y \end{pmatrix}, \tag{V.8}$$

where $\mathcal{E}_{x(y)} = E^0_{x(y)} e^{i\phi_{x(y)}}$ and $|\mathcal{E}_x|^2 + |\mathcal{E}_y|^2 = 1$. The scalar product between two Jones vectors $|\chi\rangle$ and $|\psi\rangle$ is defined as:

$$\langle\chi|\psi\rangle \equiv \int dxdy \begin{pmatrix} \chi_1^* & \chi_2^* \end{pmatrix} \begin{pmatrix} \psi_1 \\ \psi_2 \end{pmatrix}. \tag{V.9}$$

Hence, we can safely use the bra-ket notation. The two orthogonal *linear polarizations* $\{|H\rangle, |V\rangle\}$ are conventionally chosen as the basis; in this basis, the two orthogonal left and right *circular polarizations* read:

$$\begin{aligned} |L\rangle &= \frac{|H\rangle + i|V\rangle}{\sqrt{2}}; \\ |R\rangle &= \frac{|H\rangle - i|V\rangle}{\sqrt{2}}. \end{aligned} \tag{V.10}$$

By defining the *orbital angular momentum* as

$$L_z \equiv -i(\mathbf{r} \times \nabla)_z \tag{V.11}$$

and the *spin angular momentum* (SAM) as

$$S_z \equiv \begin{pmatrix} 1 & 0 \\ 0 & -1 \end{pmatrix}, \tag{V.12}$$

then, Eq. V.5 reads:

$$J_z = \frac{\langle E|L_z|E\rangle + \langle E|S_z|E\rangle}{\langle E|E\rangle}, \tag{V.13}$$

where the denominator is a normalization term and can be safely set to one by a proper choice of the wave amplitude [140]. Thus, the angular momentum of a paraxial beam is the sum of two terms which can be regarded as the expectation values of two operators: the SAM and the OAM [140]; these two terms respectively read:

$$\langle E|S_z|E\rangle = \int\int dxdy(|\mathcal{E}_R|^2 - |\mathcal{E}_L|^2) \tag{V.14}$$

$$\langle E|L_z|E\rangle = \hbar \int\int d\rho d\phi \mathcal{E}_L^* \frac{\partial \mathcal{E}_L}{\partial \phi} + \mathcal{E}_R^* \frac{\partial \mathcal{E}_R}{\partial \phi}, \tag{V.15}$$

$\mathcal{E}_{R(L)}$ are the complex components of the polarization vector in the basis $\{|R\rangle, |L\rangle\}$ and ρ and ϕ are the polar coordinates in the transverse plane.

By putting Eq. (V.1) in the wave equation, we obtain the paraxial Helmholtz equation [52]:

$$\nabla_\perp^2 \mathbf{A} + 2ik\frac{\partial \mathbf{A}}{\partial z} = 0 \tag{V.16}$$

where $\nabla_\perp^2$ is the transverse Laplacian $\frac{\partial^2}{\partial_x^2} + \frac{\partial^2}{\partial_y^2}$. The solutions of Eq. (V.16) are called paraxial beams; they have transverse dimensions much smaller than the typical longitudinal distance over which the field changes appreciably in magnitude. Laser beams are described by a class of paraxial

beams called *Gaussian modes* as the envelope $A(\mathbf{r})$ is a Gaussian function. Other solutions of Eq. (V.16) are the *modes of Laguerre-Gauss* (LG) [140]. Laguerre-Gaussian modes in cylindrical coordinates (ρ, ϕ, z) read:

$$A_{LG} = \frac{A_0 w_0}{w(z)} \left(\frac{\rho}{w(z)} \right)^{|m|} {L_p}^m \left(\frac{2\rho^2}{w^2(z)} \right) e^{-\frac{\rho^2}{w^2(z)}} e^{i[kz + \frac{k\rho^2}{2R(z)} + m\phi - (|m|+2p+1)\zeta(z)]}, \tag{V.17}$$

where A_0 is a constant, $w(z)$ and $R(z)$ are two functions measuring respectively the beam width and the radius of curvature of the wave-front, w_0 is the beam waist, $\zeta(z)$ is the Gouy phase [52] and L_p^m is the generalized Laguerre polynomial of indices p and m, called respectively radial and azimuthal number. As shown in Fig. V.1, the integer $|m|$ counts the number of twisted wave-fronts winded up around the z axis and the sign of m yields the chirality of the helices [140]; the azimuthal phase ϕ is not defined on the optical axis where there is a singularity, namely the intensity of the LG beams is zero on the propagation axis, see the bottom row of Fig. V.1. LG modes are eigenmodes of the orbital angular momentum L_z of eigenvalue m [140]; the mode with $p = m = 0$, often indicated with TEM_{00}, is a Gaussian beam. While the circular polarizations are eigenmodes of the spin of eigenvalues ± 1.

The distinction between the SAM and the OAM of a paraxial beam is not purely formal, but has a physical meaning: the two angular momenta interact with the matter in different ways. Being absorbed by a small particle,a circularly polarized beam produces a rotation of the particle around itself [148, 149, 150], whereas a LG beam produces a revolution of the particle around the optical axis [139, 141, 142]. The distinction between SAM and OAM holds also at the level of single photons, namely each photon of a circularly polarized paraxial beam carries a well defined SAM equal to $\pm\hbar$ and an OAM equal to $\hbar m$ [89, 141].

The q-plate

In the interaction with the majority of the materials, SAM and OAM can be regarded as independent degrees of freedom [89]. However, when a

paraxial beam interacts with an inhomogeneous anisotropic medium, a polarization's flip can change the beam's OAM [144]. This phenomenon allows one to manipulate the OAM of a paraxial beam using a slab of birefringent material patterned in the transverse plane, such a device is called q-plate [91].

A *birefringent material* is a material presenting two different refractive indices n_1 and n_2 along two different directions called principal axes [52]. Thus, it introduces a phase retardation between the two polarization components oriented along the principal axes. The phase retardation δ introduced by a birefringent plate of thickness d is given by $\delta = \frac{1}{\lambda}[2\pi(n_2 - n_1)d]$, where λ is the wavelength of the incident radiation in vacuum. The Jones matrix of such a medium, in the basis of its own principal axes, reads:

$$P = \begin{pmatrix} 1 & 0 \\ 0 & e^{-i\delta} \end{pmatrix} \tag{V.18}$$

If $\delta = \pi$, the plate is called *half-wave plate* (HWP); whereas, if $\delta = \frac{\pi}{2}$, it is called *quarter-wave plate* (QWP). These names derive from the fact that the difference of optical path-length between the polarization components is $\frac{\lambda}{2}$ in the first case, $\frac{\lambda}{4}$ in the second one. In a generic frame, where the x axis forms an angle θ with one of the principal axes of the plates, the Jones matrices of the HWP ($\mathcal{H}$) and the QWP ($\mathcal{Q}$) read [147]:

$$\mathcal{H}_\theta = R^{-1}(\theta)\mathcal{H}R(\theta) = \begin{pmatrix} \cos(2\theta) & \sin(2\theta) \\ \sin(2\theta) & -\cos(2\theta) \end{pmatrix} \tag{V.19}$$

$$\mathcal{Q}_\theta = R^{-1}(\theta)\mathcal{Q}R(\theta) = \frac{1}{\sqrt{2}} \begin{pmatrix} 1 - i\cos(2\theta) & -i\sin(2\theta) \\ -i\sin(2\theta) & 1 + i\cos(2\theta) \end{pmatrix},$$

with

$$R(\theta) = \begin{pmatrix} \cos(\theta) & -\sin(\theta) \\ \sin(\theta) & \cos(\theta) \end{pmatrix}. \tag{V.20}$$

From these expressions, we can deduce that a HWP rotates the linear polarizations, whereas a QWP turns a linear polarization into a circular

polarization and vice versa. With both plates, rotated of two different angles θ and ϕ, it is possible to achieve every polarization state [147]. The Jones matrices $\mathcal{H}_\theta$ and $\mathcal{Q}_\theta$, in the circular basis $\{|R\rangle, |L\rangle\}$ read:

$$\mathcal{H}_\theta = \begin{pmatrix} 0 & e^{i2\theta} \\ e^{-i2\theta} & 0 \end{pmatrix} \tag{V.21}$$
$$\mathcal{Q}_\theta = \frac{1}{\sqrt{2}} \begin{pmatrix} 1 & -ie^{-i2\theta} \\ -ie^{i2\theta} & 1 \end{pmatrix}.$$

In addiction to the natural birefringent materials, such as quartz or mica, there exist some artificial ones [52]. For instance, a thin slab of *liquid crystal* (LC) can exhibit a refractive index along the direction in which the molecules' axes are oriented, and another along the perpendicular one. Furthermore, the phase retardation introduced by a thin slab of LC can be tuned by changing the temperature [151], or by applying a voltage to the slab [152].

The q-plate is a LC plate where the liquid crystal is arranged according to an azimuthal pattern; if one sets a couple of axes x and y in the plane, the local orientation of the LC optic axis reads:

$$\alpha = \alpha_0 + q \arctan(y/x) = \alpha_0 + q\phi, \tag{V.22}$$

where q is an integer or semi-integer number, namely the topological charge of the q-plate. The Jones matrix of the q-plate, in the linear polarizations basis, reads

$$Q = R^{-1}(\alpha) \begin{pmatrix} 1 & 0 \\ 0 & e^{-i\delta} \end{pmatrix} R(\alpha) \tag{V.23}$$

where δ is the phase retardation introduced by the liquid crystal and $R(\alpha)$ is the rotation matrix given in Eq. (V.20). In the basis of the circular polarizations Q reads:

$$Q = \begin{pmatrix} \cos(\delta/2) & ie^{-i(2\alpha_0+2q\phi)} \sin(\delta/2) \\ ie^{i(2\alpha_0+2q\phi)} \sin(\delta/2) & \cos(\delta/2) \end{pmatrix} \tag{V.24}$$

A circularly polarized beam outgoing from a q-plate contains two terms: one identical to the input, and the other having an OAM of $\pm 2q$ and a circular polarization with opposite chirality. The rate of conversion depends on the LC phase retardation δ; this parameter can be tuned at will by means of an applied voltage [152]. If we set $\alpha_0 = 0$ and $q = 1/2$, equation (V.24) yields the unitary operator Q of the quantum walk protocol in Eq. (IV.15), with ϕ being the walker's quasi-momentum k. In this chapter, we will use the letter q instead of k to denote the walker's quasi-momentum in order to avoid possible confusion with the light wavevector.

There are other devices allowing for the manipulation of the light's OAM, such as the spiral phase plate and the spatial light modulator (SLM). This latter is a LC screen whose pixels are addressed by an individually controllable voltage, and thereby it can shape the phase profile of a light beam according to almost every pattern. It is a very versatile tool whose applications go beyond the manipulation of light OAM, however it is not a scalable resource. To conclude, the q-plate offers the opportunity of coupling light's polarization and OAM in a scalable and unitary fashion and it can generate beams with high values of OAM. For these reasons, it has been employed many times in the field of quantum information [153, 154, 155, 156, 157, 158, 159], and in the fascinating branch of classical optics called *singular optics* [160, 161].

V.1.2 Implementation of the 1D DTQW and detection of the topology

Here we present the experiment reported in Ref. [71] from which the data and the figures shown in this subsection are readapted. The photonic setup of this experiment has been previously reported in [69, 70].

The QW takes place on a lattice whose discrete positions $|m\rangle$ correspond to values m of the OAM carried by the twisted light beam; the two coin states are mapped onto the left and right circular polarizations. Such a QW can be implemented in both a classical regime, i.e. using light beams as in [71], or in a single-photon regime as in [69, 70]. The uni-

tary evolution operator $U = QW$ is implemented with a couple of optical plates: a quarter wave-plate rotated by $\pi/2$ radians with respect to the horizontal direction implements the operator W, and a q-plate implements Q. Both the operators are given in Eq. (IV.14). The sketch of the setup is shown in Fig. V.2.

As we already mentioned in SubSec. IV.1.3, in order to fully characterize the system's topology in terms of $\mathcal{W}_0$ and $\mathcal{W}_\pi$, we should measure the walker's MCD in the two explicitly chiral-symmetric time-frames corresponding to the unitary operators $U_1 = \sqrt{W}Q\sqrt{W}$ and $U_2 = \sqrt{Q}W\sqrt{Q}$. However, for experimental reasons, we measured the walker's MCD in the time-frames corresponding to $U = QW$ and $\tilde{U} \equiv U_2 = \sqrt{Q}W\sqrt{Q}$. This choice does not affect the final result since the winding number of the default Floquet Hamiltonian $H = i \log U$, for every value of the parameter δ, is the same as that of $H_1 = i \log U_1$. We prepared a QW of seven steps, once within the protocol U, and once within the protocol $\tilde{U}$; we initialized the system's state in $|0\rangle \otimes |s\rangle$, with $|0\rangle$ being the state of zero OAM (TEM_{00} mode) corresponding to the center of the lattice, and $|s\rangle$ being two different polarizations for every protocol, namely $|L\rangle$ and $(|L\rangle + |R\rangle)/\sqrt{2}$; we repeated the measurement of the MCD ten times for every polarization in correspondence of different values of δ sampling the range $[0, 2\pi]$, and we took the measurements' average. As expected, in both the time-frames, the mean chiral displacement does not depend on the initial polarization and it oscillates around the value of the winding number, see Fig. V.3(b) and V.3(d). Combining the measured MCD, $\mathcal{C}(t)$ and $\tilde{\mathcal{C}}(t)$, we obtained the two observables $\mathcal{C}_0(t)$ and $\mathcal{C}_\pi(t)$ whose long time limits give, respectively, the topological invariants $\mathcal{W}_0$ and $\mathcal{W}_\pi$, see Fig. V.4.

Robustness of the mean chiral displacements to the dynamical noise

We tested the stability of the quantization of the MCD against disorder. We chose the protocol U and introduced a dynamical disorder by offsetting the optical retardation δ_j ($1 \leq j \leq 7$) of each q-plate by a small random amount $|\epsilon_j| < \Delta$ around their common mean value $\bar{\delta}$: we set

$\Delta = \pi/10$ and $\pi/5$. This disorder is dynamic, in the sense that it affects independently the various q-plates crossed by the beam, but crucially it respects chiral symmetry. As shown in Fig. V.5, in single realizations, the mean chiral displacement presents oscillations featuring higher amplitude for increasing disorder, but an ensemble average over independent realizations smoothly converges to the expected theoretical result which, in the infinite time limit, gives the winding number. A similar robustness of the chiral displacement shall hold for every 1D QW chiral protocol, and more generally for every 1D chiral system, as long as the disorder does not break chiral symmetry and its strength is smaller than the gap size, as it is shown in Fig. V.6 for the SSH model.

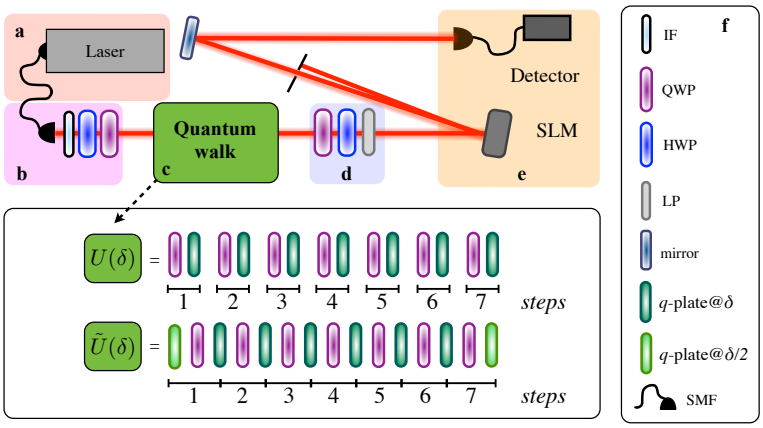

Figure V.2: **Scheme of the experimental setup of the 1D chiral DTQW**. **a.** The output of a Ti:Sa pulsed laser source (pulse duration = 100 fs, central wavelength = 800 nm, repetition rate = 82 MHz) is coupled into a single mode fiber (SMF) so as to clean the laser spatial mode; this provides a single OAM state with $m = 0$ at the input of the QW. **b.** At the exit of the fiber, the beam passes through an interferential filter (IF), whose transmittance is peaked at 800 nm with bandwidth of 3 nm, which allows to have a stable control of the light's wavelength and a narrower frequency distribution. Then the desired input polarization state is prepared by means of a half-wave plate (HWP) and a quarter-wave plate (QWP). **c.** The light beam passes through a sequence of QWPs and q-plates, as shown in detail in the inset, which are positioned in order to realize either protocol U or $\tilde{U}$. **d.** At the end of the QW, a polarization component is selected by means of a QWP and a HWP, followed by a linear polarizer (LP). **e.** The OAM spectrum is measured by diffraction on a spatial light modulator (SLM), that displays standard pitchfork holograms for the projection over OAM states. At the first diffraction order, the light is coupled into a SMF that is directly connected to a power meter recording the field intensity. **f.** Legend of optical components displayed in panels **a**-**e**.

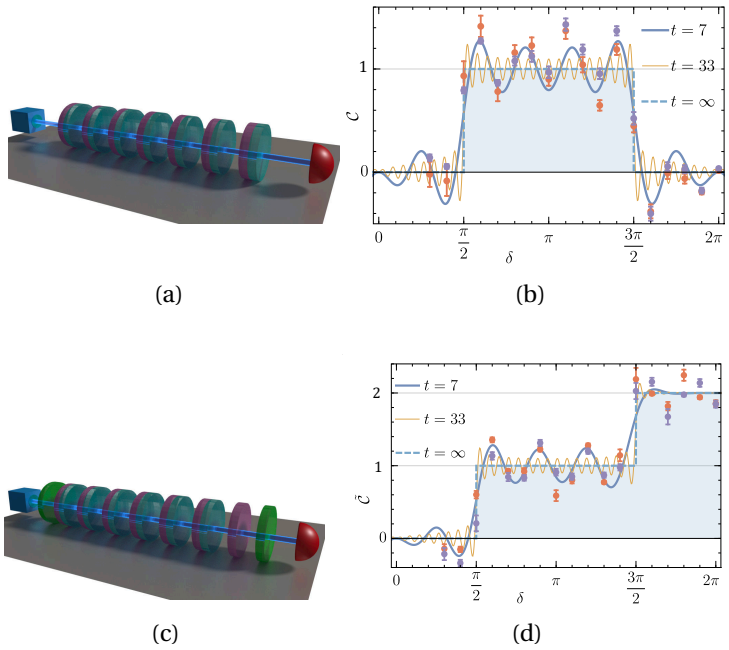

Figure V.3: **Detection of the winding numbers for the two protocols U and $\tilde{U}$ a.** Sketch of the setup implementing the default protocol $U = QW$. A light beam performs a QW by propagating through a sequence of quarter-wave plates (purple disks) and q-plates (turquoise disks). **b.** Mean chiral displacement $\mathcal{C}$ after a 7-steps QW of protocol U vs. the optical retardation δ. Each data point is an average over ten different measurements (error bars are the associated standard errors). Purple and red dots refer, respectively, to different input polarizations, $|L\rangle$ and $(|L\rangle + |R\rangle)/\sqrt{2}$. The lines represent the expected value of the MCD for different values of the time t. In the long time limit the MCD converges to the winding number of the Floquet Hamiltonian (straight dotted line). **c.** Sketch of the setup implementing the protocol $\tilde{U} = \sqrt{Q} \cdot W \cdot \sqrt{Q}$. The two q-plates at the beginning and end of the optical path (shown in bright green) yield an optical retardation $\delta/2$, where δ is the optical retardation characterizing bulk q-plates (turquoise). **d.** Mean chiral displacement $\tilde{\mathcal{C}}$ after a 7-steps QW with protocol $\tilde{U}$.

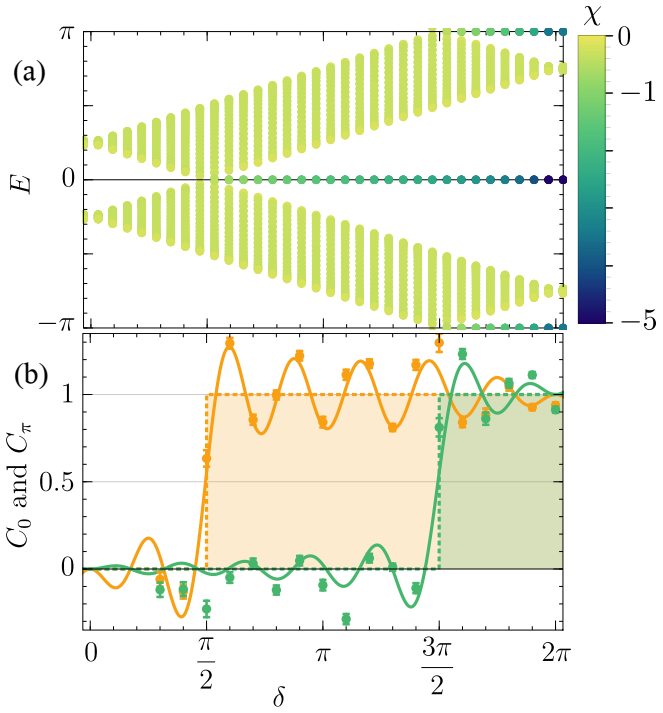

Figure V.4: **Bulk-edge correspondence for the chiral symmetric DTQW. a.** Quasi-energy spectrum of the effective QW Hamiltonian within open boundary conditions for a chain of $2N+1=21$ cells. The plot is taken from Ref. [71]. The color coding of the spectrum indicates the degree of localization $log_{10}(1-|\langle\hat{m}\rangle)|/N)$ of each eigenstate on the two edges $m=-N, m=N$; light (dark) colors indicate bulk (edge) states. The spectrum looks similar to the one of the static SSH model (Fig. II.3) but here localized edge states have both effective energy 0 and π. **b.** Time average of the measured mean chiral displacements $\mathcal{C}_0(t)\equiv\frac{\mathcal{C}_1(t)+\mathcal{C}_2(t)}{2}$ (green line) and $\mathcal{C}_0(t)\equiv\frac{\mathcal{C}_1(t)-\mathcal{C}_2(t)}{2}$ (orange line). The points are obtained averaging the results obtained from the two different initial states (the error bars are the propagated standard error). Their long-time limits, namely the topological indices $\mathcal{W}_0$ and $\mathcal{W}_\pi$ (dotted lines), yield respectively the number of edge states at energy 0 and π.

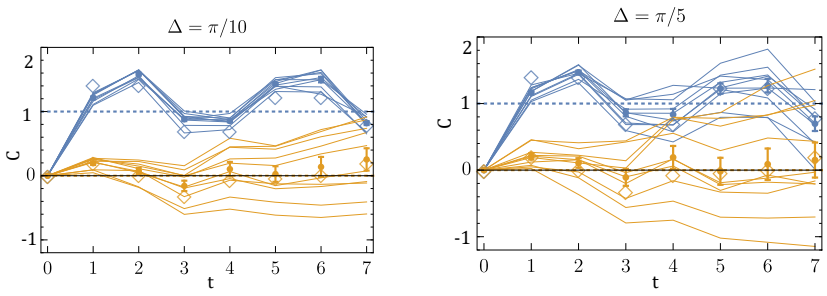

(a) (b)

Figure V.5: **Robustness of the MCD to dynamical disorder.** Measurement of the mean chiral displacement $\mathcal{C}$ of protocol U for a localized input state in presence of dynamical disorder. For the orange (blue) lines, we chose a mean value of the q-plate optical retardation $\bar{\delta} = 7\pi/4$ ($\bar{\delta} = \pi$), expected to yield a winding number $\mathcal{W} = 0$, and we add at each time step a small random retardation $|\epsilon| < \Delta$, with $\Delta = \pi/10$ (**a**) and $\pi/5$ (**b**). Thin solid lines display the measurements of single realizations, and their average is shown as filled circles (error bars are the standard error of the mean). In all plots, empty diamonds represent theoretical simulation calculated for the ideal case $\Delta = 0$ and dotted lines the expected result for $t \to \infty$.

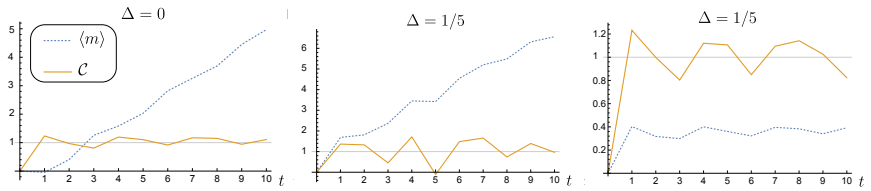

(a) (b) (c)

Figure V.6: **Mean displacement and mean chiral displacement in the SSH model with dynamical disorder.** Evolution of a walker on an SSH lattice with dynamical disorder in the tunnelings a and b. The disorder is implemented by discretizing the time of the system's evolution and by adding to a, at each discrete time, a small random amount chosen in the range $[-\Delta/2, \Delta/2]$. At $t = 0$, the walker is initialized on the central unit cell of the chain, with a random polarization (different for each realization); we set $a = b/2$, so that the SSH Hamiltonian (II.12) is in the topological phase phase $\mathcal{W} = 1$. Dashed (solid) lines depict the mean (mean chiral) displacement. **a.** Single realization in absence of disorder. **b.** Single realization with disorder amplitude $\Delta = 1/5$. **c.** Ensemble-average over 100 realizations of disorder with $\Delta = 1/5$:the mean chiral displacement smoothly converges to $\mathcal{W}$.

V.2 2D quantum walk in the momentum space of structured light

In this section, we describe the implementation and the topological characterization of the 2D DTQW whose protocol has been introduced in SubSec. IV.2.2. This experiment is reported in Ref. [80] and all the figures in this section are adapted from this paper.

The experimental research on QWs has been almost entirely focused on 1D walks, few exceptions are the studies presented in Refs. [78, 79, 94] where a 2D walk is cleverly simulated by folding a 2D lattice in a 1D chain and in Ref. [74], where path and OAM encoding are combined. Very recently, a continuous-time walk has been realized in a 2D array of coupled waveguides [92]. In our 2D QW, the coin is still encoded in the light polarization, but the walker position is now encoded in the transverse wavevector of the beam which is manipulated by means of polarization-dependent diffraction gratings; to our knowledge, this mapping has never been used in any previous platform. Here we use a 2DQW to simulate a Floquet Chern insulator; these systems, so far, have only been realized with cold atoms in periodically driven optical potentials [32, 33, 38, 34] and with arrays of helical waveguides [51].

In SubSec. V.2.1, we describe the photonic platform. In SubSec. V.2.2, we consider the dynamics of several wave-packets moving under a constant force acting in one direction, and we extract the Chern number of the QW from their transverse displacement. Various methods to detect topology through the center of mass displacement have been proposed [10, 31, 162, 99] and implemented in various simulators [116, 38, 35, 163, 164]; nonetheless, it is the first time that this method is used to detect the Chern number of a 2DQW.

V.2.1 Experimental setup

The scheme reported in Ref. [80] is based on mapping the coin onto the circular polarizations $\{|L\rangle, |R\rangle\}$ (as in our first scheme based on twisted

light), and the walker's position onto the transverse component of the beam wavevector. Let us stress that, since, in our encoding, the walker's position corresponds to the light's wavevector, then, the walker's quasi-momentum corresponds to the light's transverse position. To our knowledge, this encoding has not been considered hitherto in any photonic platform. As walker's states, we use a family of Gaussian modes whose transverse wavevector assumes the discrete values $\mathbf{k}_\perp = \Delta k_\perp \mathbf{m}$, where $\mathbf{m} = (m_x, m_y)$ are the integer walker's coordinates on the square lattice, and the lattice spacing $\Delta k_\perp$ is taken to be much smaller than the longitudinal momentum component $k_z \approx 2\pi/\lambda$ (λ is the light wavelength). Then, the modes propagate along a direction slightly tilted with respect to the z axis; their explicit expression reads:

$$|\mathbf{m}\rangle = A(\mathbf{r}) e^{i[\Delta k_\perp (m_x x + m_y y) + k_z z]}, \tag{V.25}$$

where $A(\mathbf{r})$ is a Gaussian envelope with waist w_0.

The Floquet operator of our protocol is $U = Q_y Q_x W$, see SubSec. IV.2.2, where Q_x,Q_y and W are given in Eq. (IV.23). The operators Q_x and Q_y are implemented with LC devices similar to standard q-plates (V.24), the g-plates. The difference is that, in the g-plate, the liquid crystal is arranged in the plane of the slab according to a pattern which depends linearly from the transverse coordinate (see Fig. V.7); the local orientation α of the LC optic axis in the plane of the plate reads

$$\alpha = \frac{\pi}{\Lambda}\, i + \alpha_0, \tag{V.26}$$

with $i = x, y$, α_0 being the residual angle at $i = 0$ and Λ being the g-plate's spatial periodicity yielding the lattice spacing $\Delta k_\perp = 2\pi/\Lambda$. The g-plates' action in the basis of circular polarizations reads:

$$\begin{aligned} Q_x|\mathbf{m}\rangle \otimes |L\rangle &= \cos\left(\frac{\delta}{2}\right)|\mathbf{m}\rangle \otimes |L\rangle + i \sin\left(\frac{\delta}{2}\right) e^{i2\alpha_0}|m_x + 1, m_y\rangle \otimes |R\rangle, \\ Q_x|\mathbf{m}\rangle \otimes |R\rangle &= \cos\left(\frac{\delta}{2}\right)|\mathbf{m}\rangle \otimes |R\rangle + i \sin\left(\frac{\delta}{2}\right) e^{-i2\alpha_0}|m_x - 1, m_y\rangle \otimes |L\rangle. \end{aligned} \tag{V.27}$$

The action of Q_y is obtained replacing x with y in Eq. (V.27). In the following, for simplicity, every time we will have to refer to one of the transverse directions, we will use x. The birefringent optical retardation δ of the g-plates may be controlled dynamically through an applied voltage as in the q-plates.

For the coin rotation W this time has been used a g-plate yielding the transformation of a standard quarter-wave-plate, namely a g-plate with $\delta = \pi/2$ and $\alpha = 0$. In this way, all the QW operators are physically implemented by plates having exactly same size and shape. This allows for mounting them in a compact system realized by a 3D printing technique (see Fig. V.7) which reduces the distance between consecutive steps. Making the inter-step distance as short as possible is crucial in order to minimize the relative phases between the rays forming the same mode. Indeed, each output mode $|\mathbf{m}\rangle$ corresponds to a superposition of waves which have followed different trajectories during the QW, accumulating relative phases which act as a decoherence process. In our platform, these phases are negligible ($\approx 10^{-3}\pi$) and then the physical system realizes with a very good approximation the ideal (perfectly coherent) QW protocol.

The experimental setup is sketched in Fig. V.7. A collimated Gaussian laser beam passes through the sequence of LC devices implementing the QW. At the exit of the walk, a camera placed in the focal plane of a lens reads out the field intensity providing the probability distribution of the walker's positions. Indeed, the lens performs a Fourier transform of the Gaussian beam: in its focal plane, each mode $|\mathbf{m}\rangle$ corresponds to a spot centred in a point of coordinates $\mathbf{R} = \frac{2\pi\Delta k_\perp \mathbf{m}}{\lambda f}$, with f being the focal length; the diameter of the spot is given by the waist of the Fourier transform of the beam, i.e. $\widetilde{w}_0 = 2/w_0$. The frequency of the g-plates Λ and the input beam waist w_0 have been chosen in order to have a negligible overlap between neighbour spots.

Figure V.8 shows the measured probability distribution after a 2DQW of 5 steps for a walker starting localized at $\mathbf{m} = (0,0)$. All the data show a good agreement with the numerical simulations of the ideal QW dynamics. A quantitative comparison between experimental P^e and simulated

P^s distributions is provided by computing the Similarity $S = \frac{\left(\sum_m \sqrt{P^e_m P^s_m}\right)^2}{\left(\sum_m P^e_m \sum_m P^s_m\right)}$.

V.2.2 2D motion under a constant force: anomalous displacement and Chern number

Simulating a constant force in a DTQW

Quantum walks with an extra constant driving, often referred to as electric quantum walks [95, 62, 96], have attracted attention for the study of phenomena such as quantum state refocusing and probability distributions revivals [95, 97, 98, 96], Bloch oscillations and Landau-Zener transitions [62] and for the measurement of topological invariants [63, 64, 65, 66].

A constant force acting on QW along one direction (x) can be simply simulated by a modified single-step operator [62, 65, 66]. Indeed, the operator implementing the potential of the constant dimensionless force, $F^x\hat{x}$, can be regarded as a translation of the walker's quasi-momentum component q^x of a quantity F^x. Since the only dependence on the quasi-momentum q^x is contained in the g-plate operator Q_x:

$$Q_x(q^x) = \begin{pmatrix} \cos(\delta/2) & ie^{-iq^x}\sin(\delta/2) \\ ie^{iq^x}\sin(\delta/2) & \cos(\delta/2) \end{pmatrix}, \tag{V.28}$$

thereby, at the t-th step, the Bloch Floquet operator of the QW reads:

$$\tilde{U}(\mathbf{q},t) \equiv \tilde{U}(q^x + F^x t, q^y) = Q_y(q^y)e^{-it\frac{F^x}{2}\sigma_z}Q_x(q^x)e^{it\frac{F^x}{2}\sigma_z}W. \tag{V.29}$$

The force can be implemented by progressively displacing the g-plates without using any additional optical device: the g-plate which acts at time step t is shifted laterally along the x direction by an amount of $\Delta_x = \frac{-t\Lambda F^x}{2\pi}$.

Adiabatic dynamics of a filled band under a constant force

Let us assume to be in adiabatic regime, namely that the variation $q^x(t) = q^x_0 + F^x t$ is slow with respect to the frequency associated to the gap of the

effective energy spectrum. As derived in Refs. [165, 99], in the adiabatic approximation, the semi-classical equations of motion of a wave-packet initially peaked around an energy eigenstate $e^{i\mathbf{q}_0\mathbf{m}_0}|u_\pm(\mathbf{q}_0)\rangle$ read:

$$\begin{aligned}\dot{m}_i &= \partial_{q_i}\epsilon_\pm(\mathbf{q}) - \dot{q}^j\Omega_{ij}^{(\pm)}(\mathbf{q}),\\ \dot{q}^i &= F^i,\end{aligned} \tag{V.30}$$

where i and $j \in \{x, y\}$, $\pm$ are the band indices, $\epsilon_\pm$ is the energy dispersion and $\Omega_{ji}^{(\pm)} = -\Omega_{ij}^{(\pm)}$ is the Berry curvature (II.25).

Hence, the components of the particle velocity read

$$\dot{m}_i = \partial_{q_i}\epsilon_\pm(\mathbf{q}) + F^j\Omega_{ji}^{(\pm)}(\mathbf{q}), \tag{V.31}$$

where $\partial_{q_i}\epsilon(\mathbf{q})$ is the standard group velocity vg_i of the band and $F^j\Omega_{ji}$ is the anomalous velocity. It comes straightforwardly that, if the system's state is an homogeneous superposition of all the upper (lower) band's eigenstates, the overall mean displacements read:

$$\begin{aligned}\langle\Delta m_y(t)\rangle_\pm &= \frac{F^x\nu^{(\pm)}}{2\pi}t,\\ \langle\Delta m_x(t)\rangle_\pm &= 0,\end{aligned} \tag{V.32}$$

where $\nu^{(\pm)}$ is the upper (lower) band's Chern number (Eq. (II.26)). The total displacement along the x direction is null since the integrals of both components of the standard group velocity over the Brillouin zone are zero.

Wave-packet's dynamics with no external force

In our experiment, we use as initial states Gaussian wave-packets sharply peaked around specific values of the quasi-momentum $\mathbf{q}_0$ and belonging to one energy band of the Floquet Hamiltonian; we denote these states as $|\Psi_g(\mathbf{q}_0, \pm)\rangle$. These wave-packets are physically generated as

narrow Gaussian beams with a small waist w_g (with $w_g \ll \Lambda$), centred around specific transverse positions $\mathbf{r}_\perp = \mathbf{q}_0\Lambda/(2\pi)$, and with polarizations equal to the eigenstates of the Floquet Hamiltonian $|u_\pm(\mathbf{q}_0)\rangle$. The transverse position $\mathbf{r}_\perp$ is controlled by translating the whole QW setup (mounted on a single motorized mechanical holder) with respect to the input laser beam. In the simulated square lattice of the walker's positions the states $|\Psi_g(\mathbf{q}_0, \pm)\rangle$ are delocalized and cover multiple lattice sites $\mathbf{m}$, but with a well defined average position $\langle\mathbf{m}\rangle$. Since they approximate the system's eigenstates, if we set the external force to zero, they propagate by preserving their shape, with a dynamics dictated by the standard group velocity, see Fig. V.9. Figure V.9(c) shows the linear motion of a gaussian wave-packet under the QW evolution with no force. In Fig. V.9(d), we retrieve the band's group velocity by measuring the trajectories of 22×22 wavepackets belonging to the upper band of the Floquet spectrum. The overall displacement of the band, obtained by summing the data, is very close to the value of zero expected for a band insulator, see Eqs. (V.32) with $F^x = 0$.

Wave-packet's dynamics under a constant force and Chern number detection

The Chern number of the Floquet Hamiltonian of our QW is extracted from the overall transverse displacement of the upper band under a force $F^x = \pi/20$, see Fig. V.10. The total transverse displacement is obtained by summing up the transverse displacements measured for 11×11 distinct wave-packets $|\Psi_g(\mathbf{q}_0, -)\rangle$ which provide an homogeneous sampling of the Brillouin zone.

We choose two values of δ corresponding to two different topological sectors: $\delta = \pi/2$, where the lower band's Chern number is $\nu^{(-)} = 1$, and $\delta = 7\pi/8$, where the lower band's Chern number is $\nu^{(-)} = 0$, see Fig. IV.4(a). At $\delta = \pi/2$, topological edge states arise only in the gap of the Floquet energy spectrum centered around zero. Thereby, for this value of δ, the Chern number provides the correct bulk-edge correspondence, see Fig. IV.4(c). However, for other values of δ, for example, $\delta = 7\pi/8$, the

Chern number's value is zero, but topological edge states are expected to arise simultaneously in both the gaps of the Floquet energy spectrum, see Fig. IV.4(d). For this reason, as we mentioned in the previous chapter, the full topological classification of 2D QWs is given in terms of the invariants W_0 and W_π, which count separately the topological edge states in the two gaps of the Floquet energy spectrum.

In Figs. V.10(a) and V.10(b), experimental data (points) are compared to the numerical simulations of the ideal QW dynamics (dashed lines) and to the overall lower band's displacement predicted by the semi-classical theory within adiabatic regime, Eq. (V.32) (black continuous line). At $\delta = \pi/2$, the energy bandgap ≈ 1 is sufficiently larger than the applied force $F_x = \pi/20$ to ensure the validity of the adiabatic approximation. However, the measured overall displacements of the lower band $\langle \Delta m_y(t) \rangle_-$ (blue empty markers) and $\langle \Delta m_x(t) \rangle_-$ (red empty markers) diverge from the semi-classical predictions. To reduce this discrepancy, which we ascribe to residual group-velocity effects, we consider also the inverse protocol whose evolution is defined by the Floquet operator $U^{-1} = W^{-1} Q_x^{-1} Q_y^{-1}$. Indeed, the bands of this inverse protocol have the same dispersion as the direct one U, but feature opposite Chern numbers. In this way, if filling the same band, we expect to observe identical contributions from the group velocity dispersion, while the anomalous displacement should be inverted. $(\langle \Delta m_y(t) \rangle_U - \langle \Delta m_y(t) \rangle_{U^{-1}})/2$ and $(\langle \Delta m_x(t) \rangle_U - \langle \Delta m_x(t) \rangle_{U^{-1}})/2$ (solid markers) show a better agreement with the expected results. The measured value of the Chern number extracted from the improoved measurement at $\delta = \pi/2$ is $\nu^{(-)} = 1.19 \pm 0.13$, consistent with the theoretical value of 1 (errors are given at one standard deviation) and at $\delta = 7\pi/8$ is $\nu^{(-)} = 0.10 \pm 0.15$ consisted with the expected 0 value.

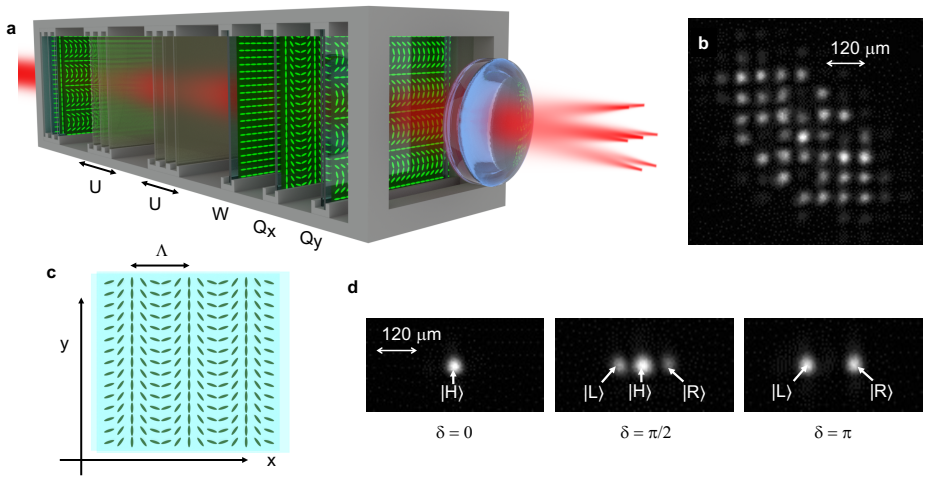

Figure V.7: **Platform working principle. a.** Sketch of the setup. A collimated beam crosses a sequence of LC devices which implement either coin rotations (W) or spin-dependent walker discrete translations (Q_x and Q_y) forming the Floquet operator $U = Q_y Q_x W$. Each shift of the walker position (transverse wavevector) tilts slightly the photon propagation direction. The QW is mounted in a compact holder, so that the transverse diffraction is negligible and the entire evolution effectively occurs in a single beam. At the QW exit, a lens performs the beam Fourier transform. **b.** The light intensity pattern which appears in the focal plane of the lens is directly imaged on a camera. It is a grid of small Gaussian spots of radius ≈20 μm spaced of $\approx$ 63 μm. The normalized intensities of the spots give the probability distribution of the walker's positions. **c.** Pattern of the LC optic-axis in a g-plate implementing a Q_x operator. The spatial period Λ fixes the lattice spacing $\Delta k_\perp = 2\pi/\Lambda$. **d.** Action of a single Q_x on a state $|\Psi_0\rangle = |\mathbf{m}, H\rangle$, with $\mathbf{m} = (0,0)$, for different values of the optical retardation δ. For $\delta = 0$, the device acts as the identity operator; for $\delta = \pi/2$, the final state is $|\Psi_{\text{out}}\rangle = |m_x, m_y, H\rangle/\sqrt{2} + |m_x - 1, m_y, L\rangle/2 + |m_x + 1, m_y, R\rangle/2$, i.e. three spots are visible; for $\delta = \pi$, $|\Psi_{\text{out}}\rangle = (|m_x - 1, m_y, L\rangle + |m_x + 1, m_y, R\rangle)/\sqrt{2}$, i.e. two spots are visible.

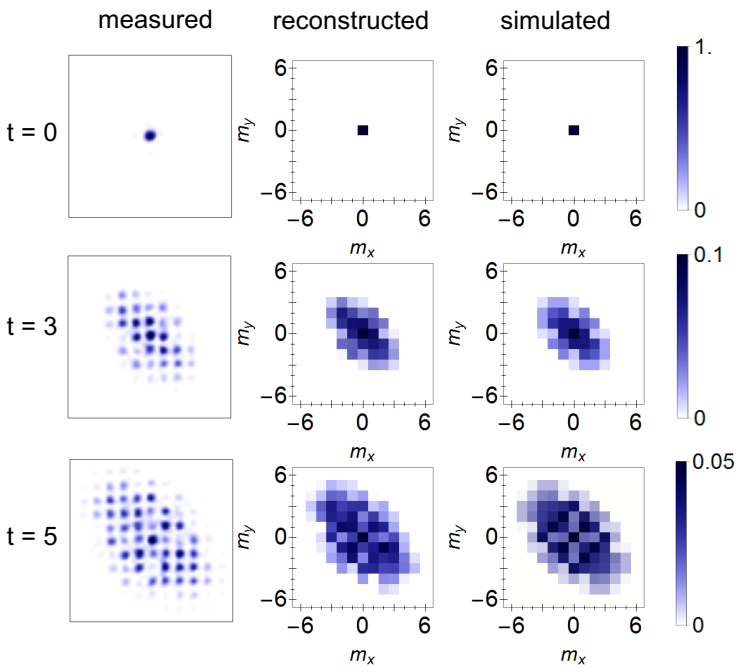

Figure V.8: **2D Quantum Walk with localized input state.** Probability distributions of the walker's positions for a QW with initial state $|\Psi_0\rangle = |\mathbf{m}, H\rangle$, with $\mathbf{m} = (0,0)$, and optical retardation $\delta = \pi/2$. From top to bottom, we display results after 0, 3, and 5 steps. From left to right, we show: measurements, probabilities reconstructed by integrating and normalizing the light intensities of the Gaussian spots, and numerical simulations. The excellent agreement between the theoretical and the measured distributions is quantified by the similarity, which equals $S = 98.2\% \pm 0.5\%, 98.0\% \pm 0.3\%, 98.0\% \pm 0.2\%$ for the distributions at $t = 0, 3, 5$, respectively. The data points are averages over four independent measurements. The uncertainties on the values of S are obtained by propagating the standard errors of the mean.

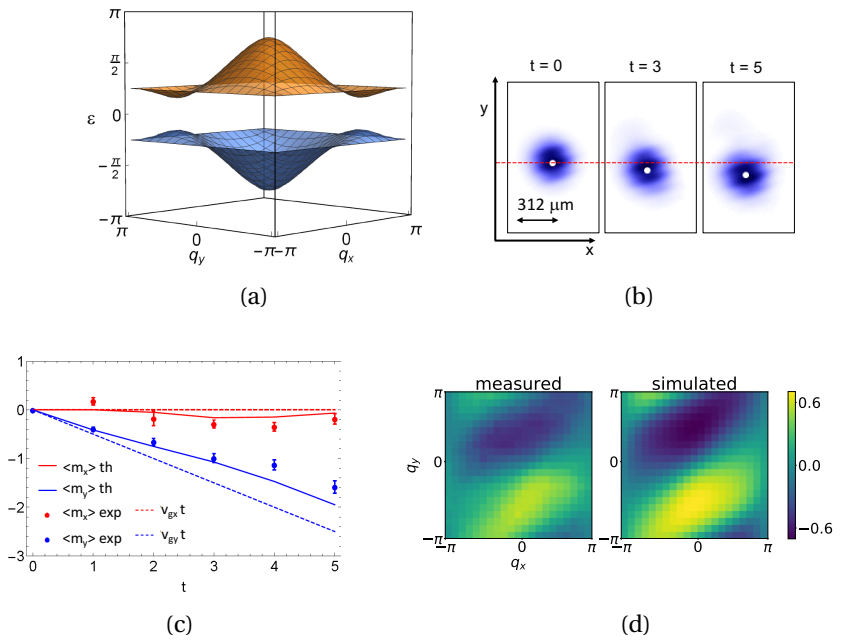

Figure V.9: **Wave-packet's dynamics without external force. a.** Effective energy $\varepsilon_{\pm}(\mathbf{q})$ at $\delta = \pi/2$. **b.** Light intensity distribution measured for a wave-packet $|\Psi_g(\mathbf{q}_0, +)\rangle$ with $\mathbf{q_0} = (-\pi/2, \pi)$ which evolves through our QW without external force. For this value of the quasi-momentum, the group velocity components are expected to be $vg_x = 0$ and $vg_y = -0.5$. The coloured marker correspond to the center of mass. The width of the initial beam is $150\,\mu$m on the plane of the camera, corresponding to a wave-packet covering a diameter of ≈ 5 lattice sites. **c.** Dynamical evolution of the center of mass of $|\Psi_g(\mathbf{q}_0, +)\rangle$. Experimental results (points) are compared to numerical simulations (continuous lines) and to semi-classical predictions (dashed lines). **d.** Measured and simulated group velocity component vg_y, for 22×22 values of the quasi-momentum in the Brillouin torus. The experimental vg_y has been extracted from the displacements of the center of mass of the corresponding wave-packets through a linear fit.

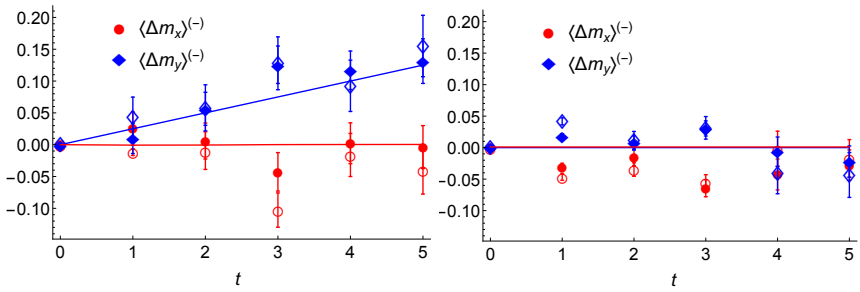

Figure V.10: **Anomalous displacement under a constant force a**, Overall center-of-mass average displacements of the lower band $\langle \Delta m_x \rangle^{(-)}(t)$ and $\langle \Delta m_y \rangle^{(-)}(t)$ under a force $F^x = \pi/20$ measured for $\delta = \pi/2$. Empty markers show results from the simple protocol U, while solid symbols show the improved results obtained by combining protocol U with its inverse U^{-1}. Straight lines correspond to the theoretical results dictated by the semi-classical equations of motion, predicting an anomalous displacement proportional to the band Chern number. **b**, Center of mass displacements of the lower band under a force $F^x = \pi/20$ measured with $\delta = 7\pi/8$. Meaning of all symbols and lines as in panel a. Statistical uncertainties include estimated misalignment effects.

VI

Conclusions and outlooks

The work presented in this thesis consisted in designing protocols and detection methods to simulate and characterize non-interacting topological insulators in 1- and 2D. We studied both static and Floquet Hamiltonians based on different architectures and paid a particular attention to quantum walk protocols and photonic implementations. We focused on detection methods of the topological invariants of the systems directly inside their bulk. Thereby, our proposals perfectly fit simulation platforms with no physical boundaries, as for instance the ones in Refs. [70, 71, 80].

The first result presented in this thesis is the derivation of a method to detect the topological invariant associated to 1D chiral-symmetric topological insulators, the winding number. We showed that the winding number can be directly read out from the free dynamics of the bulk through the measurement of the mean chiral displacement (MCD). We derived analytically this equivalence in the quasi-momentum space of a clean and infinite chiral system [83]. The MCD measurement does not require any external intervention, such as forces, losses nor interferometric setups, and it can be accomplished in systems both static and periodically driven with any internal dimension [83]. This method has, then, first been applied to a 1D chiral-symmetric QW taking place in the space of

the light's OAM [71]. Furthermore, we measured the MCD in two inequivalent timeframes in order to characterize the full topology of the Floquet system. Indeed, QW protocols are periodically driven systems and are described by effective Floquet Hamiltonians, the bulk-edge correspondence for 1D chiral-symmetric Floquet Hamiltonians is expressed by a couple of winding numbers instead of just one. These invariants can be extracted by two versions of the unitary operator of the QW protocol written in two different time-frames [75]. In the experiment, we implemented these two versions, changing the optical devices at the edges of the sequence, and we measured their MCDs.

Recently, it has been pointed out [166] that 1D discrete time QWs can realize the so-called *dynamical topological phase transition* which can arise in topological Hamiltonians undergoing a quench [167]. The dynamical topological phases are labelled by *dynamical topological invariants* which generalize the standard Berry phases: finding and implementing a method to detect such numbers might be an interesting outlook for our research on topological QW.

Then, we have shown that the MCD measurement can also be used in disordered systems. We derived both the MCD and the winding number in the real space of chiral systems with broken translation symmetry and we showed that they still converge to the same quantity in the long time limit. The MCD measurement allowed for the detection of disorder-driven topological phase transitions in a synthetic chiral-symmetric wire [50]. The experiment, performed within an ultra-cold atoms simulator, has been the first experimental observation of the so-called topological Anderson insulator (TAI) which is a disorder driven topological insulator.

Finally, we contributed to the theoretical proposal of a 2D photonic QW experiment [80], in particular, with a method to measure the Chern number inside the bulk of the system. This QW simulates a Floquet Chern insulator in the space of the transverse wavevector of a light beam. It is the first inherently 2D implementation of a topological QW and the first QW setup exploiting the transverse components of the light wavevector as synthetic dimensions. In this experiment, we characterized the system by measuring one band's Chern number. We extracted it from the over-

all transverse displacement of the band under a constant force. In order to achieve a cleaner experimental estimate of the Chern number, we exploited the symmetry of the spectrum of the QW effective energy: we combined the overall band's transverse displacement measured for the QW unitary operator and the one measured for the inverse unitary operator. While, in static Chern insulators, the bulk-edge correspondence is provided by the system's Chern number, in Floquet Chern insulators, it is expressed by a couple of invariants [44]. In the specific case of our model, characterized by two bands which are symmetric around zero quasi-energy, edge states may appear independently within the gap centred at quasi-energy 0, or within the gap at quasi-energy $\pm\pi$. The bulk-edge correspondence of such systems is provided by a couple of topological invariants $\mathcal{W}_0$ and $\mathcal{W}_\pi$, which count, respectively, the number of pairs of edge modes in the 0-energy and π-energy gaps. An interesting prospect would be to propose and implement a method to measure these invariants in the bulk of a 2D topological QW. In general, the photonic 2D QW is a new and versatile resource, which paves the way to various interesting outlooks. For instance, changing the symmetries of our unitary protocol, it might be possible to address different topological classes [3] in 2D.

Furthermore, it might be possible to add another degree of freedom to the beams, like for instance the OAM, and accomplish a system with three synthetic dimensions [168]. This could allow us to simulate 3D topological classes. In this scenario, it would be interesting to focus on the 3D chiral class and to detect the associated invariant through a 3D generalization of the MCD.

The platform may also be adapted to simulate a 2D crystal with quantized quadrupole momentum, a *quadrupole insulator* [169]. In particular, in order to implement the minimal model proposed by Benalcazar, Bernevig and Hughes, one should find the suitable optical devices to introduce controllable phases in the hopping terms of the effective Hamiltonian.

Finally, it is interesting to study how to simulate some kind of interaction among the walkers in one or two dimensions. A way to accomplish

this can be for instance to add some non-linear optical effect to the QW mapped onto the wavevector space of the light beam: we could work in a quantum regime and exploit the phase-matching conditions to couple the wavevectors of different photons. In this frame, finding an analogue of the MCD for interacting chiral systems would provide a way to detect the topology of the latter. The idea might be developed following the line of thought displayed in the works of Gurarie [170], and Gurarie and Essin [171]. They provided an expression of the topological invariant of Chiral systems in terms of the zeros of the Green's functions; we may try to find a bulk observable containing this quantity and being measurable in simulation experiments.

VII

Appendix

VII.1 Detection of the winding number in translationally invariant systems

VII.1.1 Mean displacement

In terms of projectors on energy eigenstates, the mean displacement of a generic localized state $\overline{|\Psi\rangle}$ reads:

$$\langle \hat{m}(t)\rangle_{\overline{\Psi}} = \oint \frac{\mathrm{d}k}{2\pi} \sum_{j,j'=\pm 1,\ldots,\pm\mathcal{D}/2} \langle\Psi|P_j U^{-t}(i\partial_k)U^t P_{j'}|\Psi\rangle. \tag{VII.1}$$

Using $\partial_k U^t P_{j'} = e^{-itE_{j'}}[(-it\partial_k E_{j'})P_{j'} + |\psi'_{j'}\rangle\langle\psi_{j'}| + |\psi_{j'}\rangle\langle\psi'_{j'}|]$, we have

$$\begin{aligned} P_j U^{-t}\partial_k U^t P_{j'} &= e^{itE_j} P_j \partial_k U^t P_{j'} \\ &= \delta_{jj'}[-it(\partial_k E_j)P_j + |\psi_j\rangle\langle\psi'_j|] + e^{it(E_j - E_{j'})} P_j|\psi'_{j'}\rangle\langle\psi_{j'}|. \end{aligned} \tag{VII.2}$$

Mean displacement in $\mathcal{D} = 2$

For $\mathcal{D} = 2$, we will denote with $+/-$ the positive/negative energy eigenstates, so that the skew polarization is simply $\mathcal{S} = i\langle\psi_+|\psi'_-\rangle$. Multiplying

Eq. (VII.2) by $(+i)$, using $|\psi_+\rangle\langle\psi_-| - |\psi_-\rangle\langle\psi_+| = Q\Gamma$, and inserting a completeness relation $P_+ + P_- = \mathbb{I}$ after $|\psi_j\rangle\langle\psi_j'|$, one finds:

$$\langle\hat{m}(t)\rangle_{\overline{\Psi}} = \oint \frac{\mathrm{d}k}{2\pi}\Big\{t\partial_k E_+\langle Q\rangle_\Psi + \sin(2tE_+)\mathcal{S}\langle iQ\Gamma\rangle_\Psi - \mathcal{S}[1-\cos(2tE_+)]\langle\Gamma\rangle_\Psi\Big\}. \tag{VII.3}$$

Now we use the following relations:

- $Q = \mathbf{n}\cdot\boldsymbol{\sigma}$
- $iQ\Gamma = -n_y\sigma_x + n_x\sigma_y$
- $\mathcal{S}\langle iQ\Gamma\rangle = \langle\partial_k\mathbf{n}\cdot\boldsymbol{\sigma}\rangle/2$
- $\mathcal{S}[1-\cos(2tE_+)] = 2\mathcal{S}\sin^2(tE_+) = \sin^2(tE_+)(\mathbf{n}\times\partial_k\mathbf{n})$.

Then Eq. (VII.3) may be written as:

$$\begin{aligned}\langle\hat{m}(t)\rangle_{\overline{\Psi}} = \oint \frac{\mathrm{d}k}{2\pi}\Big\{&t\partial_k E_+\langle\mathbf{n}\cdot\boldsymbol{\sigma}\rangle_\Psi \\ &+ \frac{\sin(2tE_+)}{2}\langle\partial_k\mathbf{n}\cdot\boldsymbol{\sigma}\rangle_\Psi - \sin^2(tE_+)(\mathbf{n}\times\partial_k\mathbf{n})\langle\Gamma\rangle_\Psi\Big\}.\end{aligned} \tag{VII.4}$$

In the particular case of a chiral localized state $\overline{|\Gamma_j\rangle}$, only the last term of Eq. (VII.3) survives. This comes from the facts that $\langle Q\rangle_{\Gamma_j} = 0$ and $\langle Q\Gamma\rangle_{\Gamma_j} = 0$. On the other hand, for a localized state built as flat superposition of states in a single band $\overline{|\psi_j\rangle}$, Eq. (VII.3) gives 0. This comes from the facts that $\oint dk\partial_k E_+\langle Q\rangle_{\psi_j} = sign(j)\oint dk\partial_k E_+ = 0$, $\langle Q\Gamma\rangle_{\psi_j} = 0$ and $\langle\Gamma\rangle_{\psi_j} = 0$.

Mean displacement in $\mathcal{D} > 2$

For $\mathcal{D} > 2$, the mean displacement at time t, starting from a generic localized state $\overline{|\Psi\rangle}$ reads:

$$\langle \hat{m}(t)\rangle_{\overline{\Psi}} = \tag{VII.5}$$
$$\sum_{j=1}^{\mathcal{D}/2} \oint \frac{\mathrm{d}k}{2\pi} \Big\{ t\partial_k E_j \langle Q_j\rangle_\Psi + \mathcal{S}_j \sin(2tE_j)\langle iQ_j\Gamma_j\rangle_\Psi - \mathcal{S}_j[1-\cos(2tE_j)]\langle\Gamma_j\rangle_\Psi \Big\}$$
$$+ \sum_{j,j'=\pm1,\ldots,\mathcal{D}/2 \text{ and } |j|\neq|j'|} \oint \frac{\mathrm{d}k}{2\pi} i\langle\psi_j|\psi'_{j'}\rangle\langle\Psi|\psi_j\rangle\langle\psi_{j'}|\Psi\rangle e^{it(E_j-E_{j'})}.$$

It can be shown that the terms arising from the second summation give rise to a purely real number, in agreement with the fact that the result is the expectation value of a Hermitian operator.

Noting that $Q_j\Gamma_j = |\psi_j\rangle\langle\psi_{-j}| - |\psi_{-j}\rangle\langle\psi_j|$, it is easy to see that the states $\overline{|\psi_j\rangle}$ are again stationary, as expected. On the other hand, for a chiral localized state $\overline{|\Gamma_j\rangle}$, Eq. (VII.5) gives:

$$\langle \hat{m}(t)\rangle_{\overline{\Gamma_j}} = -\mathrm{sgn}(j) \oint \frac{\mathrm{d}k}{2\pi} \mathcal{S}_j[1-\cos(2tE_j)], \tag{VII.6}$$

which proves Eq. III.9:

$$\sum_{j=1}^{\mathcal{D}/2} \langle \hat{m}(t)\rangle_{\overline{\Gamma_j}} = \sum_{j=1}^{\mathcal{D}/2} \langle \Gamma\cdot\hat{m}(t)\rangle_{\overline{\Gamma_j}} = -\sum_{j=1}^{\mathcal{D}/2} \oint \frac{\mathrm{d}k}{2\pi} \mathcal{S}_j[1-\cos(2tE_j)], \tag{VII.7}$$

VII.1.2 Mean chiral displacement

In terms of projectors on energy eigenstates, the mean chiral displacement of a generic localized state $\overline{|\Psi\rangle}$ reads:

$$\widehat{\langle\Gamma m(t)\rangle}_{\overline{\Psi}} = \oint \frac{\mathrm{d}k}{2\pi} \langle\Psi|U^{-t}\Gamma(i\partial_k)U^t|\Psi\rangle. \tag{VII.8}$$

We have

$$P_j[U^{-t}\Gamma\partial_k U^t]P_{j'} = \tag{VII.9}$$
$$\delta_{jj'}\left[P_j\Gamma\partial_k\frac{e^{i2tE_j}}{2} + e^{i2tE_j}|\psi_j\rangle\langle\psi'_{-j}|\right] + e^{it(E_j-E_{j'})}|\psi_j\rangle\langle\psi_{-j}|\psi'_{j'}\rangle\langle\psi_{j'}| =$$
$$= \delta_{jj'}\left[P_j\Gamma\partial_k\frac{e^{i2tE_j}}{2} + e^{i2tE_j}|\psi_j\rangle\langle\psi'_{-j}|\right] - e^{it(E_j-E_{j'})}|\psi_j\rangle\langle\psi'_{-j}|P_{j'}.$$

Mean chiral displacement in $\mathcal{D}=2$

For $\mathcal{D}=2$, the mean chiral displacement at time t, starting from a generic localized state $\overline{|\Psi\rangle}$ reads:

$$\widehat{\langle\Gamma m(t)\rangle}_{\overline{\Psi}} = \tag{VII.10}$$
$$\oint\frac{\mathrm{d}k}{2\pi}\Big\{\mathcal{S}[1-\cos(2tE_+)]\,\langle\mathbb{I}\rangle_\Psi + \frac{1}{2}\partial_k\left[\langle\Gamma\rangle_\Psi\cos(2tE_+) + \langle iQ\Gamma\rangle_\Psi\sin(2tE_+)\right]\Big\} =$$
$$= \oint\frac{\mathrm{d}k}{2\pi}\mathcal{S}[1-\cos(2tE_+)] = \oint\frac{\mathrm{d}k}{2\pi}\mathcal{S}\frac{\sin^2(tE_+)}{2} = \oint\frac{\mathrm{d}k}{2\pi}\sin^2(tE_+)(\mathbf{n}\times\partial_k\mathbf{n}).$$

This expression coincides with the one given in Ref. [71].

Mean chiral displacement in $\mathcal{D}>2$

Let us now define the projector on the subspace of chiral-partner eigenstates,

$$R_j = P_j + P_{-j}, \qquad \text{so that } \sum_{j=1}^{\mathcal{D}/2} R_j = \mathbb{I}. \tag{VII.11}$$

When $\mathcal{D} > 2$, we find that Eq. (VII.9) multiplied by i gives the sum of two terms, a term A which acts in the subspace of chiral partner states ($|j| = |j'|$) and a term B which acts in the subspace of the states with

$|j| \neq |j'|$.

$$A = \sum_{j=1}^{\mathcal{D}/2} \mathcal{S}_j[1-\cos(2tE_j)]R_j + iR_j\Gamma\partial_k\left[\frac{\cos(2tE_j)}{2}\right] - Q_j\Gamma\partial_k\left[\frac{\sin(2tE_j)}{2}\right] \tag{VII.12}$$

$$- iQ_j\mathcal{S}_j\sin(2tE_j) =$$
$$= \sum_{j=1}^{\mathcal{D}/2} \mathcal{S}_j[1-\cos(2tE_j)]R_j + \partial_k\left[i\Gamma_j\frac{\cos(2tE_j)}{2} - Q_j\Gamma\frac{\sin(2tE_j)}{2}\right],$$

where we have used the facts that $R_j\Gamma = \Gamma_j$, $\partial_k\Gamma = 0$ and $iQ_jS_j = \partial_k(Q_j\Gamma)/2$. And

$$B = \sum_{j,j'=\pm1,\ldots,\mathcal{D}/2 \text{ and } |j|\neq|j'|} i\langle\psi_{-j}|\psi'_{j'}\rangle|\psi_j\rangle\langle\psi_{j'}|e^{it(E_j-E_{j'})}. \tag{VII.13}$$

The term B has no diagonal term between chiral partners, and is purely oscillatory, so for generic E_j and $E_{j'}$ it will average to zero in the long time limit. Once integrated over the whole Brillouin zone the total derivative contained in A vanishes, so that the final result is

$$\langle\widehat{\Gamma m}(t)\rangle_{\overline{\Psi}} = \oint\frac{\mathrm{d}k}{2\pi}\left\langle B + \sum_{j=1}^{\mathcal{D}/2}\mathcal{S}_j[1-\cos(2tE_j)]R_j\right\rangle_{\Psi}. \tag{VII.14}$$

For the states $\overline{|\psi_j\rangle}$ and $\overline{|\Gamma_j\rangle}$, we have that $\langle B\rangle_{\psi_j} = \langle B\rangle_{\Gamma_j} = 0$ and $\langle R_j\rangle_{\psi'_j} = \langle R_j\rangle_{\Gamma'_j} = \delta_{jj'}$. This proves Eq. (III.10):

$$\sum_{j=1}^{\mathcal{D}/2}\langle\widehat{\Gamma m}(t)\rangle_{\overline{\Gamma_j}} = \sum_{j=1}^{\mathcal{D}/2}\langle\widehat{\Gamma m}(t)\rangle_{\overline{\Psi_j}} = \oint\frac{\mathrm{d}k}{2\pi}\sum_{j=1}^{\mathcal{D}/2}\mathcal{S}_j[1-\cos(2tE_j)]. \tag{VII.15}$$

The mean chiral displacement of a generic localized state, with support on all bands, in the long time-limit would instead be given by:

$$\lim_{t\to\infty}\langle\widehat{\Gamma m}(t)\rangle_{\overline{\Psi}} = \oint\frac{\mathrm{d}k}{2\pi}\sum_{j=1}^{\mathcal{D}/2}\mathcal{S}_j\langle R_j\rangle_{\Psi}, \tag{VII.16}$$

which, differently from the case $\mathcal{D} = 2$, is not a multiple of the winding number.

VII.1.3 Eigensystem of the SSH$_4$ model

Given a generic block anti-diagonal matrix $M = \begin{pmatrix} 0 & M_{12} \\ M_{21} & 0 \end{pmatrix}$, we have $M^2 = \begin{pmatrix} M_{12}M_{21} & 0 \\ 0 & M_{21}M_{12} \end{pmatrix}$. The eigenvalues of M therefore are the square roots of the eigenvalues of $\hat{M} = M_{12}M_{21}$. Thus, if we start from the SSH$_4$ Hamiltonian written in its completely off-diagonal form (in the canonical chiral eigenbasis), we have $H^2 = \begin{pmatrix} \hat{h} & 0 \\ 0 & \tilde{h} \end{pmatrix}$, with

$$\hat{h} = h^\dagger.h = \begin{pmatrix} a^2 + d^2 & ab + cde^{-ik} \\ ab + cde^{ik} & b^2 + c^2 \end{pmatrix}, \tag{VII.17}$$

and $\tilde{h} = h.h^\dagger$. If we denote by λ_1^2 and λ_2^2 the two eigenvalues of $\hat{h}$, the eigenvalues of the Hamiltonian are simply given by their square roots:

$$\lambda_{\pm 1} = \pm\lambda_1 = \pm\sqrt{\frac{T}{2} - \sqrt{\frac{T^2}{4} - \hat{D}}}, \qquad \lambda_{\pm 2} = \pm\lambda_2 = \pm\sqrt{\frac{T}{2} + \sqrt{\frac{T^2}{4} - \hat{D}}}, \tag{VII.18}$$

where $T = a^2 + b^2 + c^2 + d^2$ and $\hat{D} = a^2c^2 + b^2d^2 - 2abcd\cos(k)$ are respectively the trace and determinant of $\hat{h}$, and $|\lambda_{\pm 1}| < |\lambda_{\pm 2}|$. The topological phase transition of the SSH$_4$ model takes place when $ac = bd$ and $k = 0$, where $\lambda_{\pm 1} = 0$.

In order to find the eigenvectors of H, let us first consider the eigenvectors of H^2. Provided that $e^{ik} \neq -ab/cd$, we have $H^2|\hat{h}_l\rangle = \lambda_l^2|\hat{h}_l\rangle$ (for

$l = 1, 2$) with:

$$|\hat{h}_1\rangle = \frac{1}{\sqrt{\langle\hat{h}_1|\hat{h}_1\rangle}} \begin{pmatrix} \lambda_1^2 - (b^2 + c^2) \\ ab + cde^{ik} \\ 0 \\ 0 \end{pmatrix}, \qquad |\hat{h}_2\rangle = \frac{1}{\sqrt{\langle\hat{h}_2|\hat{h}_2\rangle}} \begin{pmatrix} \lambda_2^2 - (b^2 + c^2) \\ ab + cde^{ik} \\ 0 \\ 0 \end{pmatrix}. \tag{VII.19}$$

Similarly, provided that $e^{ik} \neq -bc/ad$, we have $H^2|\tilde{h}_l\rangle = \lambda_l^2|\tilde{h}_l\rangle$, with:

$$|\tilde{h}_1\rangle = \frac{1}{\sqrt{\langle\tilde{h}_1|\tilde{h}_1\rangle}} \begin{pmatrix} 0 \\ 0 \\ \lambda_1^2 - (c^2 + d^2) \\ bc + ade^{ik} \end{pmatrix}, \qquad |\tilde{h}_2\rangle = \frac{1}{\sqrt{\langle\tilde{h}_2|\tilde{h}_2\rangle}} \begin{pmatrix} 0 \\ 0 \\ \lambda_2^2 - (c^2 + d^2) \\ bc + ade^{ik} \end{pmatrix}. \tag{VII.20}$$

It is obvious that these will also be eigenvectors of Γ.

The eigenvectors of the Hamiltonian, $|\psi_{\pm l}\rangle$ are also eigenvectors of H^2, with eigenvalue λ_l^2. Therefore, for each value of l, we may write them as a normalized superposition of the two eigenvectors of H^2 with eigenvalue λ_l^2:

$$|\psi_{\pm l}\rangle = \hat{\alpha}_{\pm l}|\hat{h}_l\rangle + \tilde{\alpha}_{\pm l}|\tilde{h}_l\rangle. \tag{VII.21}$$

In particular, chiral symmetry imposes that energy eigenstates have equal support on both sublattices, i.e., $|\hat{\alpha}_{\pm l}| = |\tilde{\alpha}_{\pm l}| = 1/\sqrt{2}$. Then, with an appropriate choice of phases, we can write them as:

$$|\psi_{\pm l}\rangle = \frac{|\hat{h}_l\rangle \pm e^{i\phi_l}|\tilde{h}_l\rangle}{\sqrt{2}}. \tag{VII.22}$$

The phase ϕ_l needs to be fixed imposing that $|\psi_{\pm l}\rangle$ is an eigenstate of H with positive/negative energy. This may be done using the first line of the matrix equality $H|\psi_{+l}\rangle = +\lambda_l|\psi_{+l}\rangle$, which yields:

$$e^{i\phi_l} = \frac{\lambda_l|\hat{h}_l\rangle_1}{a|\tilde{h}_l\rangle_3 + de^{-ik}|\tilde{h}_l\rangle_4}, \tag{VII.23}$$

where $|\psi\rangle_n$ indicates the n^{th} component of the vector $|\psi\rangle$. Note finally that, upon sending $k \to -k$, the eigenstates of H satisfy

$$|\psi_{\pm l}(-k)\rangle = |\psi_{\pm l}(k)\rangle^*, \tag{VII.24}$$

which tells us that the Hamiltonian is time-reversal symmetric. Now we can explicitly build the Q-matrix in the canonical chiral eigenbasis, it reads:

$$Q = \sum_{l=1,2} e^{i\phi_l}|\tilde{h}_l\rangle\langle\hat{h}_l| + e^{-i\phi_l}|\hat{h}_l\rangle\langle\tilde{h}_l| = \sum_{1\leq r,s,t\leq 4} |\Gamma_r\rangle M_{rs}\Gamma_{ss}(M^\dagger)_{st}\langle\Gamma_t|, \tag{VII.25}$$

with $M_{rs} = \langle\Gamma_r|\psi_s\rangle$ the unitary matrix for the change of basis between the canonical-chiral and energy eigenstates. Computing the determinant of q, the lower-left block of Q, we see that $\arg[\mathrm{Det}(q)] = -i\log\left(\frac{ac-bde^{ik}}{|ac-bde^{ik}|}\right) = \arg[\mathrm{Det}(h)]$. The winding of the SSH_4 model may now be computed from Eq. (II.7), or equivalently from Eq. (II.10).

VII.2 Detection of the winding in disorderd systems

VII.2.1 Real-space definition of the Winding number

Here we compute the winding number within open boundary conditions using the "local topological marker" introduced by Bianco and Resta in Refs. [125, 126]. In particular we use the symmetrized version of the argument of the trace per volume appearing in Ref. [124] evaluated over the central part of the chain. Its explicit expression is given in Eq. (III.17) in terms of the operator M:

$$M = \frac{Q_{BA}XQ_{AB} - Q_{BA}Q_{AB}X - Q_{AB}XQ_{BA} + Q_{AB}Q_{BA}X}{2}. \tag{VII.26}$$

The winding number is given by $\nu(0) = \sum_{a=A,B}\langle 0_a|M|0_a\rangle$ where $|0_a\rangle$ is a state completely localized on the central cell of the chain, either in a site $a = A$ or in a site $a = B$. α_{ai} are its projections on the eigensystem of the

Hamiltonian $\{|\phi_i\rangle\}$, with $i = -N, ..N$ and energies $E_{-i} = -E_i$. Note that the Chiral symmetry implies that the states ϕ_i satisfy $|\phi_{-i}\rangle = \Gamma|\phi_i\rangle$.

In order to compute the scalar product $\langle 0_a|M|0_a\rangle$ we use the following properties:

- The state is localized in 0, then $X|0_a\rangle = 0$.
- $\Gamma_B Q = Q\Gamma_A$. With open boundary conditions, this equality does not hold for zero-energy edge states, but here we are only interested in a bulk state, like $|0\rangle$, which has negligible overlap with the edge states.
- Γ_A and Γ_B are projectors, so that, e.g., $\Gamma_A\Gamma_A = \Gamma_A$.
- The chiral operator is local (i.e., diagonal in the position basis), so that $[X, \Gamma_A] = [X, \Gamma_B] = 0$.

These gives:

$$\langle 0_a|M|0_a\rangle = \frac{1}{2}\langle 0|Q_{BA}XQ_{AB} - Q_{BA}Q_{AB}X - Q_{AB}XQ_{BA} + Q_{AB}Q_{BA}X|0\rangle \tag{VII.27}$$

$$\begin{aligned} &= \frac{1}{2}\langle 0_a|Q_{BA}XQ_{AB} - Q_{AB}XQ_{BA}|0_a\rangle \\ &= \frac{1}{2}\langle 0_a|Q(\Gamma_A)^4XQ - Q(\Gamma_B)^4XQ|0_a\rangle \\ &= \frac{1}{2}\langle 0_a|Q\Gamma XQ|0_a\rangle. \end{aligned}$$

Finally, using $Q = \mathbb{I} - 2P_-$, we arrive to Eq. (III.19)

$$
\begin{aligned}
\nu(0) &= \sum_{a=A,B} \langle 0_a|M|0_a\rangle \qquad \text{(VII.28)}\\
&= \sum_a \langle 0_a| \left[\frac{1}{2}\Gamma X - P_-\Gamma X - \Gamma X P_- + 2P_-\Gamma X P_-\right] |0_a\rangle \\
&= 2\sum_a \langle 0_a|P_-\Gamma X P_-|0_a\rangle \\
&= 2\sum_a \left[\sum_{i<0} |\alpha_{ai}|^2 \langle\phi_i|\Gamma X|\phi_i\rangle + \sum_{i,j<0;i\neq j} \alpha^*_{ai}\alpha_{aj}\langle\phi_i|\Gamma X|\phi_j\rangle\right] \\
&= \sum_a \left[\sum_{i} |\alpha_{ai}|^2 \langle\phi_i|\Gamma X|\phi_i\rangle + \sum_{i,j<0;i\neq j} \alpha^*_{ai}\alpha_{aj}\langle\phi_i|\Gamma X|\phi_j\rangle \right.\\
&\left. + \sum_{i,j>0;i\neq j} \alpha^*_{ai}\alpha_{aj}\langle\phi_i|\Gamma X|\phi_j\rangle\right].
\end{aligned}
$$

Bibliography

[1] M. Nakahara, *Geometry, topology and physics*. CRC Press, 2003.

[2] K.-H. Hoffmann and Q. Tang, *Ginzburg-Landau phase transition theory and superconductivity*, vol. 134. Birkhäuser, 2012.

[3] C.-K. Chiu, J. C. Y. Teo, A. P. Schnyder, and S. Ryu, "Classification of topological quantum matter with symmetries," *Rev. Mod. Phys.*, vol. 88, p. 035005, 2016.

[4] J. M. Kosterlitz and D. J. Thouless, "Ordering, metastability and phase transitions in two-dimensional systems," *J. Phys. C: Solid State Phys.*, vol. 6, p. 1181, 1973.

[5] J. M. Kosterlitz, "Nobel lecture: Topological defects and phase transitions," *Rev. Mod. Phys.*, vol. 89, p. 040501, 2017.

[6] F. D. M. Haldane, "Nobel lecture: Topological quantum matter," *Rev. Mod. Phys.*, vol. 89, p. 040502, 2017.

[7] K. von Klitzing, "The quantized hall effect," *Rev. Mod. Phys.*, vol. 58, p. 519, 1986.

[8] D. J. Thouless, M. Kohmoto, M. P. Nightingale, and M. den Nijs, "Quantized hall conductance in a two-dimensional periodic potential," *Phys. Rev. Lett.*, vol. 49, p. 405, 1982.

[9] D. R. Hofstadter, "Energy levels and wave functions of bloch electrons in rational and irrational magnetic fields," *Phys. Rev. B*, vol. 14, p. 2239, 1976.

[10] D. Xiao, M.-C. Chang, and Q. Niu, "Berry phase effects on electronic properties," *Rev. Mod. Phys.*, vol. 82, p. 1959, 2010.

[11] R. B. Laughlin, "Quantized hall conductivity in two dimensions," *Phys. Rev. B*, vol. 23, p. 5632, 1981.

[12] B. I. Halperin, "Quantized hall conductance, current-carrying edge states, and the existence of extended states in a two-dimensional disordered potential," *Phys. Rev. B*, vol. 25, p. 2185, 1982.

[13] D. J. Thouless, "Quantization of particle transport," *Phys. Rev. B*, vol. 27, p. 6083, 1983.

[14] M. Z. Hasan and C. L. Kane, "Colloquium," *Rev. Mod. Phys.*, vol. 82, p. 3045, 2010.

[15] F. D. M. Haldane, "Model for a quantum hall effect without landau levels: Condensed-matter realization of the "parity anomaly"," *Phys. Rev. Lett.*, vol. 61, p. 2015, 1988.

[16] C. L. Kane and E. J. Mele, "Quantum spin hall effect in graphene," *Phys. Rev. Lett.*, vol. 95, p. 226801, 2005.

[17] C. L. Kane and E. J. Mele, "Z_2 topological order and the quantum spin hall effect," *Phys. Rev. Lett.*, vol. 95, p. 146802, 2005.

[18] B. A. Bernevig, T. L. Hughes, and S.-C. Zhang, "Quantum spin hall effect and topological phase transition in hgte quantum wells," *Science*, vol. 314, p. 1757, 2006.

[19] M. König, C. Wiedmann, S.and Brüne, A. Roth, H. Buhmann, L. W. Molenkamp, X. Qi, and S. Zhang, "Quantum spin hall insulator state in hgte quantum wells," *Science*, vol. 318, p. 766, 2007.

[20] C. Gross and I. Bloch, "Quantum simulations with ultracold atoms in optical lattices," *Science*, vol. 357, p. 995, 2017.

[21] A. Aspuru-Guzik and P. Walther, "Photonic quantum simulators," *Nat. Phys.*, vol. 8, p. 285, 2012.

[22] N. Goldman, J. C. Budich, and P. Zoller, "Topological quantum matter with ultracold gases in optical lattices," *Nat. Phys.*, vol. 12, p. 639, 2016.

[23] N. Cooper, J. Dalibard, and I. Spielman, "Topological bands for ultracold atoms," *arXiv preprint arXiv:1803.00249*, 2018.

[24] T. Ozawa, H. M. Price, A. Amo, N. Goldman, M. Hafezi, L. Lu, M. Rechtsman, D. Schuster, J. Simon, O. Zilberberg, *et al.*, "Topological photonics," *arXiv preprint arXiv:1802.04173*, 2018.

[25] M. Greiner, O. Mandel, T. Esslinger, T. W. Hänsch, and I. Bloch, "Quantum phase transition from a superfluid to a mott insulator in a gas of ultracold atoms," *Nature*, vol. 415, p. 39, 2002.

[26] S.-C. Zhang and J. Hu, "A four-dimensional generalization of the quantum hall effect," *Science*, vol. 294, p. 823, 2001.

[27] M. Lohse, C. Schweizer, H. M. Price, O. Zilberberg, and I. Bloch, "Exploring 4d quantum hall physics with a 2d topological charge pump," *Nature*, vol. 553, p. 55, 2018.

[28] S. Sugawa, F. Salces-Carcoba, A. R. Perry, Y. Yue, and I. B. Spielman, "Second chern number of a quantum-simulated non-abelian yang monopole," *Science*, vol. 360, p. 1429, 2018.

[29] O. Zilberberg, S. Huang, J. Guglielmon, M. Wang, K. Chen, Y. E. Kraus, and M. C. Rechtsman, "Photonic topological boundary pumping as a probe of 4d quantum hall physics," *Nature*, vol. 553, p. 59, 2018.

[30] M. Aidelsburger, M. Atala, S. Nascimbène, S. Trotzky, Y.-A. Chen, and I. Bloch, "Experimental realization of strong effective magnetic fields in an optical lattice," *Phys. Rev. Lett.*, vol. 107, p. 255301, 2011.

[31] H. M. Price and N. R. Cooper, "Mapping the berry curvature from semiclassical dynamics in optical lattices," *Phys. Rev. A*, vol. 85, p. 033620, 2012.

[32] M. Aidelsburger, M. Atala, M. Lohse, J. T. Barreiro, B. Paredes, and I. Bloch, "Realization of the hofstadter hamiltonian with ultracold atoms in optical lattices," *Phys. Rev. Lett.*, vol. 111, p. 185301, 2013.

[33] H. Miyake, G. A. Siviloglou, C. J. Kennedy, W. C. Burton, and W. Ketterle, "Realizing the harper hamiltonian with laser-assisted tunneling in optical lattices," *Phys. Rev. Lett.*, vol. 111, p. 185302, 2013.

[34] G. Jotzu, M. Messer, R. Desbuquois, M. Lebrat, T. Uehlinger, D. Greif, and T. Esslinger, "Experimental realization of the topological haldane model with ultracold fermions," *Nature*, vol. 515, p. 237, 2014.

[35] M. Lohse, C. Schweizer, O. Zilberberg, M. Aidelsburger, and I. Bloch, "A thouless quantum pump with ultracold bosonic atoms in an optical superlattice," *Nat. Phys.*, vol. 12, p. 350, 2015.

[36] M. Mancini, G. Pagano, G. Cappellini, L. Livi, M. Rider, J. Catani, C. Sias, P. Zoller, M. Inguscio, M. Dalmonte, and L. Fallani, "Observation of chiral edge states with neutral fermions in synthetic hall ribbons," *Science*, vol. 349, p. 1510, 2015.

[37] B. K. Stuhl, H.-I. Lu, L. M. Aycock, D. Genkina, and I. B. Spielman, "Visualizing edge states with an atomic bose gas in the quantum hall regime," *Science*, vol. 349, p. 1514, 2015.

[38] M. Aidelsburger, M. Lohse, C. Schweizer, M. Atala, J. T. Barreiro, S. Nascimbène, N. R. Cooper, I. Bloch, and N. Goldman, "Revealing

the topology of hofstadter bands with ultracold bosonic atoms," *Nat. Phys.*, vol. 11, p. 162, 2015.

[39] M. Leder, C. Grossert, L. Sitta, M. Genske, A. Rosch, and M. Weitz, "Real-space imaging of a topologically protected edge state with ultracold atoms in an amplitude-chirped optical lattice," *Nat. Commun.*, vol. 7, p. 13112, 2016.

[40] D. Jaksch and P. Zoller, "Creation of effective magnetic fields in optical lattices: the hofstadter butterfly for cold neutral atoms," *New J. Phys.*, vol. 5, p. 56, 2003.

[41] N. Goldman and J. Dalibard, "Periodically driven quantum systems: Effective hamiltonians and engineered gauge fields," *Phys. Rev. X*, vol. 4, p. 031027, 2014.

[42] T. Kitagawa, E. Berg, M. Rudner, and E. Demler, "Topological characterization of periodically driven quantum systems," *Phys. Rev. B*, vol. 82, p. 235114, 2010.

[43] J. K. Asbóth, B. Tarasinski, and P. Delplace, "Chiral symmetry and bulk-boundary correspondence in periodically driven one-dimensional systems," *Phys. Rev. B*, vol. 90, p. 125143, 2014.

[44] M. S. Rudner, N. H. Lindner, E. Berg, and M. Levin, "Anomalous edge states and the bulk-edge correspondence for periodically driven two-dimensional systems," *Phys. Rev. X*, vol. 3, p. 031005, 2013.

[45] F. Nathan and M. S. Rudner, "Topological singularities and the general classification of floquet-bloch systems," *New J. Phys.*, vol. 17, p. 125014, 2015.

[46] L. Jiang, T. Kitagawa, J. Alicea, A. R. Akhmerov, D. Pekker, G. Refael, J. I. Cirac, E. Demler, M. D. Lukin, and P. Zoller, "Majorana fermions in equilibrium and in driven cold-atom quantum wires," *Phys. Rev. Lett.*, vol. 106, p. 220402, 2011.

[47] A. Celi, P. Massignan, J. Ruseckas, N. Goldman, I. B. Spielman, G. Juzeliūnas, and M. Lewenstein, "Synthetic gauge fields in synthetic dimensions," *Phys. Rev. Lett.*, vol. 112, p. 043001, 2014.

[48] E. J. Meier, F. A. An, and B. Gadway, "Atom-optics simulator of lattice transport phenomena," *Phys. Rev. A*, vol. 93, p. 051602, 2016.

[49] E. J. Meier, F. A. An, and B. Gadway, "Observation of the topological soliton state in the su–schrieffer–heeger model," *Nat. Commun.*, vol. 7, p. 13986, 2016.

[50] E. J. Meier, F. A. An, A. Dauphin, M. Maffei, P. Massignan, T. L. Hughes, and B. Gadway, "Observation of the topological anderson insulator in disordered atomic wires," *Science*, vol. 362, p. 929, 2018.

[51] M. C. Rechtsman, J. M. Zeuner, Y. Plotnik, Y. Lumer, D. Podolsky, F. Dreisow, S. Nolte, M. Segev, and A. Szameit, "Photonic floquet topological insulators," *Nature*, vol. 496, p. 196, 2013.

[52] B. E. Saleh, M. C. Teich, and B. E. Saleh, *Fundamentals of photonics*, vol. 22. Wiley New York, 1991.

[53] S. Raghu and F. D. M. Haldane, "Analogs of quantum-hall-effect edge states in photonic crystals," *Phys. Rev. A*, vol. 78, p. 033834, 2008.

[54] F. D. M. Haldane and S. Raghu, "Possible realization of directional optical waveguides in photonic crystals with broken time-reversal symmetry," *Phys. Rev. Lett.*, vol. 100, p. 013904, 2008.

[55] T. Ozawa, H. M. Price, N. Goldman, O. Zilberberg, and I. Carusotto, "Synthetic dimensions in integrated photonics: From optical isolation to four-dimensional quantum hall physics," *Phys. Rev. A*, vol. 93, p. 043827, 2016.

[56] Y. Aharonov, L. Davidovich, and N. Zagury, "Quantum random walks," *Phys. Rev. A*, vol. 48, p. 1687, 1993.

[57] A. Peruzzo, M. Lobino, J. C. F. Matthews, N. Matsuda, A. Politi, K. Poulios, X.-Q. Zhou, Y. Lahini, N. Ismail, K. Worhoff, Y. Bromberg, Y. Silberberg, M. G. Thompson, and J. L. OBrien, "Quantum Walks of Correlated Photons," *Science*, vol. 329, p. 1500, 2010.

[58] L. Sansoni, F. Sciarrino, G. Vallone, P. Mataloni, A. Crespi, R. Ramponi, and R. Osellame, "Two-Particle Bosonic-Fermionic Quantum Walk via Integrated Photonics," *Physical Review Letters*, vol. 108, p. 010502, 2012.

[59] M. A. Broome, A. Fedrizzi, B. P. Lanyon, I. Kassal, A. Aspuru-Guzik, and A. G. White, "Discrete single-photon quantum walks with tunable decoherence," *Phys. Rev. Lett.*, vol. 104, p. 153602, 2010.

[60] A. Schreiber, K. N. Cassemiro, V. Potoček, A. Gábris, I. Jex, and C. Silberhorn, "Decoherence and disorder in quantum walks: From ballistic spread to localization," *Phys. Rev. Lett.*, vol. 106, p. 180403, 2011.

[61] A. Crespi, R. Osellame, R. Ramponi, V. Giovannetti, R. Fazio, L. Sansoni, F. D. Nicola, F. Sciarrino, and P. Mataloni, "Anderson localization of entangled photons in an integrated quantum walk," *Nat. Photonics*, vol. 7, p. 322, 2013.

[62] M. Genske, W. Alt, A. Steffen, A. H. Werner, R. F. Werner, D. Meschede, and A. Alberti, "Electric quantum walks with individual atoms," *Phys. Rev. Lett.*, vol. 110, p. 190601, 2013.

[63] M. Atala, M. Aidelsburger, J. T. Barreiro, D. A. Abanin, T. Kitagawa, E. Demler, and I. Bloch, "Direct measurement of the zak phase in topological bloch bands," *Nat. Phys.*, vol. 9, p. 795, 2013.

[64] D. A. Abanin, T. Kitagawa, I. Bloch, and E. Demler, "Interferometric approach to measuring band topology in 2d optical lattices," *Phys. Rev. Lett.*, vol. 110, p. 165304, 2013.

[65] V. V. Ramasesh, E. Flurin, M. Rudner, I. Siddiqi, and N. Y. Yao, "Direct probe of topological invariants using bloch oscillating quantum walks," *Phys. Rev. Lett.*, vol. 118, p. 130501, 2017.

[66] E. Flurin, V. V. Ramasesh, S. Hacohen-Gourgy, L. S. Martin, N. Y. Yao, and I. Siddiqi, "Observing topological invariants using quantum walks in superconducting circuits," *Phys. Rev. X*, vol. 7, p. 031023, 2017.

[67] T. Kitagawa, M. S. Rudner, E. Berg, and E. Demler, "Exploring topological phases with quantum walks," *Phys. Rev. A*, vol. 82, p. 033429, 2010.

[68] S. Barkhofen, T. Nitsche, F. Elster, L. Lorz, A. Gábris, I. Jex, and C. Silberhorn, "Measuring topological invariants in disordered discrete-time quantum walks," *Phys. Rev. A*, vol. 96, p. 033846, 2017.

[69] F. Cardano, F. Massa, H. Qassim, E. Karimi, S. Slussarenko, D. Paparo, C. de Lisio, F. Sciarrino, E. Santamato, R. W. Boyd, and L. Marrucci, "Quantum walks and wavepacket dynamics on a lattice with twisted photons," *Sci. Adv.*, vol. 1, 2015.

[70] F. Cardano, M. Maffei, F. Massa, B. Piccirillo, C. D. Lisio, G. D. Filippis, V. Cataudella, E. Santamato, and L. Marrucci, "Statistical moments of quantum-walk dynamics reveal topological quantum transitions," *Nat. Commun.*, vol. 7, p. 11439, 2016.

[71] F. Cardano, A. D'Errico, A. Dauphin, M. Maffei, B. Piccirillo, C. de Lisio, G. De Filippis, V. Cataudella, E. Santamato, L. Marrucci, M. Lewenstein, and P. Massignan, "Detection of zak phases and topological invariants in a chiral quantum walk of twisted photons," *Nat. Commun.*, vol. 8, p. 15516, 2017.

[72] L. Xiao, X. Zhan, Z. Bian, K. Wang, X. Zhang, X. Wang, J. Li, K. Mochizuki, D. Kim, N. Kawakami, *et al.*, "Observation of topo-

logical edge states in parity–time-symmetric quantum walks," *Nat. Phys.*, vol. 13, p. 1117, 2017.

[73] X. Zhan, L. Xiao, Z. Bian, K. Wang, X. Qiu, B. C. Sanders, W. Yi, and P. Xue, "Detecting topological invariants in nonunitary discrete-time quantum walks," *Phys. Rev. Lett.*, vol. 119, p. 130501, 2017.

[74] X. Wang, L. Xiao, X. Qiu, K. Wang, W. Yi, and P. Xue, "Detecting topological invariants and revealing topological phase transitions in discrete-time photonic quantum walks," *Phys. Rev. A*, vol. 98, p. 013835, 2018.

[75] J. K. Asbóth and H. Obuse, "Bulk-boundary correspondence for chiral symmetric quantum walks," *Phys. Rev. B*, vol. 88, p. 121406, 2013.

[76] T. Kitagawa, M. a. Broome, A. Fedrizzi, M. S. Rudner, E. Berg, I. Kassal, A. Aspuru-Guzik, E. Demler, and A. G. White, "Observation of topologically protected bound states in photonic quantum walks," *Nat. Commun.*, vol. 3, p. 882, 2012.

[77] K. Poulios, R. Keil, D. Fry, J. D. A. Meinecke, J. C. F. Matthews, A. Politi, M. Lobino, M. Gräfe, M. Heinrich, S. Nolte, A. Szameit, and J. L. O'Brien, "Quantum Walks of Correlated Photon Pairs in Two-Dimensional Waveguide Arrays," *Physical Review Letters*, vol. 112, p. 143604, 2014.

[78] A. Schreiber, A. Gábris, P. P. Rohde, K. Laiho, M. Štefaňák, V. Potoček, C. Hamilton, I. Jex, and C. Silberhorn, "A 2d quantum walk simulation of two-particle dynamics," *Science*, 2012.

[79] Y.-C. Jeong, C. Di Franco, H.-T. Lim, M. Kim, and Y.-H. Kim, "Experimental realization of a delayed-choice quantum walk," *Nat. Commun.*, vol. 4, p. 2471, 2013.

[80] A. D'Errico, F. Cardano, M. Maffei, A. Dauphin, R. Barboza, C. Esposito, B. Piccirillo, M. Lewenstein, P. Massignan, and L. Marrucci,

"Two–dimensional topological quantum walks in the momentum space of structured light," *arXiv preprint arXiv:1811.04001*, 2018.

[81] L. Mazza, M. Aidelsburger, H.-H. Tu, N. Goldman, and M. Burrello, "Methods for detecting charge fractionalization and winding numbers in an interacting fermionic ladder," *New J. Phys.*, vol. 17, p. 105001, 2015.

[82] D. S. Simon, C. A. Fitzpatrick, S. Osawa, and A. V. Sergienko, "Quantum simulation of topologically protected states using directionally unbiased linear-optical multiports," *Phys. Rev. A*, vol. 96, p. 013858, 2017.

[83] M. Maffei, A. Dauphin, F. Cardano, M. Lewenstein, and P. Massignan, "Topological characterization of chiral models through their long time dynamics," *New J. Phys.*, vol. 20, p. 013023, 2018.

[84] J. K. Asbóth, L. Oroszlány, and A. Pályi, *A Short Course on Topological Insulators*, vol. 919 of *Lecture Notes in Physics*. Springer International Publishing, 2016.

[85] M. S. Rudner and L. S. Levitov, "Topological transition in a non-hermitian quantum walk," *Phys. Rev. Lett.*, vol. 102, p. 1, 2009.

[86] J. M. Zeuner, M. C. Rechtsman, Y. Plotnik, Y. Lumer, S. Nolte, M. S. Rudner, M. Segev, and A. Szameit, "Observation of a topological transition in the bulk of a non-hermitian system," *Phys. Rev. Lett.*, vol. 115, p. 040402, 2015.

[87] T. Rakovszky, J. K. Asbóth, and A. Alberti, "Detecting topological invariants in chiral symmetric insulators via losses," *Phys. Rev. B*, vol. 95, p. 201407, 2017.

[88] J. Li, R.-L. Chu, J. K. Jain, and S.-Q. Shen, "Topological anderson insulator," *Phys. Rev. Lett.*, vol. 102, p. 136806, 2009.

[89] L. Allen, M. Padgett, and M. Babiker, vol. 39 of *Progress in Optics*. Elsevier, 1999.

[90] M. Padgett, J. Courtial, and L. Allen, "Light's orbital angular momentum," *Phys. Today*, vol. 57, p. 35, 2004.

[91] L. Marrucci, C. Manzo, and D. Paparo, "Optical spin-to-orbital angular momentum conversion in inhomogeneous anisotropic media," *Phys. Rev. Lett.*, vol. 96, p. 163905, 2006.

[92] H. Tang, X.-F. Lin, Z. Feng, J.-Y. Chen, J. Gao, K. Sun, C.-Y. Wang, P.-C. Lai, X.-Y. Xu, Y. Wang, L.-F. Qiao, A.-L. Yang, and X.-M. Jin, "Experimental two-dimensional quantum walk on a photonic chip," *Sci. Adv.*, vol. 4, 2018.

[93] B. Wang, T. Chen, and X. Zhang, "Experimental Observation of Topologically Protected Bound States with Vanishing Chern Numbers in a Two-Dimensional Quantum Walk," *Physical Review Letters*, vol. 121, p. 100501, 2018.

[94] C. Chen, X. Ding, J. Qin, Y. He, Y.-H. Luo, M.-C. Chen, C. Liu, X.-L. Wang, W.-J. Zhang, H. Li, L.-X. You, Z. Wang, D.-W. Wang, B. C. Sanders, C.-Y. Lu, and J.-W. Pan, "Observation of Topologically Protected Edge States in a Photonic Two-Dimensional Quantum Walk," *Physical Review Letters*, vol. 121, p. 100502, 2018.

[95] C. Cedzich, T. Rybár, A. H. Werner, A. Alberti, M. Genske, and R. F. Werner, "Propagation of quantum walks in electric fields," *Phys. Rev. Lett.*, vol. 111, p. 160601, 2013.

[96] L. A. Bru, M. Hinarejos, F. Silva, G. J. de Valcárcel, and E. Roldán, "Electric quantum walks in two dimensions," *Phys. Rev. A*, vol. 93, p. 1, 2015.

[97] P. Xue, H. Qin, B. Tang, and B. C. Sanders, "Observation of quasiperiodic dynamics in a one-dimensional quantum walk of single photons in space," *New J. Phys.*, vol. 16, p. 053009, 2014.

[98] C. Cedzich and R. F. Werner, "Revivals in quantum walks with a quasiperiodically-time-dependent coin," *Phys. Rev. A*, vol. 93, p. 032329, 2016.

[99] H. M. Price, O. Zilberberg, T. Ozawa, I. Carusotto, and N. Goldman, "Measurement of chern numbers through center-of-mass responses," *Phys. Rev. B*, vol. 93, p. 245113, 2016.

[100] W. P. Su, J. R. Schrieffer, and A. J. Heeger, "Solitons in polyacetylene," *Phys. Rev. Lett.*, vol. 42, p. 1698, 1979.

[101] I. Mondragon-Shem, T. L. Hughes, J. Song, and E. Prodan, "Topological criticality in the chiral-symmetric aiii class at strong disorder," *Phys. Rev. Lett.*, vol. 113, p. 046802, 2014.

[102] M. Berry, "Quantal phase factors accompanying adiabatic changes," *Proceedings of the Royal Society of London A: Mathematical, Physical and Engineering Sciences*, vol. 392, p. 45, 1984.

[103] A. Tonomura, N. Osakabe, T. Matsuda, T. Kawasaki, J. Endo, S. Yano, and H. Yamada, "Evidence for aharonov-bohm effect with magnetic field completely shielded from electron wave," *Phys. Rev. Lett.*, vol. 56, p. 792, 1986.

[104] J. Zak, "Berry's phase for energy bands in solids," *Phys. Rev. Lett.*, vol. 62, p. 2747, 1989.

[105] R. Resta, "Macroscopic polarization in crystalline dielectrics: the geometric phase approach," *Rev. Mod. Phys.*, vol. 66, p. 899, 1994.

[106] G. H. Wannier, "The structure of electronic excitation levels in insulating crystals," *Phys. Rev.*, vol. 52, p. 191, 1937.

[107] R. D. King-Smith and D. Vanderbilt, "Theory of polarization of crystalline solids," *Phys. Rev. B*, vol. 47, p. 1651, 1993.

[108] C. Beenakker and L. Kouwenhoven, "A road to reality with topological superconductors," *Nat. Phys.*, vol. 12, p. 618, 2016.

[109] M. Xiao, G. Ma, Z. Yang, P. Sheng, Z. Q. Zhang, and C. T. Chan, "Geometric phase and band inversion in periodic acoustic systems," *Nat. Phys.*, vol. 11, p. 240, 2015.

[110] V. Peano, C. Brendel, M. Schmidt, and F. Marquardt, "Topological phases of sound and light," *Phys. Rev. X*, vol. 5, p. 031011, 2015.

[111] Y.-G. Peng, C.-Z. Qin, D.-G. Zhao, Y.-X. Shen, X.-Y. Xu, M. Bao, H. Jia, and X.-F. Zhu, "Experimental demonstration of anomalous floquet topological insulator for sound," *Nat. Commun.*, vol. 7, p. 13368, 2016.

[112] P. G. Harper, "Single band motion of conduction electrons in a uniform magnetic field," *Proceedings of the Physical Society. Section A*, vol. 68, p. 874, 1955.

[113] M. Kohmoto, "Zero modes and the quantized hall conductance of the two-dimensional lattice in a magnetic field," *Phys. Rev. B*, vol. 39, p. 11943, 1989.

[114] W. G. H., "A result not dependent on rationality for bloch electrons in a magnetic field," *Phys. Status Solidi B*, vol. 88, p. 757, 1978.

[115] P. Streda, "Theory of quantised hall conductivity in two dimensions," *J. Phys. C: Solid State Phys.*, vol. 15, p. L717, 1982.

[116] Y. E. Kraus, Y. Lahini, Z. Ringel, M. Verbin, and O. Zilberberg, "Topological states and adiabatic pumping in quasicrystals," *Phys. Rev. Lett.*, vol. 109, p. 106402, 2012.

[117] E. Prodan, "Virtual topological insulators with real quantized physics," *Phys. Rev. B*, vol. 91, p. 245104, 2015.

[118] S. Aubry, "S. aubry and g. andré, ann. isr. phys. soc. 3, 133 (1980).," *Ann. Isr. Phys. Soc.*, vol. 3, p. 133, 1980.

[119] D. Levine and P. J. Steinhardt, "Quasicrystals: A new class of ordered structures," *Phys. Rev. Lett.*, vol. 53, p. 2477, 1984.

[120] Y. E. Kraus and O. Zilberberg, "Topological equivalence between the fibonacci quasicrystal and the harper model," *Phys. Rev. Lett.*, vol. 109, p. 116404, 2012.

[121] A. Altland, D. Bagrets, and A. Kamenev, "Topology versus anderson localization: Nonperturbative solutions in one dimension," *Phys. Rev. B*, vol. 91, p. 085429, 2015.

[122] H. Guo and S. Chen, "Kaleidoscope of symmetry-protected topological phases in one-dimensional periodically modulated lattices," *Phys. Rev. B*, vol. 91, p. 041402, 2015.

[123] P. St-Jean, V. Goblot, E. Galopin, A. Lemaître, T. Ozawa, L. Le Gratiet, I. Sagnes, J. Bloch, and A. Amo, "Lasing in topological edge states of a one-dimensional lattice," *Nat. Photonics*, vol. 11, p. 651, 2017.

[124] I. Mondragon-Shem, T. L. Hughes, J. Song, and E. Prodan, "Topological criticality in the chiral-symmetric aiii class at strong disorder," *Phys. Rev. Lett.*, vol. 113, p. 046802, 2014.

[125] R. Bianco and R. Resta, "Mapping topological order in coordinate space," *Phys. Rev. B*, vol. 84, p. 241106, 2011.

[126] R. Bianco and R. Resta, "Orbital magnetization as a local property," *Phys. Rev. Lett.*, vol. 110, p. 087202, 2013.

[127] P. W. Anderson, "Absence of diffusion in certain random lattices," *Phys. Rev.*, vol. 109, p. 1492, 1958.

[128] S. Stützer, Y. Plotnik, Y. Lumer, P. Titum, N. H. Lindner, M. Segev, M. C. Rechtsman, and A. Szameit, "Photonic topological anderson insulators," *Nature*, vol. 560, no. 7719, p. 461, 2018.

[129] C. W. Groth, M. Wimmer, A. R. Akhmerov, J. Tworzydło, and C. W. J. Beenakker, "Theory of the topological anderson insulator," *Phys. Rev. Lett.*, vol. 103, p. 196805, 2009.

[130] A. Altland, D. Bagrets, L. Fritz, A. Kamenev, and H. Schmiedt, "Quantum criticality of quasi-one-dimensional topological anderson insulators," *Phys. Rev. Lett.*, vol. 112, p. 206602, 2014.

[131] S. E. Venegas-Andraca, "Quantum walks: a comprehensive review," *Quantum Inf. Process.*, vol. 11, p. 1015, 2012.

[132] N. B. Lovett, S. Cooper, M. Everitt, M. Trevers, and V. Kendon, "Universal quantum computation using the discrete-time quantum walk," *Phys. Rev. A*, vol. 81, p. 042330, 2010.

[133] N. Shenvi, J. Kempe, and K. B. Whaley, "Quantum random-walk search algorithm," *Phys. Rev. A*, vol. 67, p. 052307, 2003.

[134] A. M. Childs and J. Goldstone, "Spatial search by quantum walk," *Phys. Rev. A*, vol. 70, p. 022314, 2004.

[135] J. K. Asbóth, "Symmetries, topological phases, and bound states in the one-dimensional quantum walk," *Phys. Rev. B*, vol. 86, p. 195414, 2012.

[136] L. J. Maczewsky, J. M. Zeuner, S. Nolte, and A. Szameit, "Observation of photonic anomalous floquet topological insulators," *Nat. Commun.*, vol. 8, p. 13756, 2017.

[137] M. A. Broome, A. Fedrizzi, S. Rahimi-Keshari, J. Dove, S. Aaronson, T. C. Ralph, and A. G. White, "Photonic boson sampling in a tunable circuit," *Science*, vol. 339, p. 794, 2013.

[138] C. Callias, "Axial anomalies and index theorems on open spaces," *Commun. Math. Phys.*, vol. 62, p. 213, 1978.

[139] H. He, M. E. J. Friese, N. R. Heckenberg, and H. Rubinsztein-Dunlop, "Direct observation of transfer of angular momentum to absorptive particles from a laser beam with a phase singularity," *Phys. Rev. Lett.*, vol. 75, p. 826, 1995.

[140] L. Allen, M. W. Beijersbergen, R. J. C. Spreeuw, and J. P. Woerdman, "Orbital angular momentum of light and the transformation of laguerre-gaussian laser modes," *Phys. Rev. A*, vol. 45, p. 8185, 1992.

[141] J. Leach, M. J. Padgett, S. M. Barnett, S. Franke-Arnold, and J. Courtial, "Measuring the orbital angular momentum of a single photon," *Phys. Rev. Lett.*, vol. 88, p. 257901, 2002.

[142] V. Garcés-Chávez, D. McGloin, M. J. Padgett, W. Dultz, H. Schmitzer, and K. Dholakia, "Observation of the transfer of the local angular momentum density of a multiringed light beam to an optically trapped particle," *Phys. Rev. Lett.*, vol. 91, p. 093602, 2003.

[143] G. Molina-Terriza, J. P. Torres, and L. Torner, "Management of the angular momentum of light: Preparation of photons in multidimensional vector states of angular momentum," *Phys. Rev. Lett.*, vol. 88, p. 013601, 2001.

[144] F. Cardano and L. Marrucci, "Spin–orbit photonics," *Nat. Photonics*, vol. 9, p. 776, 2015.

[145] H. Rubinsztein-Dunlop, A. Forbes, M. V. Berry, M. R. Dennis, D. L. Andrews, M. Mansuripur, C. Denz, C. Alpmann, P. Banzer, T. Bauer, *et al.*, "Roadmap on structured light," *J. Opt.*, vol. 19, p. 013001, 2016.

[146] M. Mirhosseini, O. S. M. na Loaiza, M. N. O'Sullivan, B. Rodenburg, Z. Shi, M. Malik, M. P. J. Lavery, M. J. Padgett, D. J. Gauthier, and R. W. Boyd, "Quantum information with structured light," in *Frontiers in Optics 2016*, p. LTu1E.3, Optical Society of America, 2016.

[147] R. C. Jones, "A new calculus for the treatment of optical systemsi. description and discussion of the calculus," *J. Opt. Soc. Am.*, vol. 31, p. 488, 1941.

[148] A. Ashkin, "Applications of laser radiation pressure," *Science*, vol. 210, p. 1081, 1980.

[149] S. Chang and S. S. Lee, "Optical torque exerted on a homogeneous sphere levitated in the circularly polarized fundamental-mode laser beam," *J. Opt. Soc. Am. B*, vol. 2, p. 1853, 1985.

[150] E. Santamato, B. Daino, M. Romagnoli, M. Settembre, and Y. R. Shen, "Collective rotation of molecules driven by the angular momentum of light in a nematic film," *Phys. Rev. Lett.*, vol. 57, p. 2423, 1986.

[151] E. Karimi, B. Piccirillo, E. Nagali, L. Marrucci, and E. Santamato, "Efficient generation and sorting of orbital angular momentum eigenmodes of light by thermally tuned q-plates," *Appl. Phys. Lett.*, vol. 94, p. 231124, 2009.

[152] B. Piccirillo, V. D'Ambrosio, S. Slussarenko, L. Marrucci, and E. Santamato, "Photon spin-to-orbital angular momentum conversion via an electrically tunable q-plate," *Appl. Phys. Lett.*, vol. 97, p. 241104, 2010.

[153] V. D'ambrosio, E. Nagali, S. P. Walborn, L. Aolita, S. Slussarenko, L. Marrucci, and F. Sciarrino, "Complete experimental toolbox for alignment-free quantum communication," *Nat. Commun.*, vol. 3, p. 961, 2012.

[154] C. Vitelli, N. Spagnolo, L. Aparo, F. Sciarrino, E. Santamato, and L. Marrucci, "Joining the quantum state of two photons into one," *Nat. Photonics*, vol. 7, p. 521, 2013.

[155] V. Parigi, V. D'Ambrosio, C. Arnold, L. Marrucci, F. Sciarrino, and J. Laurat, "Storage and retrieval of vector beams of light in a

multiple-degree-of-freedom quantum memory," *Nat. Commun.*, vol. 6, p. 7706, 2015.

[156] D. Naidoo, F. S. Roux, A. Dudley, I. Litvin, B. Piccirillo, L. Marrucci, and A. Forbes, "Controlled generation of higher-order poincaré sphere beams from a laser," *Nat. Photonics*, vol. 10, p. 327, 2016.

[157] E. Nagali, L. Sansoni, F. Sciarrino, F. De Martini, L. Marrucci, B. Piccirillo, E. Karimi, and E. Santamato, "Optimal quantum cloning of orbital angular momentum photon qubits through hong–ou–mandel coalescence," *Nat. Photonics*, vol. 3, p. 720, 2009.

[158] F. Cardano, E. Karimi, L. Marrucci, C. de Lisio, and E. Santamato, "Violation of leggett-type inequalities in the spin-orbit degrees of freedom of a single photon," *Phys. Rev. A*, vol. 88, p. 032101, 2013.

[159] E. Karimi, F. Cardano, M. Maffei, C. de Lisio, L. Marrucci, R. W. Boyd, and E. Santamato, "Hardy's paradox tested in the spin-orbit hilbert space of single photons," *Phys. Rev. A*, vol. 89, p. 032122, 2014.

[160] F. Cardano, E. Karimi, S. Slussarenko, L. Marrucci, C. de Lisio, and E. Santamato, "Polarization pattern of vector vortex beams generated by q-plates with different topological charges," *Appl. Opt.*, vol. 51, p. C1, 2012.

[161] A. D'Errico, M. Maffei, B. Piccirillo, C. De Lisio, F. Cardano, and L. Marrucci, "Topological features of vector vortex beams perturbed with uniformly polarized light," *Sci. Rep.*, vol. 7, p. 40195, 2017.

[162] A. Dauphin and N. Goldman, "Extracting the chern number from the dynamics of a fermi gas: Implementing a quantum hall bar for cold atoms," *Phys. Rev. Lett.*, vol. 111, p. 135302, 2013.

[163] S. Nakajima, T. Tomita, S. Taie, T. Ichinose, H. Ozawa, L. Wang, M. Troyer, and Y. Takahashi, "Topological thouless pumping of ultracold fermions," *Nat. Phys.*, vol. 12, p. 296, 2016.

[164] N. Fläschner, B. S. Rem, M. Tarnowski, D. Vogel, D.-S. Lühmann, K. Sengstock, and C. Weitenberg, "Experimental reconstruction of the berry curvature in a floquet bloch band," *Science*, vol. 352, p. 1091, 2016.

[165] Y. Gao, S. A. Yang, and Q. Niu, "Field induced positional shift of bloch electrons and its dynamical implications," *Phys. Rev. Lett.*, vol. 112, p. 166601, 2014.

[166] K. Wang, X. Qiu, L. Xiao, X. Zhan, Z. Bian, W. Yi, and P. Xue, "Simulating dynamic quantum phase transitions in photonic quantum walks," *arXiv preprint arXiv:1806.10871*, 2018.

[167] J. C. Budich and M. Heyl, "Dynamical topological order parameters far from equilibrium," *Phys. Rev. B*, vol. 93, p. 085416, 2016.

[168] L. Yuan, Q. Lin, M. Xiao, and S. Fan, "Synthetic dimension in photonics," *Optica*, vol. 5, p. 1396, 2018.

[169] W. A. Benalcazar, B. A. Bernevig, and T. L. Hughes, "Quantized electric multipole insulators," *Science*, vol. 357, p. 61, 2017.

[170] V. Gurarie, "Single-particle green's functions and interacting topological insulators," *Phys. Rev. B*, vol. 83, p. 085426, 2011.

[171] A. M. Essin and V. Gurarie, "Bulk-boundary correspondence of topological insulators from their respective green's functions," *Phys. Rev. B*, vol. 84, p. 125132, 2011.

Aknowledgements

I am greatly indebted to many people for their help during the writing of this thesis. First, I would like to thank my supervisors: Lorenzo Marrucci, who has been a generous and inspirational guide since the first steps of my scientific formation, and Maciej Lewenstein, who welcomed me in his amazing group giving me all the tools I needed to accomplish my goals.

I thank for the stimulating environment my colleagues from Naples and Barcelona, Filippo Cardano, Alexandre Dauphine, and Pietro Massignan, for sharing their ideas with me and offering me their valuable help every time I needed it.

I am also indebted to the brilliant physicists with whom I had the honour to collaborate: Bryce Gadway, Taylor Hughes, Enrico Santamato, Bruno Piccirillo, Vittorio Cataudella, Giulio Defilippis, Rauf Barboza, Eric Meier, Alessio D'Errico.

I thank Hannha Price and Oded Zilberberg for their kind and useful advices and Nathan Goldman, Emilio Pisanty and Massimiliano Stengel for the stimulating conversations.

Writing this thesis would have been much more difficult without the moral support of my oldest friends. Therefore, I whole-heartedly thank Alessandro, Edoardo, Caterina, Michele, Roberta, Michela for having been there for me all the time, and my family for having always tenderly overestimated my capabilities.

Finally, I thank the friends who I have found in Barcelona whose friendship I consider as one of my main achievements of these years: Marco, Stefano, Miriana, Amabile, Natalia, Lorenzo, Laura, Pierluigi, Tullia and Gorka, whom I also thank for the drawing in the introduction of this thesis.